Univerzita Karlova v Praze
Matematicko-fyzikálná fakulta

DISERTAČNÍ PRÁCE

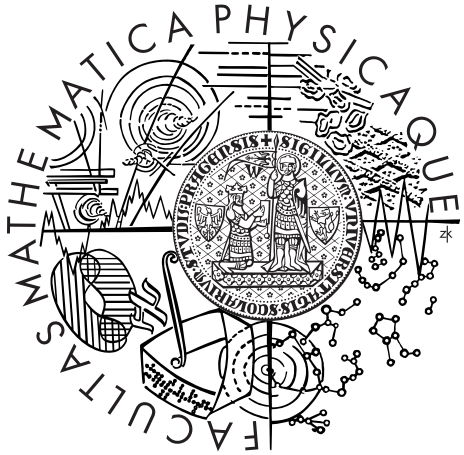

Mgr. Jana Brotánková

Studium horkého plazmatu v experimentálních zařízeních typu Tokamak

Katedra fyziky povrchů a plazmatu
Vedoucí disertační práce: *RNDr. Jan Stöckel CSc.*
Konzultant: *Prof. RNDr. Milan Tichý, DrSc.*
Studijní program: *Fyzika*
Studijní obor: *Fyzika povrchů a ionizovaných prostředí*

Disertační práce byla vypracována na Ústavu fyziky plazmatu, v.v.i.
Akademie věd České Republiky
oddělení Tokamak
Za Slovankou 3, 182 21 Praha 8

Charles University in Prague
Faculty of Mathematics and Physics

PhD THESIS

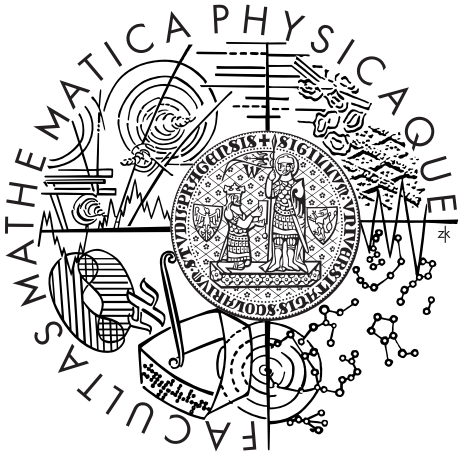

Mgr. Jana Brotánková

Study of high temperature plasma in tokamak-like experimental devices

Department of Surface and Plasma Science
Supervisor: *RNDr. Jan Stöckel CSc.*
Consultant: *Prof. RNDr. Milan Tichý, DrSc.*

Study programme: *Physics*
Study branch: *Physics of Plasmas and Ionized Media*

The PhD thesis was carried out at the Institute of Plasma Physics, v.v.i.
Academy of Sciences of the Czech Republic
Tokamak department
Za Slovankou 3, 182 21 Prague 8

Prohlašuji, že jsem svou disertační práci napsala samostatně a výhradně s použitím citovaných pramenů. Souhlasím se zapůjčováním práce.

V Praze dne *3.3.2009*

Mgr. Jana Brotánková

विघ्नानाँ नाशनँ कर्तुम्
भूतानाँ रक्षणाय च
देवानँ तुष्तये चापी
प्रेक्षकानाँ विभूतये
श्रेयसे नयकस्थात्र
पात्रसँरक्षणाय च
आचार्य शिक्षासिध्यर्थँ
पुष्पञ्जलिमथारभेत्

Acknowledgements

First of all, I would like to thank my supervisor Jan Stöckel who was guiding me on the way of knowledge. For his precious discussions about the tokamak CASTOR and plasma physics when he shared his broad experience with me, his neverending patience with explaining the secrets (and obvious things) of the research. His kindness and wonderful life attitude made our department a great place to work for me and for many other people, including our guests. His intoxicating optimism and social behaviour turned experiments into pleasant events when we were not aware of working hours. Such people are rare and I am sincerely happy to be his student. Thanks for his understanding and encouraging me in difficult times, reminding me that first I need to smile when I did not feel like at all.

Many thanks belong also to Milan Tichý, my consultant from the faculty, my guardian angel and a blessing for many other students of our faculty. He always had opened door for me, his support and readiness to help was a solid pillar in my past years. Thanks for the patience and carefulness in reading my work and for his interest in my research.

Thanks to my colleagues in the institute. The technicians for taking care of the tokamak, without them, the experiments would be infeasible. My colleagues, mainly Honza Horáček, Ivan Ďuran, Renaud Dejarnac, Vláďa Weinzettl and Martin Hron who always helped me in need and who were never annoyed by my requests. Thanks to Jirka Adámek for his fruitful cooperation and enriching experience while dealing with him. Thanks to the other colleagues who are not listed above, but who were supporting me and who made the environment of the department and the institute pleasant.

Thanks to Guido van Oost for his kindness, for his nice collaboration in our projects, interest in my research and valuable comments.

Thanks to my colleagues from abroad. The RFX-mod team, mainly Gianluigi Serianni, Monica Spolaore, Matteo Zuin, Matteo Agostini and others. Special thanks to Emilio Martines for his fruitful discussions and invaluable help with IDL and statistic analysis, for his useful IDl procedures, for establishing my cooperation with Padova and for his effort in the Ball-pen probe development research.

Thanks to the TJ-II team, mainly Maria Angeles Pedrosa Luna and Carlos Hidalgo Vera for inviting me to the institute and for their hospitality and help with the work. To Maria Angeles for her support, her discussions and her help in the jungle of new environment and to Carlos for his great ideas and insight. Thanks also to Victor Iván Vargas Blanco for his help in struggling with IDL in Madrid.

Thanks to Pascal Devynck for his nice discussions about physics and arts and for the interesting work about turbulence. Thanks to Codrina Ionita and Roman Schrittwieser, Gheorghe Popa and Claudiu Costin for their cooperation in the matter of the Ball-pen probe. Thanks to Linda van de Peppel for her exemplary work in our department such as for her refreshing company which, among others, resulted in making me an opera-fan.

Thanks to my colleagues who were helping me with the Thomson Scattering

project. To Petra Bílková and others from our institute for their cooperation, to Rolie Barth and Hennie van der Meiden from FOM for their fruitful discussions and to Michael Kantor, Mike Walsh and Roberto Pasqualotto who help our team.

Thanks to my professors and colleagues from the Faculty of Mathematics and Physics for the knowledge they have passed me on and for a wonderful environment at the department seminars. Thanks to Jana Šafránková for the great patience she had with me.

Thanks to my colleagues from the Faculty of Nuclear Sciences and Physical Engineering at the Czech Technical University in Prague for their support during my teaching there. Special thanks belong to Vojta Svoboda who brought me to our institute twelve years ago.

Thanks to leaders of the project "Otevřená Věda" (Open Science), mainly to Dagmar Dvořáková and Tomáš Palatý. This project involving high school students into the science let me supervising Matěj Peterka, who slowly became to be a nice member of our team. Thanks him for his interest, his enthusiasm to learn and his willingness to help whenever needed.

Thanks to my parents and family who brought me up and who supported me as well as they could. For giving me the background and helping me in life struggles.

Last but not least I would like to thank to my friends. Without them, my life would be a lonely sojourn in this space-time. Thanks to my neighbours from the hostel, for being tolerant and just nice. To my colleagues from the student society Spolek Matfyzák and recently founded Studentská Unie UK for giving me their trust and for their energy. To all the others who brightened my days, who comforted me when I needed and who were just happy to be with me. Thanks to my friends who left their fingerprints in my thesis – Martin for his invaluable help with editing, mainly with LaTeX when my struggles were beyond my patience and Harish who was never tired of my inventions concerning English.

At this point, I should not forget the people who were troubling me. By introducing obstacles into my life, they were challenging me, giving me lessons and contributing to keeping my life in the state of marginal stability.

Part I

Introduction

Chapter 1

Aims of the thesis

The understanding of plasma turbulence in magnetic confinement devices is believed to be one of the key elements leading to practical exploitation of fusion as an ultimate energy source for mankind. As is mentioned in the introduction chapters, turbulence is responsible for anomalously high losses of particles and energy at the plasma edge. In order to control the effects caused by turbulence, proper understanding of the phenomena occurring at the edge plasma is required.

In spite of the need for detailed knowledge about the physics of the plasma edge, it still remains an open issue for the fusion community. The Institute of Plasma Physics in Prague contributes to this research by taking advantage of the small CASTOR tokamak. Relatively cold plasma and short discharges enable a detailed studies of radial and poloidal profiles of important plasma parameters in the edge plasma region. Several arrays of Langmuir probes with high spatial and temporal resolution are being developed as well as designs of advanced probes which are directly tested and improved for large fusion facilities. Last but not least is the role of the CASTOR tokamak for the education of new scientists in fusion research.

The aims of my PhD thesis can be concluded in several items:

- Participation in experiments and development of new diagnostic methods
  - domestic and international campaigns at the CASTOR tokamak
  - measurements at the TJ-II stellarator
  - measurements at the RFX-mod reversed field pinch
  - contribute to development of the Ball-pen probe - a new electric probe designed in IPP Prague
- Develop programmes for evaluating big packages of experimental data by means of statistical methods
  - correlation analysis
  - Fourier methods for calculating of frequency spectra
  - other modern statistical methods
- Analyse experimental data in the standard regimes as well as in regimes with improved confinement
- Contribute to the programme for education of new scientists

The thesis is organised in the following way: In the first part, an introduction to the fusion research with focus on the edge plasma of fusion devices is given together with a description of the CASTOR tokamak and its diagnostic tools. The second part briefly presents my work in the field of investigation of turbulence at the plasma edge of the CASTOR tokamak, the TJ-II stellarator, and the RFX-mod reversed field pinch. The third part exposes my contribution to the development of the Ball-pen probe. In the last (fourth) part, the conclusions are given and a list of my publications is appended.

Chapter 2

Introduction to nuclear fusion

A brief introduction to fusion research as well as the basic principle of the plasma confinement in the experimental device named tokamak is given in this chapter.

2.1 Fusion

Pollution as well as increasing demand of energy is one among the most serious problems of current civilization. Realization of controlled nuclear fusion reactor on the Earth aims to solve the second one.

The concept of fusion research is to make a reactor where hydrogen nuclei get synthetized together to produce helium and energy in a controlled manner. Similar reactions occurring in the sun and other stars produce required energy to support life on Earth.

The problem of nuclear fusion is that the input is formed by two positively charged particles, which repel each other due to the Coulombic force. They need to meet for a distance of 10^{-10} m where the strong nuclei force asserts itself and bounds the nuclei together. This can be achieved by high energetic collisions, generated either by accelerators or by heating ionized fuel. It was shown that the injection of accelerated nuclei into a hydrogen target is not efficient enough thus the research is focused to the second option: heating the fuel.

2.1.1 Nuclear fusion reactions

There are several fusion reactions involving various hydrogen isotopes and helium with different cross-sections, as shown in figure 2.1. The highest cross-section at

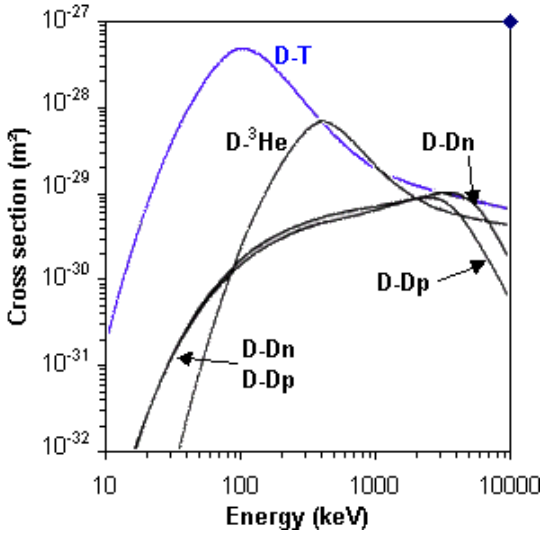

Figure 2.1: *Cross-sections of fusion reactions as a function of the energy of nuclei.*

reasonable energy has the reaction with heavy isotopes deuterium ($D = {}^2H$) and tritium ($T = {}^3H$):

$$D + T \rightarrow {}^4He\ (3.52\ \text{MeV}) + \text{n}\ (14.1\ \text{MeV}). \tag{2.1}$$

Deuterium is a common element on earth as it occurs in all compounds containing hydrogen in the rate of 1:6500 (0.015%) to the ${}^1H$ and it is easy to be separated. On the other hand, Tritium is a radioactive gas with half-life of 12.4 years and is

not readily avialable or present in nature. It needs to be synthetized from Lithium, directly from the inner wall of the reactor by the reaction with fusion neutrons:

$$n + {}^6Li \rightarrow {}^4He\ (2.1\ \text{MeV}) + \text{T}\ (2.7\ \text{MeV}). \tag{2.2}$$

The cross-sections shown in figure 2.1 come from the calculations of the energy needed for overcoming the potential barrier for one nucleus to approach another for a sufficient time to fuse. Although this barrier is 500 keV, for our most interesting case (the D-T reaction), nuclei with lower energies can fuse together due to the tunnel effect. This tunnel effect is considered while calculating the energy values shown in figure 2.1.

2.1.2 Lawson criterion

Plasma is not a group of individual nuclei, but a set of particles with the Maxwell distribution of velocities. The rate coefficient for the D-T reaction as a function of temperature is plotted in figure 2.2. It is obtained by averaging the cross-section (plotted in figure 2.1) over the velocity distribution.

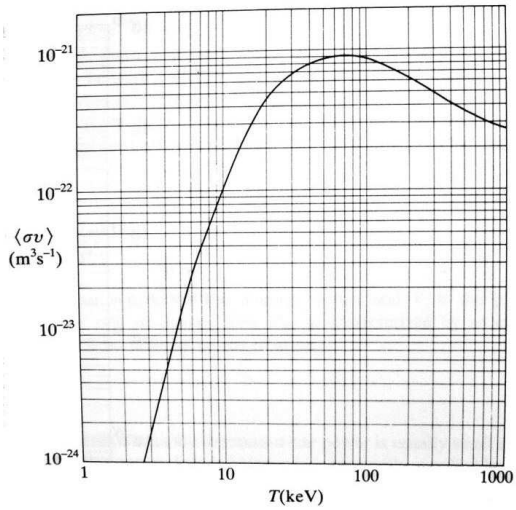

Figure 2.2: *Rate coefficient of the D-T reaction as a function of temperature.*

For using fusion as a source of energy, a relation among plasma parameters, termed the Lawson criterion, must be fulfilled [1]:

$$L = n\tau_E T \geq c_{crit} \tag{2.3}$$

where n is the ion density, T is the ion temperature and the definition of τ_E depends on the approach to the fusion (see in the following); roughly it is the time when the thermonuclear reactions can take place. The product $n\tau_E$ as a function of temperature is plotted in figure 2.3. For the $D-T$ reaction, the $c_{crit} \sim 5 \cdot 10^{21}$ s·keV·m^{-3}. In order to build up a fusion reactor, we are looking for a compromise among density, energy confinement time, and temperature.

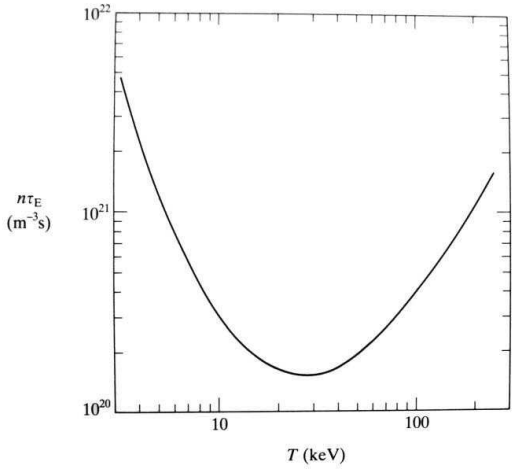

Figure 2.3: *Product $n\tau_E$ as the function of temperature.*

2.1.3 Approaches to nuclear fusion

Two concepts are being developed to fulfill the Lawson criterion: low density confined for a long time in magnetic traps and high density kept for a short time.

- **Magnetic confinement**

  As the name suggests, this approach is to confine the hot plasma for a time long enough to let the fast ions from the tail of the Boltzmann distribution overcome the Coulomb barrier, fuse, and sustain the reaction by covering the energy losses. The Lawson criterion for the magnetic fusion is $L = n\tau_E T$ where τ_E represents the energy confinement time ($\sim$ 5 s) and the ion density n takes values $\sim 10^{20}$ m^{-3}.

  From the cross-section in figure 2.2, it seems that the optimal temperature T (which means the temperature of the highest cross-section) is in the range of 50 to 100 keV. For a fusion reactor, the energy balance between the power losses and the heating by α-particles (the products of the nuclear reactions) must be considered. Power losses and the α-particle heating as functions of temperature are presented in figure 2.4. This figure is important to realize that the optimal temperature for the plasma in fusion reactor is around 15 keV.

  Plasma is confined in magnetic traps of different configurations. The most advanced are the toroidal devices: tokamaks, stellarators, and reversed field pinches.

- **Inertial fusion**

  On the contrary, the second approach uses high densities and very short time of confinement. This method is based on micro-explosions of pellets (frozen fuel) heated by high-energy laser or ion beams. The outer shell of the pellet, made usually from plastics, explodes and by the inertial force, it compresses the fuel inside which consequently reaches the required temperature and density.

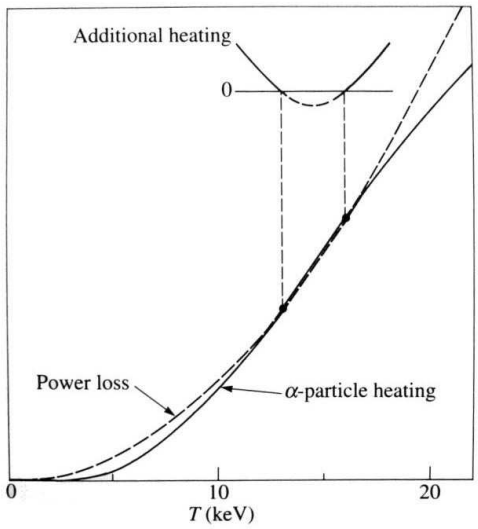

Figure 2.4: *Power losses and the α-particle heating as functions of temperature. The additional heating is necessary for temperatures outside the range of the power gain.*

Typical configuration of an inertial fusion device is limited by achievable densities $\sim 10^{30}$ m^{-3}. Burning time of the pellet for such compression is $\tau_E \sim 10^{-10}$ s and the temperature takes values of ~ 30 keV.

2.2 Tokamaks

The most promising reactor arrangement in current fusion research is the tokamak. It is a ring-shaped vacuum vessel placed as the secondary circuit of a transformer. Plasma is confined inside by a strong magnetic field along the chamber and it is heated by electric current.

2.2.1 Magnetic field of tokamak

A scheme of a tokamak is shown in figure 2.5. Tokamaks take advantage of the fact that the charged particles cannot move across magnetic field but they follow the field lines [1]. The vacuum chamber is wrapped by poloidal coils generating magnetic field along the torus (in the toroidal direction). This field is usually around 1 T for small tokamaks and up to 4 T for large facilities (JET). The toroidal magnetic field decreases with increasing major radius R, $B_{tor} \sim 1/R$ due to the toroidal geometry. As a consequence, the grad B drift $\nabla B \times \vec{B}$ separates ions and electrons and creates an electric field perpendicular to $\vec{B}_{tor}$. The resulting $\vec{E}_{rad} \times \vec{B}_{tor}$ drift causes a collective motion of charged particles, making the plasma unstable.

A significant feature of tokamak configuration is the plasma current. It flows in the toroidal direction having two important tasks: it heats the plasma and simultaneously it eliminates the $\nabla B \times \vec{B}$ instability by giving the current its poloidal component. The ring of fully ionized plasma is placed as the secondary winding of a transformer as shown in figure 2.5. At the beginning of the discharge, the plasma current ionizes and heats the working gas by so-called ohmic heating (details are

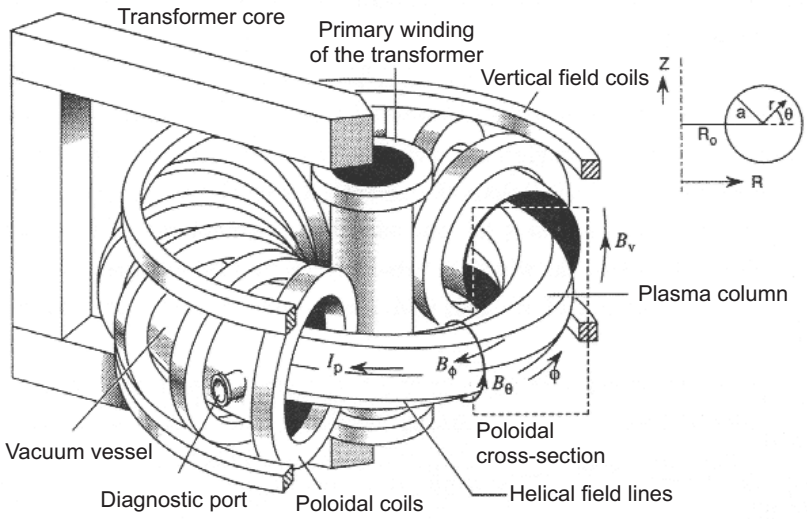

Figure 2.5: *Principle of tokamak.*

given in section 3.2). Simultaneously, it generates a poloidal magnetic field, which twists the magnetic field lines giving the resulting magnetic field a helical shape.

The magnetic field lines lay on nested surfaces centred on the magnetic axis as shown in figure 2.6. These layers are termed *magnetic flux surfaces*. The poloidal component of the tokamak magnetic field is ~ 10 times lower than the toroidal one. Thus, the helicity of the magnetic field is low and one field line needs several turns in the toroidal direction in order to intersect the poloidal cross-section at the same point. This number is termed the *safety factor* and is described in section 3.2.7.

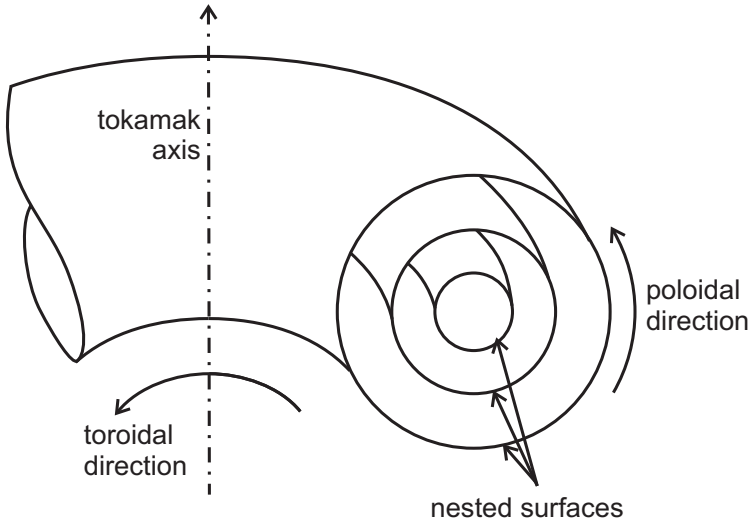

Figure 2.6: *Magnetic surfaces.*

Chapter 3

CASTOR tokamak and diagnostic tools

This chapter gives a description of the CASTOR tokamak, generating the discharge, the main plasma parameters and diagnostics.

Most of the experiments presented in this thesis were performed at the CASTOR tokamak which was operated in the Institute of Plasma Physics (IPP), AS CR in Prague. This tokamak was brought to the IPP Prague in 1977 from Kurchatov Institute in Moscow, Russia. The name TM-1-MH was substituted by the acronym CASTOR: Czech Academy of Science TORus after reconstruction in 1985. During its operation in Prague, CASTOR underwent several innovations, *e.g.*, the vacuum chamber replacement and a complete rebuild of the detection system. The appearance of CASTOR just before its disassembly at the end of 2006 is shown in figure 3.1. After the shut down, CASTOR was transported to the Faculty of Nuclear Sciences and Physical Engineering of the Czech Technical University in Prague and recently it is being reinstalled. It shall be operated under a new name GOLEM. Since I started writing the thesis when CASTOR was still in operation, it is in the present tense; some of the technical details may become irrelevant for GOLEM.

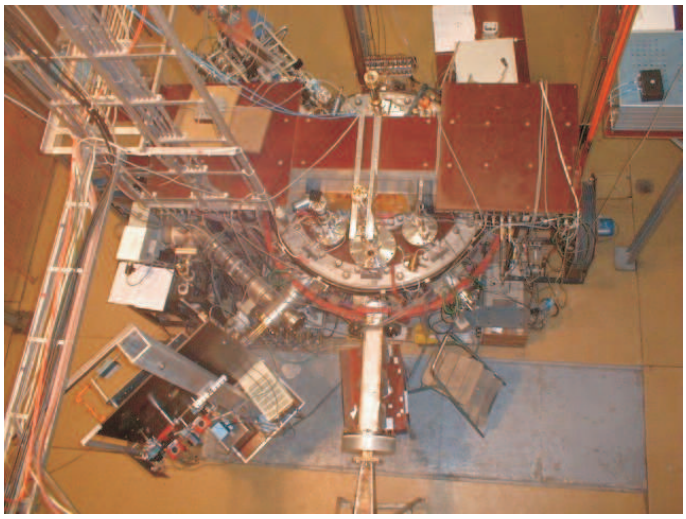

Figure 3.1: *Top view of the CASTOR tokamak. The North port is at the bottom of the picture, with connected lower hybrid grill. Microwave diagnostics is on the left from the grill. On the top ports, several probe manipulators are mounted.*

3.1 Basic parameters

CASTOR is a small size tokamak. It does not enable reaching the temperature and confinement time high enough to ignite the fusion reactions. Nevertheless, for investigation the hot plasma, devices of CASTOR size have a capability of bringing a valuable contribution. The main advantage is their high flexibility. Testing new diagnostic tools is much more feasible and cheaper in these relatively simple facilities. Due to the low temperature, plasma enables us to immerse the diagnostic probes deep inside, thus a very detailed investigation of the edge plasma may be performed. The importance of such devices for education is also worth mentioning. A number of students of different degrees (bachelor, master, PhD) were gaining their experience with fusion facilities at the CASTOR tokamak department in the scope of their

studies, several Summer schools for students and young scientists were organized by the CASTOR team.

CASTOR is a limiter tokamak with circular poloidal cross-section and with an iron transformer core. It has 18 diagnostic ports, which are organized in six groups of three ports as shown in figure 3.2. Each group consists of a top, bottom and a mid plane port. The main (*i.e.*, the largest) ports are located on the North and on the South side of the torus; 45° from them to each side, are the other groups: South-East, South-West, North-East and North-West. The poloidal limiter made of molybdenum is located 40° to the West from the North port.

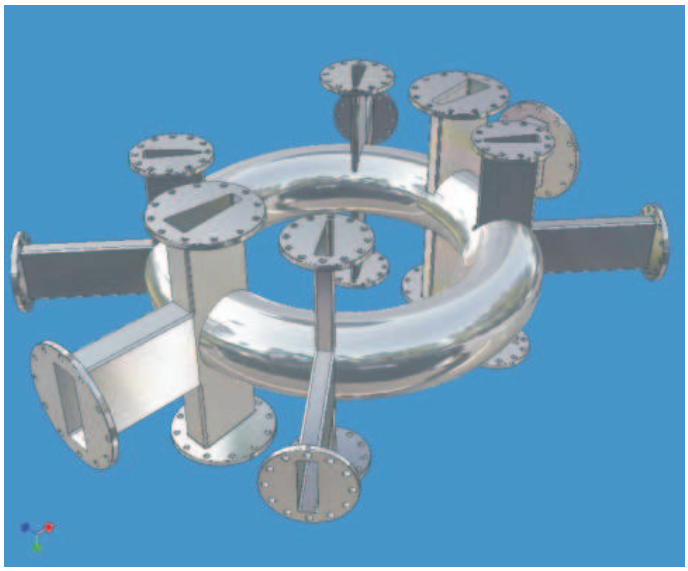

Figure 3.2: *Diagnostic ports of the CASTOR tokamak. The picture was made by Pavel Stejskal.*

Main parameters of the CASTOR tokamak:

Major radius	0.4 m
Minor radius (vacuum vessel)	0.1 m
Plasma radius (limiter radius)	0.085 m
Toroidal magnetic field	$0.5 - 1.5$ T
Plasma current	$5 - 20$ kA
Length of the discharge	< 50 ms
Central electron density	$0.5 - 3 \times 10^{19}$ m^{-3}
Central electron temperature	$100 - 300$ eV
Edge electron density	$1{\times}10^{18}$ m^{-3}
Edge electron temperature	$10 - 40$ eV

3.2 Discharge in the CASTOR tokamak

3.2.1 Plasma generation

Temporal evolution of a typical discharge of the CASTOR tokamak is shown in figure 3.3. Before discharge, the vacuum vessel is evacuated down to the pressure of 10^{-4} Pa and filled by working gas (hydrogen). After that, the power supplies are connected to the toroidal magnetic field coils. Since now, the toroidal magnetic field B_{tor} starts increasing (detailed behaviour is described in appendix A-1). When B_{tor} reaches the range of 0.8 – 1 T (which is usually 10 – 25 ms after switching it on), the primary transformer winding is automatically connected to its power supplies (capacitor banks) [2, 3] and the toroidal electric field E_{tor} is induced within the vacuum vessel. The B_{tor} is measured by an open loop fixed at the top of the vessel. The measured voltage is termed a loop voltage U_{loop}, its temporal evolution is shown in the second panel of figure 3.3. The $E_{tor} = U_{loop}/2\pi R$ starts to accelerate free electrons, which are produced by an electron gun placed in the limiter shadow. Some free electrons are always present due to the cosmic radiation, but their amount

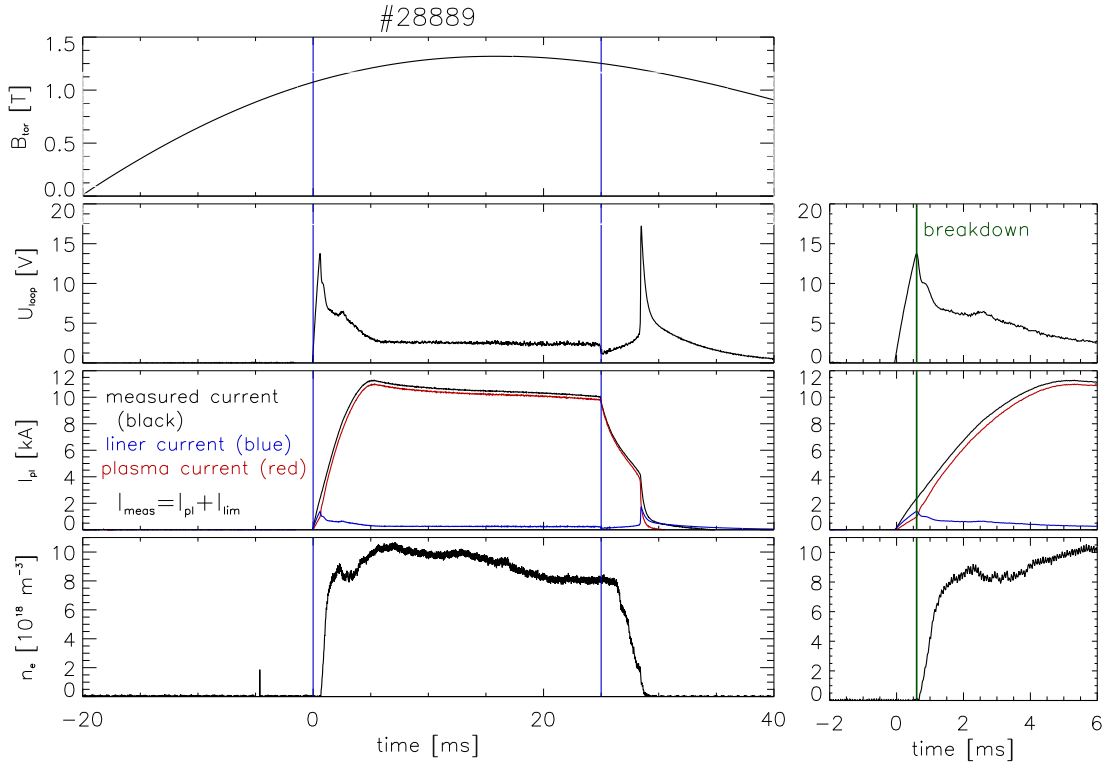

Figure 3.3: *Temporal evolution of a typical CASTOR discharge, with parameters: toroidal magnetic field (B_{tor}), loop voltage (U_{loop}), plasma current (I_{pl}), line averaged electron density (n_e). The whole discharge is plotted in left panels, the zoomed in start-up phase is shown in the right ones. Blue vertical lines (left panels) indicate the beginning and the end of the discharge. Green vertical lines (right panels) denote the breakdown.*

is not sufficient for a fast and reproducible breakdown (the moment of ignition of the discharge). After breakdown, the electron density n_e increases exponentially, as shown in figure 3.3, right bottom panel. After $\sim$ 1 ms from breakdown, the working gas is completely ionized. Simultaneously, the plasma current I_{pl} increases to the rate of 2 MA/s, which is determined by the primary circuit parameters. The slope dI_{pl}/dt has to be kept relatively low to negate the skin effect, which could drive the current only on the surface of the plasma column. In this case, the radial profile of plasma current and plasma current density gets a hollow shape, plasma gets unstable and consequently disrupts.

After the plasma current reaches values of $\sim$ 10 kA, it tends to remain constant for the next $20-30$ ms. During this quasistationary phase of discharge, the loop voltage is $2-3$ V, as shown in figure 3.3. It is interesting to realize that the plasma current in the range of 10 kA is driven by toroidal electric field 1 V/m only. The quasistationary phase is exploited for physical measurements. After the $20-30$ ms, the primary winding of the transformer is set to be short circuited. The plasma current exponentially decays. This is called a soft termination of discharge or a "soft landing".

3.2.2 Electron density, gas filling

Before the working gas (hydrogen) is injected into the vacuum vessel, it is purified by passing through a heated nickel tube as schematically shown in figure 3.4. A thin nickel finger is immersed into a reservoir of hydrogen with pressure of about 3 atmospheres. It is heated by electric current. For a certain temperature, the finger walls become permeable for hydrogen only.

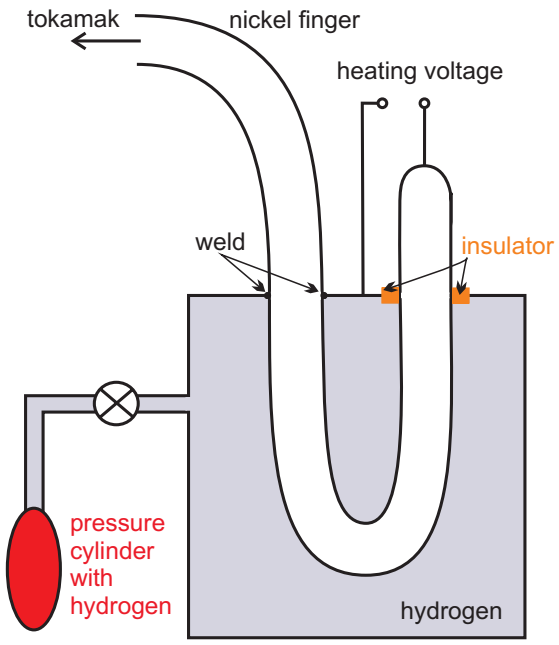

Figure 3.4: *Scheme of a nickel finger for purifying hydrogen.*

The working pressure is $\sim 10 - 20$ mPa. The stationary filling continues during the whole discharge but it is too slow to compensate losses of charged particles caused by the finite particle confinement time $\sim 1 - 2$ ms. These losses are compensated by an additional injection of hydrogen during the stationary phase of the discharge controlled by a piezoelectric valve ("gas puffing").

The electron density is measured by a microwave interferometer placed on the top of the North-East port. It is line averaged over a chord coming through the geometric centre of the vessel, and normalized to show the averaged electron density in the whole plasma volume. The temporal evolution of the result (line averaged electron density n_e) is shown in figure 3.3, bottom panel. A detailed calculation of the central electron density and averaged electron density is given in appendix A-2.

3.2.3 Plasma current

Plasma current is measured by a Rogowski coil [4], enlacing the tokamak chamber. The active area of the coil is perpendicular to the direction of the poloidal magnetic field. The coil is outside the stainless steel chamber, thus it measures not only the plasma current, but also the current through the tokamak liner I_{liner}. Hence, the plasma current I_{pl} should be determined as

$$I_{pl} = I_{measured} - I_{liner}. \tag{3.1}$$

At the beginning of the discharge - before breakdown (avalanche phase of the discharge), the plasma resistivity is infinite, thus the whole current flows through the liner, which has resistivity ~ 10 mΩ:

$$I_{liner} = \frac{U_{loop}}{R_{liner}} \approx \frac{10\ V}{10 \cdot 10^{-3}\ \Omega} = 1\ kA. \tag{3.2}$$

After breakdown, the resistivity of plasma drops. During the quasistationary part of the discharge, the resistivity of plasma is ~ 0.2 mΩ, U_{loop} has values of $2 - 3$ V while I_{liner} becomes

$$I_{liner} = \frac{U_{loop}}{R_{liner}} \approx \frac{2.5\ V}{10 \cdot 10^{-3}\ \Omega} = 250\ A, \tag{3.3}$$

which is a negligible value compared to the $I_{pl} \sim 10\ kA$. The starting phase of the discharge is shown in detail in figure 3.3, right panels.

3.2.4 Plasma resistivity, ohmic power

The resistivity of plasma R in the quasistationary part of discharge becomes ~ 0.2 mΩ as illustrated in the top panel of figure 3.5. R is calculated as

$$R = \frac{U_{loop}}{I_{pl}}. \tag{3.4}$$

The ohmic power

$$P_{oh} = U_{loop} \cdot I_{pl} \tag{3.5}$$

is between 20 and 30 kW (see figure 3.5, bottom panel).

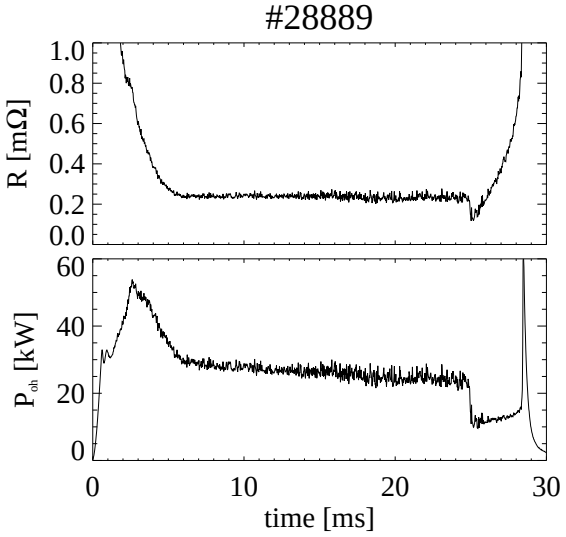

Figure 3.5: *Temporal evolution of the resistivity and the ohmic power of plasma for a typical CASTOR discharge.*

3.2.5 Equilibrium position of plasma column

The plasma ring tends to expand in the horizontal direction due to a magnetic pressure. In order to compensate this effect, a quadrupole of poloidal magnetic field coils generates a vertical magnetic field, which pushes the plasma back. A schematic illustration is shown in figure 3.6. The quadrupole of the vertical magnetic field coils (pink colour) is placed in between the vacuum chamber and a copper shell. It is connected in series with the primary transformer winding.

The equilibrium position of plasma is controlled by a feed back system [5, 6]. The plasma position is detected by two couples of Mirnov coils: top with bottom, and HFS with LFS. These coils are located inside the chamber in the limiter shadow as depicted in figure 3.6.

Signal of the two probes in each couple is summed and presented as U_{vert} (top and bottom coils) and U_{rad} (LFS and HFS ones). If the plasma position is stable, U_{vert} and U_{rad} are equal to zero. Once the plasma moves, it induces different signals in the Mirnov coils. The U_{vert} and U_{rad} signals are lead via feed back system into a transistor amplifier and further into the stabilization quadrupole toroidal coils (blue and green colour in figure 3.6), which produce vertical or horizontal magnetic field, pushing the plasma back, as schematically demonstrated in figure 3.7. The temporal evolution of the signals relevant to the feed back system is shown in figure 3.8.

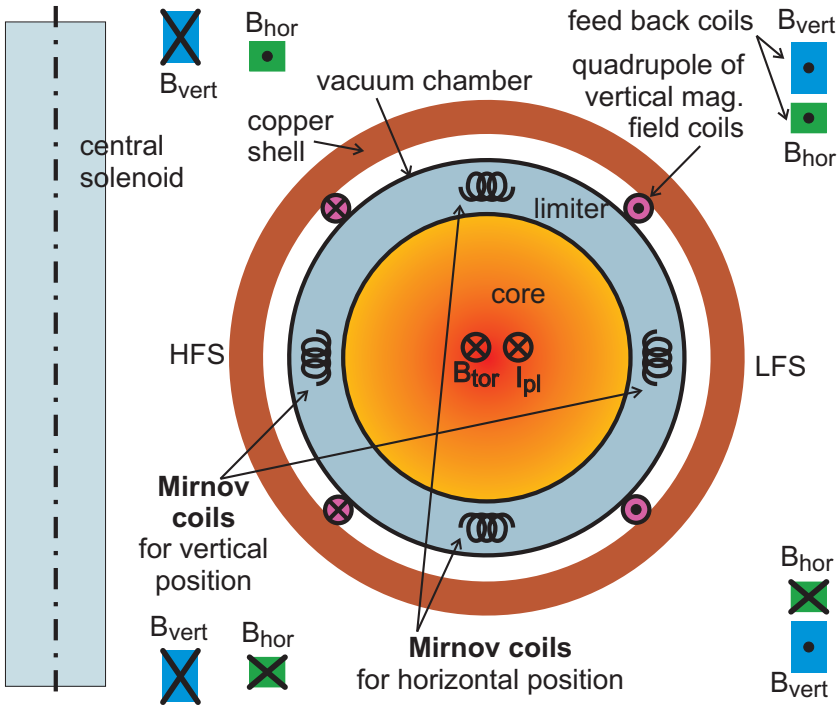

Figure 3.6: *Magnetic system of the CASTOR tokamak, poloidal cross-section.*

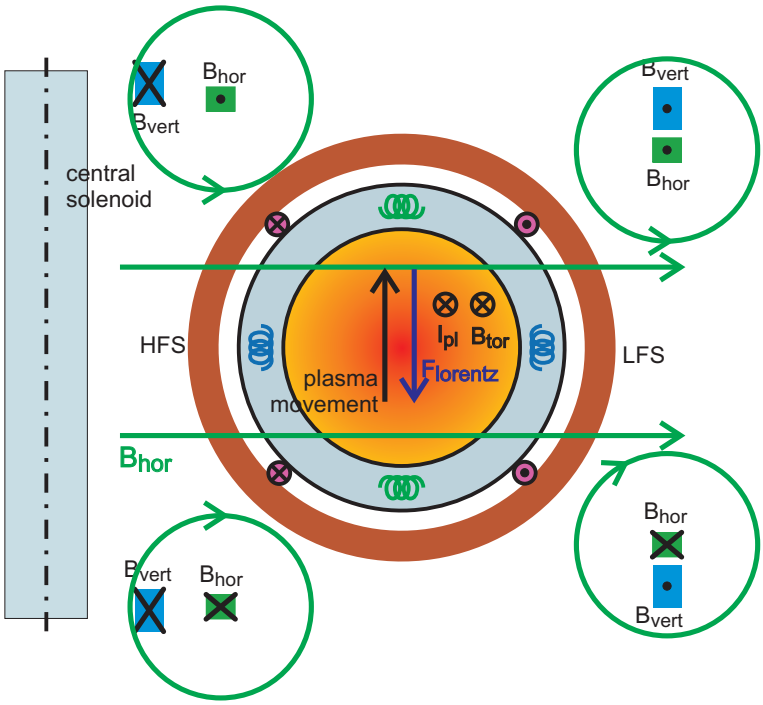

Figure 3.7: *The feed back principle. When the plasma moves up, the coils depicted as B_{hor} generate a horizontal magnetic field, which pushes the plasma back downwards by the Lorenz force. Similar effect happens in the horizontal direction. The green circles imply the magnetic field generated by individual windings of B_{hor}.*

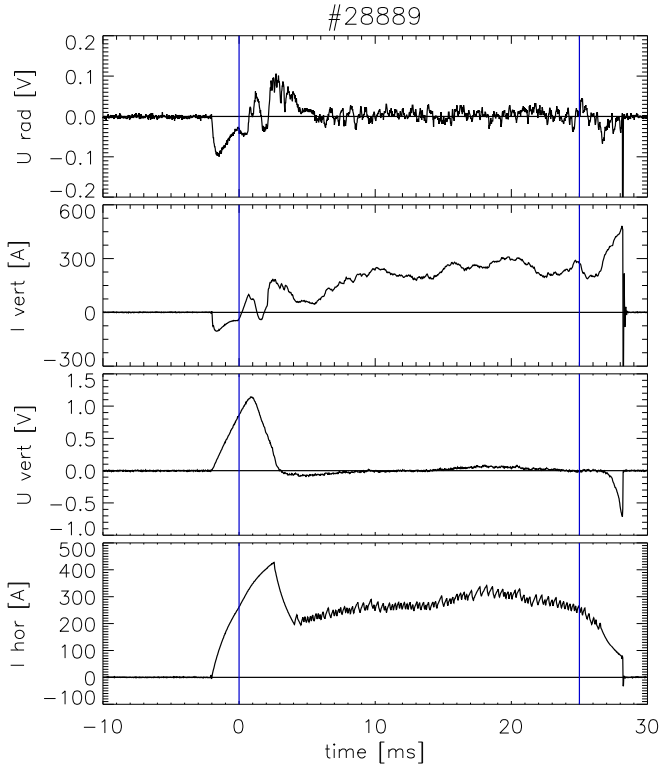

Figure 3.8: *Signals of the feed back system. U_{rad} collects information about the radial position of plasma and controls the current into the vertical magnetic field coils I_{vert} via the feed back system. In a similar way, the U_{vert} controls the horizontal magnetic field by adjusting I_{hor}. The beginning and the end of the discharge is denoted by the vertical blue lines. The feed back currents start at about 2 ms in advance in order to compensate stray magnetic fields generated by toroidal current and primary windings current.*

3.2.6 Plasma radiation

Plasma radiates in a broad range of wavelengths from microwave through the visible light up to hard X-rays (HXR). Measurements of the visible radiation can show the density of neutral hydrogen (H_α line intensity) or of the impurities such as carbon (CIII line). The HXR provides information on the behaviour of run-away electrons [7].

To monitor the plasma radiation, several detectors are installed. There are two photomultipliers equipped by interference filters measuring the intensity of H_α line at the CASTOR tokamak: one is at the position of the limiter (North-West), and the other is placed 180° toroidally from the first one (South-East) as depicted in figure 3.9. Both of them are mounted at the top of the vessel. The detector of the CIII line is located from the bottom of the North-Eastern port. The HXR detector is a photomultiplier with a NaI(Tl) scintillator located at the toroidal position of the limiter (North-West), from the top, two meters above the tokamak vessel.

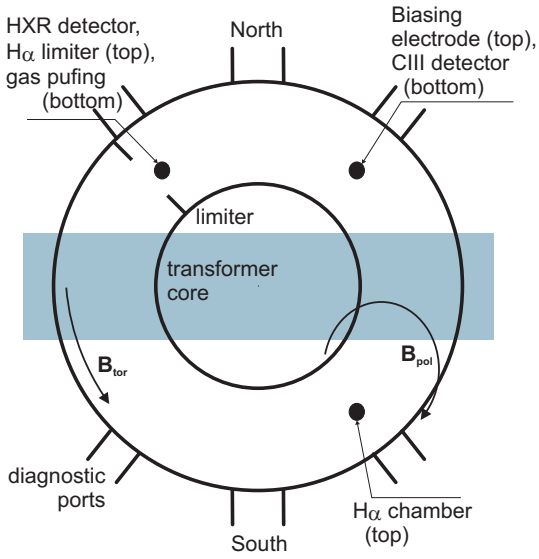

Figure 3.9: *Layout of the detectors of plasma radiation, top view. The HXR and the H_α line detector are located at the North-West port from the top, the second H_α line detector is located in the South-East port from the top. The CIII line detector is located from the bottom of North-Eastern port.*

The H_α line is the first of the Balmer series for neutral hydrogen, the transition from $n = 3$ to $n = 2$ where n is the principal quantum number. The wavelength of the H_α line is 656.28 nm, which falls into the red part of the visible spectrum. The intensity of the H_α line can be expressed as

$$I_{H_\alpha} = \frac{1}{4\pi} n_3 A_{32} \qquad [\text{photons} \cdot \text{s}^{-1} \cdot \text{m}^{-3} \cdot \text{sr},\ \text{m}^{-3},\ \text{s}^{-1}] \tag{3.6}$$

where A_{32} is the probability of transition between the states $3 \rightarrow 2$ and n_3 is the density of the atoms excited to the state $n = 3$.

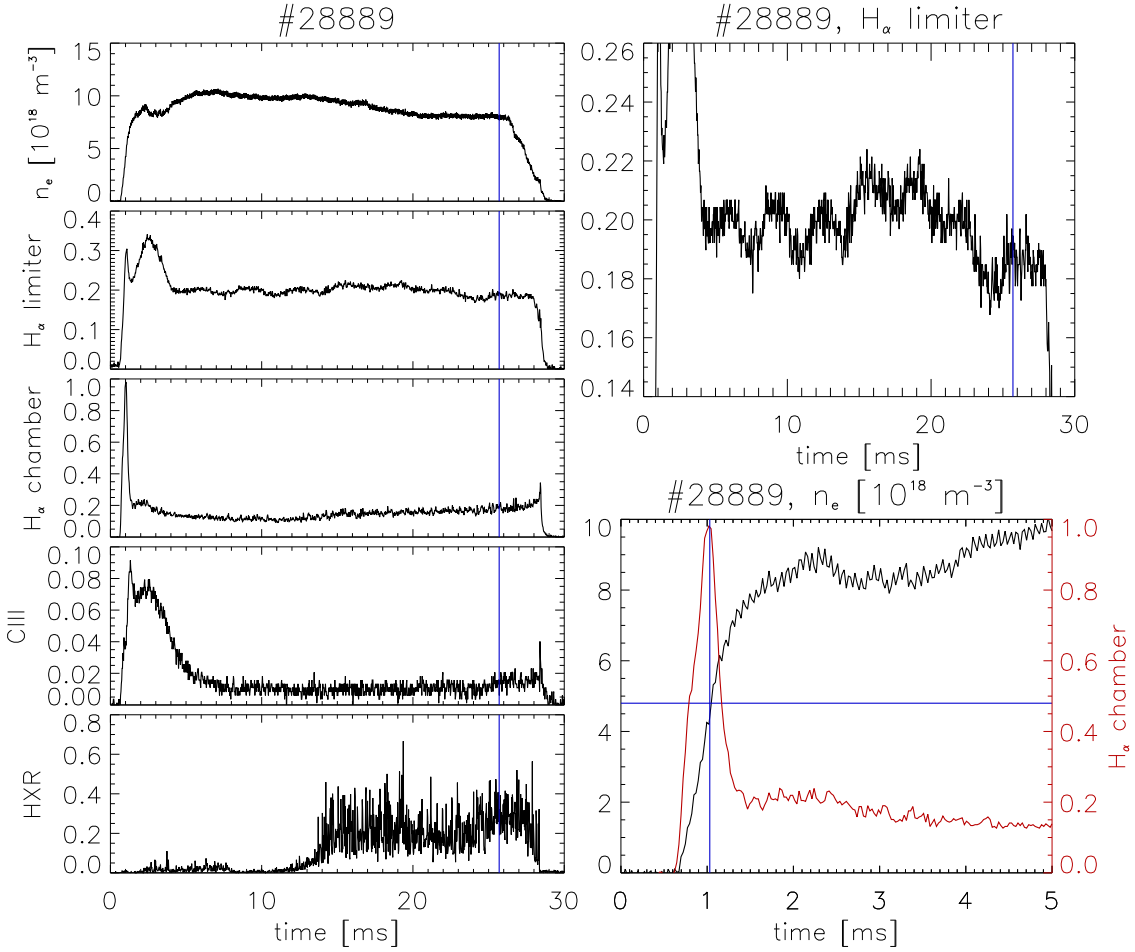

Figure 3.10: *Plasma radiation. Left panels: Temporal evolution of electron density n_e, H_α line emission at the limiter position, H_α line emission on the opposite side toroidally from the limiter, CIII line emission and HXR signal. The vertical blue line marks the end of the discharge, when the primary circuit is shorted. Right panel top: The H_α line intensity at the limiter position with emphasized scale shows periodical increasing of intensity corresponding to the gas puffing. Right bottom panel: Plasma density during the start-up phase of the discharge (black) with the H_α chamber line intensity. The time when the H_α reaches its maximum is marked by a vertical blue line. It corresponds to the half-ionization of the plasma,* i.e.*, half of the maximum of the electron density.*

The H_α line detectors give an information about the amount of atomic hydrogen. The temporal evolution of their signals are shown in figure 3.10, second and third panel from the top, left. The H_α *chamber* detector is looking directly into the chamber, thus it can see only neutrals knocked out from the vessel wall (recycling) or from the surface of probe inserted at the same toroidal position. The H_α *limiter* detector is located above the gas-puffing valve, which is installed in the bottom part of the same port. We can clearly observe periodical increasing of the H_α intensity in this detector signal as emphasized in figure 3.10, the top right panel, by enlarging the scale. The pattern is not observable in the H_α *chamber* signal, because the neutral gas ionizes close to the region of gas injection and it does not reach the place visible

by the H_α *chamber* detector.

The full ionization of the working gas as well as the maxwellization of plasma, takes place during a thermal ionization phase of the discharge (TIP) [8]. From the experimental point of view, the TIP starts when a measurable value of the H_α line intensity and the electron density can be observed. It ends when the electron density reaches its maximal value, *i.e.*, at the beginning of the quasistationary phase of discharge. The maximum of the H_α intensity corresponds to the ionization of 50% of the working gas (half of the n_e), as shown in figure 3.10 in the right bottom panel and demonstrated in [8].

The CIII line ($\lambda = 464.7$ nm) is emitted by twice ionized carbon atom C^{2+}. The main source of carbon impurities are the walls, eventually the biasing electrode, immersed into the plasma from the top just opposite to the CIII detector. A typical temporal evolution of the CIII detector signal is shown in figure 3.10.

The HXR detector collects radiation produced mainly by interaction of run-away electrons [9] with the limiter. The run-away electrons are developed from the high energy part (> 60 keV) of the velocity distribution function. The cross section of the coulomb collisions decreases with rising velocity, thus the fast electrons are accelerated by E_{tor}. The run-away electrons are generated during the avalanche phase of the discharge, *i.e.* before the electron density starts to increase [8]. Typically after ~ 15 ms, they start leaving the confinement region and they hit the limiter, mostly at the LFS close to the mid-plane. Temporal evolution of the HXR signal is shown in figure 3.10. Generation of run-away electrons depends also on plasma density: for low density discharges, the amount of run-aways is higher, for very low densities, they can carry a significant fraction of the plasma current, and consequently also a significant fraction of the ohmic energy.

3.2.7 Safety factor q

Magnetic field in tokamak is not purely toroidal as it has a helical shape. The strong toroidal current adds a poloidal component to the magnetic field. Thus, a particular magnetic field line does not come into the same poloidal position after one toroidal turn, but after several of them, after it covers a toroidal angle $\Delta\varphi$. The helicity of tokamak magnetic field can be accurately described by defining a *safety factor* q as

$$q = \frac{\Delta\varphi}{2\pi}. \tag{3.7}$$

If q is irrational, one magnetic field line covers the whole magnetic surface and any fluctuation can spread quickly and homogeneously. On the contrary, if q is a small rational or even a natural number, individual parts of the magnetic surface do not communicate and instabilities like magnetic islands can arise.

The safety factor depends on the geometry of the machine and it varies along the minor radius. For large aspect ratio tokamaks ($\epsilon = R/a$) with circular poloidal cross-section (as in the case of CASTOR), q can be written as [4]

$$q(r) = \frac{r}{R}\frac{B_{tor}}{B_{pol}(r)} \tag{3.8}$$

where r and R are the minor and major radii, while B_{tor} and B_{pol} are the toroidal and poloidal magnetic fields. B_{pol} can be expressed as

$$B_{pol}(r) = \frac{\mu_0}{2\pi}\frac{I_{pl}(r)}{r} = \frac{\mu_0}{2\pi}\frac{I_{pl}(a)}{r}\left[1 - \left(1 - \frac{r^2}{a^2}\right)^{p+1}\right] \tag{3.9}$$

where I_{pl} is the plasma current which is driven within the radius r. Substituting (3.9) into (3.8), $q(r)$ can be written as

$$q(r) = q(a)\frac{r^2/a^2}{1-(1-r^2/a^2)^{p+1}} \tag{3.10}$$

where $q(a)$ is the edge safety factor:

$$q(a) = \frac{2\pi}{\mu_0}\frac{a^2}{R}\frac{B_{tor}}{I_{pl}(a)}. \tag{3.11}$$

A radial profile of the *normalized safety factor* $q(r)/q(a)$ is shown in figure 3.11.

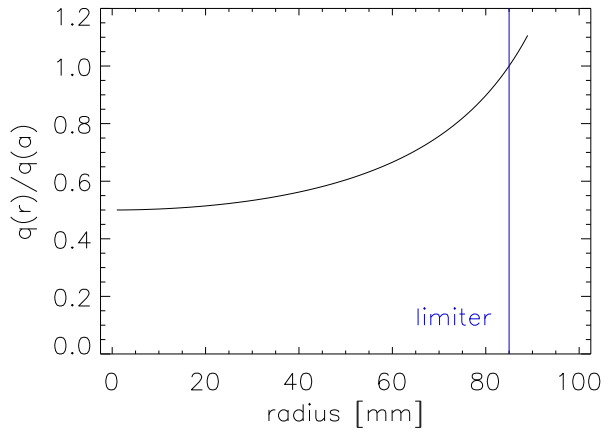

Figure 3.11: *Radial profile of the normalized safety factor. The vertical blue line indicates the limiter position.*

For the edge of CASTOR tokamak ($a = 85$ mm), we can write

$$q(a) = 90.3 \cdot \frac{B_{tor}}{I_{pl}} \qquad [\mathrm{T}, \mathrm{kA}]. \tag{3.12}$$

This is true in an ideal case when the plasma column is centralized with the poloidal circumference $a = 85$ mm. If the plasma is shifted, the constant in the formula (3.12) has to be modified.

Temporal evolution of $q(a)$ during a typical discharge is shown in figure 3.12.

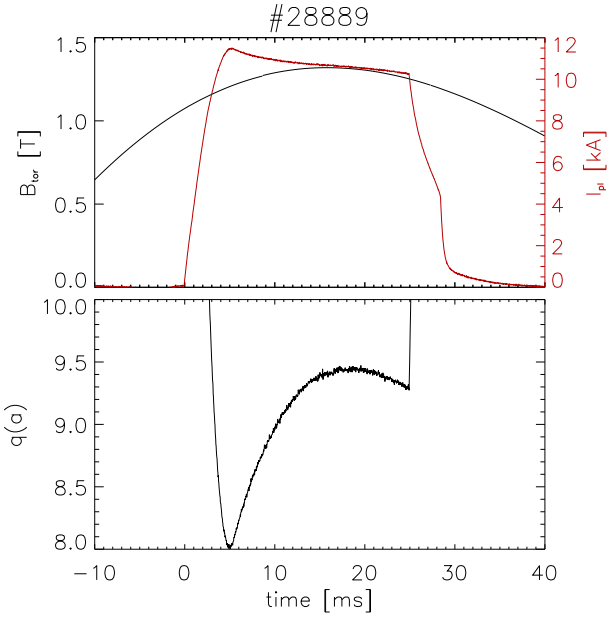

Figure 3.12: *Temporal evolution of the safety factor $q(a)$ (bottom panel). In the top panel, the toroidal magnetic field B_{tor} is shown. The discharge is depicted by the plasma current I_{pl} (red line). The calculation was performed for $a = 78$ mm.*

3.2.8 Determination of electron temperature and density

Electron temperature

The electron temperature profile $T_e(r)$ is used in many calculations but not routinely measured at the CASTOR tokamak. Experimental measurements were performed at the plasma edge only, by swept Langmuir probes [10]. The resulting profiles are presented in section 4.3.5.

An estimation of the central electron temperature $T_e(0)$ can be obtained from the following considerations: The current density of plasma is

$$j = E \cdot \sigma \tag{3.13}$$

where σ is the specific conductivity of plasma given by

$$\sigma(r) = 1.544 \cdot 10^3 \cdot \frac{T_e(r)^{3/2}}{Z_{eff}}, \qquad [\Omega^{-1}\mathrm{m}^{-1}, \mathrm{eV}] \tag{3.14}$$

and the electric field E is assumed constant in the poloidal cross-section:

$$E = \frac{U_{loop}}{2\pi R}. \tag{3.15}$$

Plasma current is obtained by integrating current density over the plasma column:

$$I_{pl} = \int_0^a E \cdot \sigma(r) 2\pi r dr. \tag{3.16}$$

Using (3.14) and (3.15) in (3.16) we can write

$$\frac{I_{pl}}{U_{loop}} \cdot 2\pi R \cdot \frac{Z_{eff}}{1.544 \cdot 10^3} = \int_0^a T_e(r)^{3/2} 2\pi r dr. \tag{3.17}$$

For the electron temperature, we assume a polynomial profile

$$T_e(r) = T_e(0)\left(1 - \frac{r^2}{a^2}\right)^{\alpha} \tag{3.18}$$

where a is the minor radius and $T_e(0)$ is the electron temperature in the centre of the plasma column. We assume $\alpha = 2$, thus the integral on the right side of equation (3.17) can be calculated as

$$\int_0^a T_e(0)^{3/2}\left(1 - \frac{r^2}{a^2}\right)^3 2\pi r dr = 2\pi \cdot T_e(0)^{3/2} \cdot \frac{a^2}{8}. \tag{3.19}$$

Substituting (3.19) into (3.17) gives us the formula for the central electron temperature

$$T_e(0) = \left(\frac{R}{a^2}\frac{8 \cdot Z_{eff}}{1.544 \cdot 10^3}\right)^{2/3} \cdot \left(\frac{I_{pl}}{U_{loop}}\right)^{2/3}. \tag{3.20}$$

For the CASTOR tokamak geometry with $a = 78$ mm (plasma shift is 7 mm downwards, see section 4.3.1):

$$T_e(0) = 89.8 \cdot \left(\frac{I_{pl}\ [kA]}{U_{loop}}\right)^{2/3} \approx 230\ eV. \tag{3.21}$$

The effective ion charge is assumed as $Z_{eff} = 2.5$. The result is over-estimated in comparison to previous evaluations from H_α measurements ($T_e \approx 150 - 200$ eV) [11]. The difference may be caused by neglecting energy losses in the presented calculation.

The temporal evolution of $T_e(0)$ is shown in figure 3.13 in the top panel.

Electron density

The line averaged density is measured by a microwave interferometer, its temporal evolution during a typical discharge is shown in figure 3.3. Assuming parabolic density profile (A-21), we can express the relation between the measured $n_{e\ meas}$ and the central electron density $n_e(0)$ as

$$n_e(0) = \frac{3}{2} n_{e\ meas}. \tag{3.22}$$

Detailed calculation is given in appendix A-2.

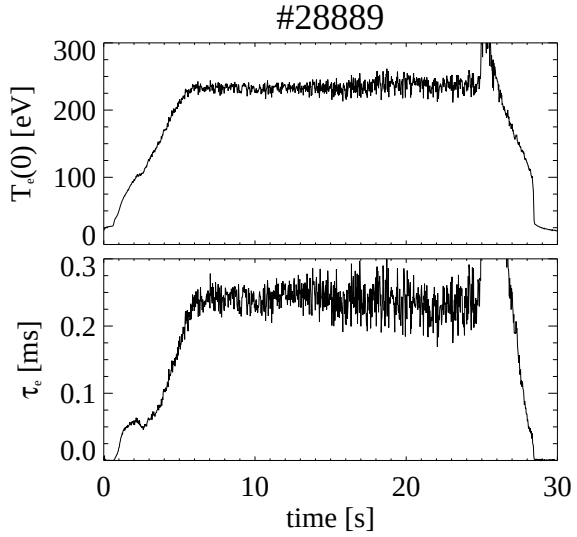

Figure 3.13: *Temporal evolution of the central electron temperature $T_e(0)$ (top panel) and of the energy confinement time τ_e (bottom panel) for a typical CASTOR discharge.*

3.2.9 Electron confinement time

The *electron confinement time* τ_e can be estimated as the ratio of the energy stored in the electron component of the plasma Q_e and of the ohmic power P_{oh}:

$$\tau_e = \frac{Q_e}{P_{oh}}. \tag{3.23}$$

The total energy stored in the electron component of the plasma can be obtained from

$$Q_e = \frac{3}{2} \langle T_e(r) n_e(r) \rangle \cdot V_{tor} \qquad T_e,\ n_e,\ V_{tor}\ \ [\mathrm{J},\ \mathrm{m}^{-3},\ \mathrm{m}^3] \tag{3.24}$$

where $V_{tor} = \pi a^2 \cdot 2\pi R$ is the plasma volume and $\langle T_e(r) n_e(r) \rangle$ is the product of electron temperature and density

$$\langle T_e(r) n_e(r) \rangle = \frac{1}{4} T_e(0) \cdot n_e(0) \tag{3.25}$$

as shown in appendix A-2. Introducing (3.25) into (3.24), we obtain

$$Q_e = \frac{3}{8} V_{tor} \cdot T_e(0) \cdot n_e(0). \tag{3.26}$$

Finally, the energy confinement time τ_e derived from equation (3.23) by substituting equation (3.26) and (3.5) (page 16), can be written as

$$\tau_e = \frac{3}{8} V_{tor} \frac{T_e(0) \cdot n_e(0)}{U_{loop} \cdot I_{pl}} \approx 0.25 \text{ ms} \qquad T_e,\ I_{pl}\ [\mathrm{J},\ \mathrm{kA}]. \tag{3.27}$$

Temporal evolution obtained from experimental data is shown in figure 3.13, bottom panel.

This was a rough estimation of the τ_e. A proper calculation requires to include the radiative power loss and the energy stored in ion component, as is described in [12] and [13]. Similar results ($\tau_e \simeq 0.3$ ms) were obtained from measurements of plasma diamagnetism [14].

3.3 Diagnostics

Tokamak CASTOR is equipped by a set of basic diagnostics for measurements of the main plasma parameters such as the loop voltage, the plasma current, and the averaged plasma density as well as the plasma radiation and magnetic properties. The main emphasis of the physical programme of the facility is on measurements of the edge plasma. For this purpose, several arrays with high space and temporal resolution were constructed and several advanced probes were developed. In this section, we focus on the most important diagnostic tools for the turbulence measurements, used in this work.

3.3.1 Langmuir probe arrays

Several arrays of Langmuir probes were developed for measurements in the edge region of the CASTOR tokamak. The required spatial resolution is in the order of millimetres, the temporal resolution should be 1 μs, if not indicated otherwise. The probes work either in the floating potential regime, or they collect the ion saturation current. An electronic circuit of an individual probe is shown in figure 3.14.

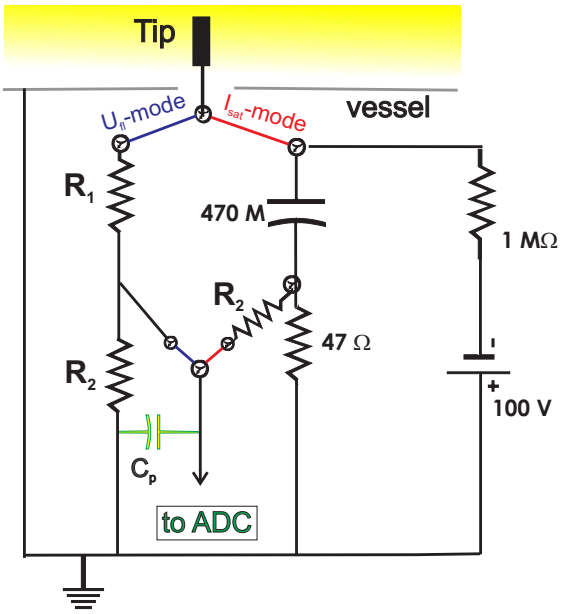

Figure 3.14: *Circuit of the connection of one Langmuir probe. The blue and red lines depict connection for measuring the floating potential and the ion saturation current, respectively. The resistors are* $R_1 = 620k\Omega, R_2 = 6.2k\Omega$.

Rake probe

The rake probe is a radial array of 16 Langmuir tips made of molybdenum, spaced by 2.5 mm. A picture of the probe is shown in figure 3.15 in the left panel. The support is inserted into a quartz sleeve. The probe is immersed into the plasma from the top of the chamber in most of the experiments, in some of them from the LFS at the mid plane.

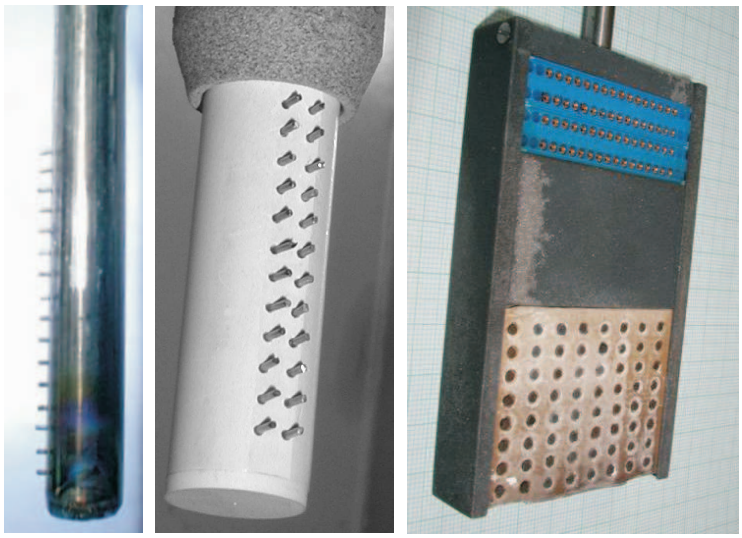

Figure 3.15: *Arrays of Langmuir probes. Left panel: the single rake probe, central panel: the double rake probe. Right panel: the 2D probe array; the bottom part shows the Langmuir probe tips, the blue top part contains connectors for the conductors leading the signal out from the vacuum vessel. This part is in the diagnostic port.*

Double rake probe

The double rake probe is a radial array of 24 Langmuir tips (two rows each of 12 tips). They are made of molybdenum, spaced by 2.5 mm in the radial as well as in the poloidal direction, as shown in figure 3.15 in the middle panel. The support is made of machinable ceramics (boron-nitride). The probe is immersed into plasma from the top of the chamber, facing the upstream with respect to the magnetic field lines (and the plasma current).

2D probe array

The 2D probe array [15] is a two-dimensional matrix of 64 graphite tips (8×8) with spacing of 6 mm in the poloidal direction and 4.5 mm in the radial direction as shown in figure 3.15, right panel. The tips are held by a support made of boron-nitride.

The 2D matrix is inserted into the plasma from the top of the chamber, oriented either upstream, or downstream with respect to the magnetic field lines.

Poloidal ring

The poloidal ring [16, 18] consists of 124 Langmuir probes made of molybdenum, located on a circumference of a stainless steel ring with the radius of 58 mm, as shown in figure 3.16. The probes have the length of 2.5 mm and the diameter of 0.6 mm, their poloidal distance is 3 mm. This ring plays the role of an additional limiter.

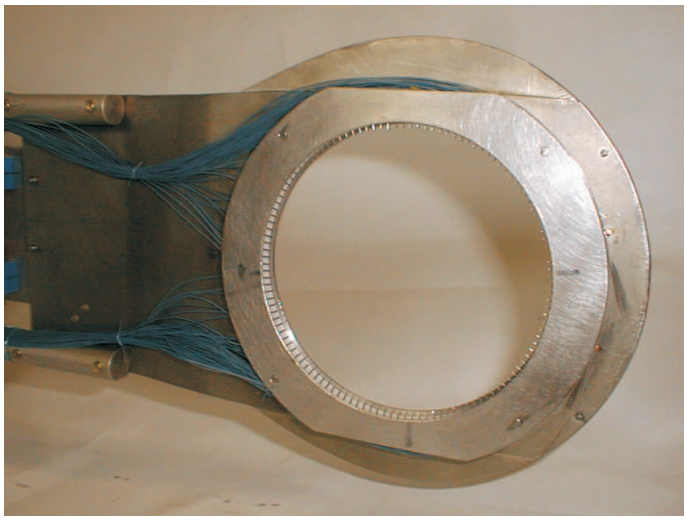

Figure 3.16: *Poloidal ring.*

SK ring

Another poloidal array named "SK ring" [17] consists of 96 Langmuir probes, moreover 16 magnetic coils are added as apparent from figure 3.17. This ring is placed slightly behind the limiter ($r = 87$ mm), the individual Langmuir probes are made of molybdenum wire with the length of 2 mm and the diameter of 0.6 mm. Their poloidal distances are thus 5.7 mm. The probes can measure local electric parameters, while the coils detect changes in the magnetic field, caused by magnetic islands in the plasma core.

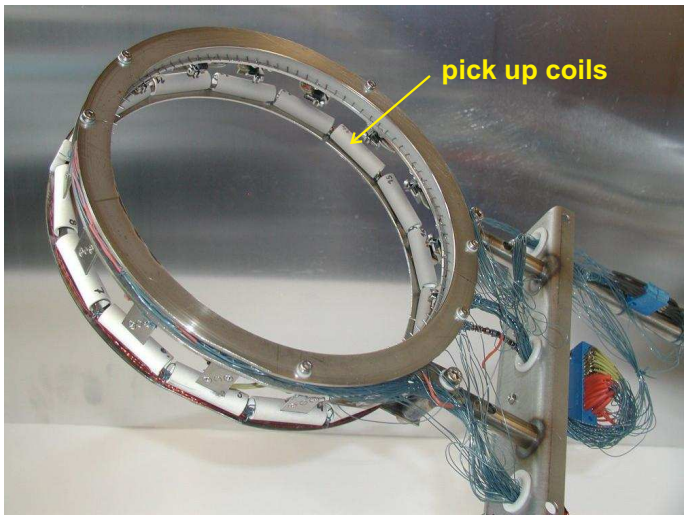

Figure 3.17: *SK ring. The white segments are covers of the 16 magnetic coils, while the Langmuir tips are embedded in a PTFE ring protected by a stainless steel diaphragm.*

3.3.2 Advanced probes

Ball-pen probe

The Ball-pen probe is a novel type of probe, which was developed in IPP Prague to measure directly the plasma potential [19, 20]. This probe, which is based on the Katsumata probe concept [21], consists of a movable collector with a conical tip housed inside an insulating boron-nitride shielding, as shown in figure 11.1. The collector can be moved radially, and adjusted in order to collect equal fluxes of ions and electrons, due to the shadowing effect of the shielding. When such condition is reached, and the collector is floating, the collector potential will be equal to the plasma potential.

Another application of the probe is to study the spatial decay of the fluctuation power spectrum inside the shaft for different collector positions. From these data, the plasma diffusion coefficient is derived. Part III is devoted to the detailed description of the method as well as of the probe itself.

Gundestrup probe

The Gundestrup probe [22] is designed for direction-sensitive measurements of ion flows. It consists of eight segments, placed on an insulating boron-nitride housing, facing all sides as shown in figure 3.18. The segments are made of a copper cylindrical conductor with the diameter of 11.7 mm, divided into the segments, which are separated by a gap of 0.2 mm. The whole probe is covered by a quartz sleeve which determines the radial extent of the active area of the segments. Thus, each segment has the active area 11.4 mm × 2.2 mm. The segments are biased at the

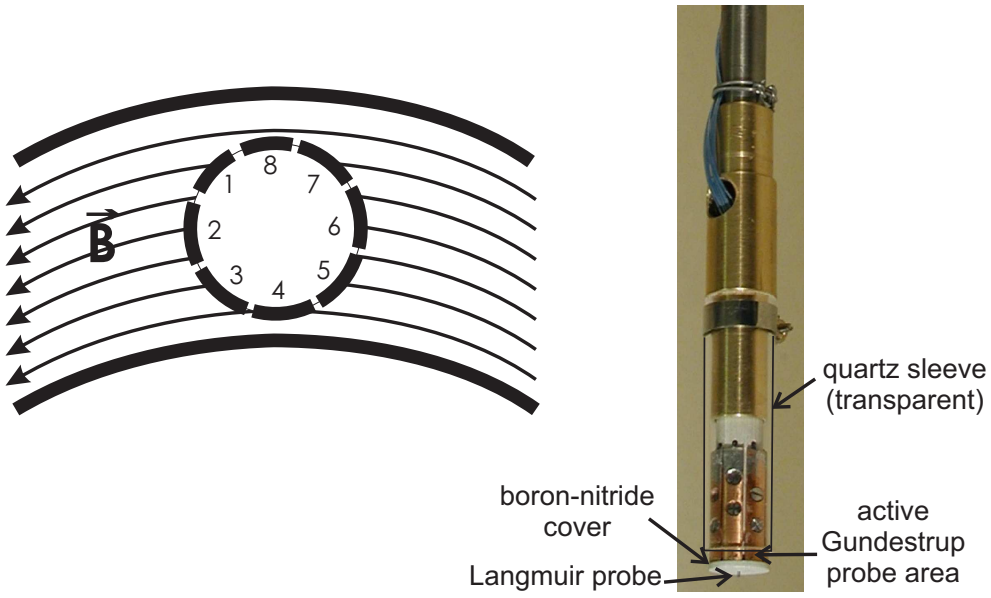

Figure 3.18: *Gundestrup probe. Left panel: Orientation of the probe with respect to the tokamak vessel, top view. Right panel: A photo; the quartz sleeve is emphasized by the black frame.*

ion saturation current. Moreover, a single Langmuir probe (1.25 mm length and 0.6 mm diameter) is located on the top of the Gundestrup probe, insulated by a boron-nitride cover (1.8 mm thick). The Langmuir probe is swept by a triangular voltage in order to get the voltage current characteristics to determine the local electron temperature and density in front of the Gundestrup probe.

Segmented tunnel probe

The segmented tunnel probe (STP) [23, 24] was developed for ion temperature measurements. It consists of two hollow tunnels with axis parallel to the B_{tor}: one is upstream (facing the ion current) and the second one is downstream oriented (facing the opposite side). One tunnel has the diameter and depth of 5 mm. It is ended with a copper back plate, the inner sides are made of two copper rings as depicted in figure 3.19 in the left panel. Each of this part is negatively charged to measure the ion saturation current. In the proximity of the probe orifice, four Langmuir probes are installed to measure the floating potential. An overview picture is in figure 3.19 in the right panel.

The segmented tunnel probe is inserted from the top of the chamber. The ions flowing into the probe are demagnetized by a strong electric field and redistributed among the back plate and the rings. The ratio of the currents flowing to the segments (the inner copper rings) and to the back plate is a function of electron temperature. The sum of the currents to the individual conductors divided by the area of STP orifice gives the parallel ion current density. The ratio of the current flowing to the first and to the second inner ring is proportional to the parallel ion temperature.

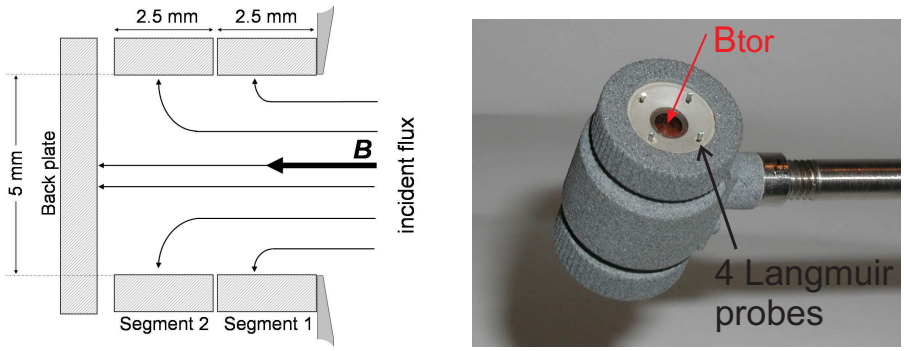

Figure 3.19: *The segmented tunnel probe. Left panel: Schema of one tunnel, right panel: Picture of the whole probe.*

Chapter 4

Edge plasma

In this chapter, we give a brief description of a basic information about two kinds of geometry of Scrape Off Layer in tokamaks and about transport in this region. The specific geometry of the CASTOR edge plasma is described and the most important parameters characterizing the CASTOR edge plasma are shown.

The concept of magnetic confinement is to keep plasma inside a vacuum chamber with a help of a strong magnetic field. In reality, the plasma will always escape from the trap due to various drifts, diffusion processes and turbulence. The plasma column will decay to the vessel inner walls and the particles of the plasma will interact with the wall.

The plasma-surface interaction (PSI) is an important issue in the magnetic fusion research since it is responsible for:

1. recycling of the fuel (hydrogen) atoms,
2. bringing impurities into the plasma,
3. erosion of the inner vessel walls,
4. cooling the edge plasma.

As noted in section 2.2.1, the helical magnetic field creates concentric magnetic flux surfaces (see figure 2.6). The surfaces which are not connected with any solid material are called *closed* while the magnetic surfaces which come through solid surfaces (wall, limiter) are called *open*. The *Last Closed* (magnetic) *Flux Surface* (LCFS) is important in the edge plasma physics terminology: it divides the plasma boundary into the confinement region with closed flux surfaces (inwards of the LCFS), and the *Scrape Off Layer* (SOL) with open flux surfaces.

4.1 Scrape Off Layer

The shape of the edge plasma region is different for different magnetic confinement devices. In general we distinguish two main types: the *limiter* and the *divertor* configuration. The limiter as well as the divertor act as a *plasma sink*.

4.1.1 Limiter configuration

The simplest configuration is made by using some kind of limiter. Inserting a limiter into the chamber enables to determine the shape of the plasma and the connection length in the SOL and in the limiter shadow. Using a limiter also enables to influence the plasma-wall interaction by choosing a suitable material. For example, in the case of the CASTOR tokamak, the limiter is made of molybdenum. If the limiter was not there, the plasma would pollute itself by massive sputtering the iron walls.

The most often used shapes of limiters are the poloidal or toroidal. A *poloidal limiter* is a metal annulus placed in one or more poloidal positions. It is used in devices with circular cross-sections such as the CASTOR tokamak or the FTU tokamak. A typical distance, which a particle has to travel in the SOL before hitting the limiter, is termed the *connection length* and it is equal to

$$L \approx \frac{\pi R}{n_{lim}} \tag{4.1}$$

where n_{lim} is the number of poloidal limiters. The distance in between two solid surfaces of the limiter(s) is $2L$. A picture of a poloidal limiter of the FTU tokamak is shown in figure 4.1.

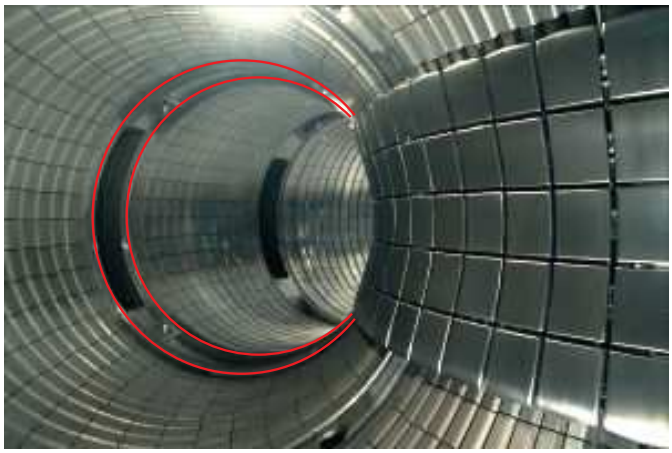

Figure 4.1: *Poloidal limiter of the FTU tokamak pointed up by red lines.*

A *toroidal limiter* is a rail, covered by protecting plates, inserted into the plasma in the toroidal direction, usually from the bottom of the vessel, as in the tokamaks Tore Supra or TEXTOR. The toroidal limiter of Tore Supra is shown in figure 4.2. The connection length L is longer with this configuration, as the particles need to go around the chamber several times before hitting the solid surface. L depends on the pitch angle via the safety factor q and we can be expressed it as

$$L = \pi R q. \tag{4.2}$$

Any object inserted into plasma can play the role of a limiter, if it is large enough to close the magnetic field lines on itself. Another type of limiter is so-called *wall-limiter*, means that the plasma touches directly the walls. Advantage of this configuration is the distribution of power to a large surface.

Figure 4.2: *Toroidal limiter of the Tore Supra tokamak placed at the bottom of the chamber.*

4.1.2 Divertor configuration

The characteristic feature of the arrangement using a divertor configuration is that the LCFS does not touch any material surface as in the case of limiter.

The divertor configuration is schematically shown in figure 4.3. It is formed by a toroidal conductor carrying a current I_d, parallel with the plasma current I_p. These two currents create an eight-shaped magnetic surfaces. In between these two conductors, a magnetic *X-point* exists, it is the place where the poloidal magnetic field is equal to zero. The Last Closed Flux Surface passing through this point is termed *separatrix*. The mostly used configuration shown in figure 4.3 is called a *poloidal divertor* and corresponds to the toroidal limiter.

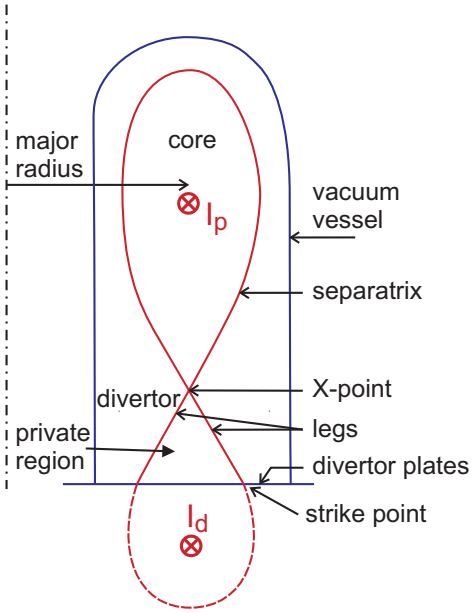

Figure 4.3: *Principle of divertor.*

As the confined plasma is separated from solid surfaces (which play role of the source or impurities) and therefore remains purer, the divertor configuration is better than the limiter one. Divertor configuration permits us to reach so-called *plasma detachment* [25, 39], moreover, the strong magnetic shear around X-point is a very efficient ingredient for transition into *H-mode* (improved confinement) [25, 39].

A construction of a divertor is more difficult than the construction of a limiter since it requires an external poloidal coil conducting high current (comparable with the plasma current). This configuration is therefore used in the European facilities such as JET, COMPASS, ASDEX, TCV and MAST, and it is designed also for the tokamak ITER. For large devices with high energy stored in plasma, the geometry of divertor tiles must be done in a special way, in order to maximize surface touched by plasma and thus to minimize the energy flux to divertor plates. A detail of the ITER divertor is shown in the figure 4.4.

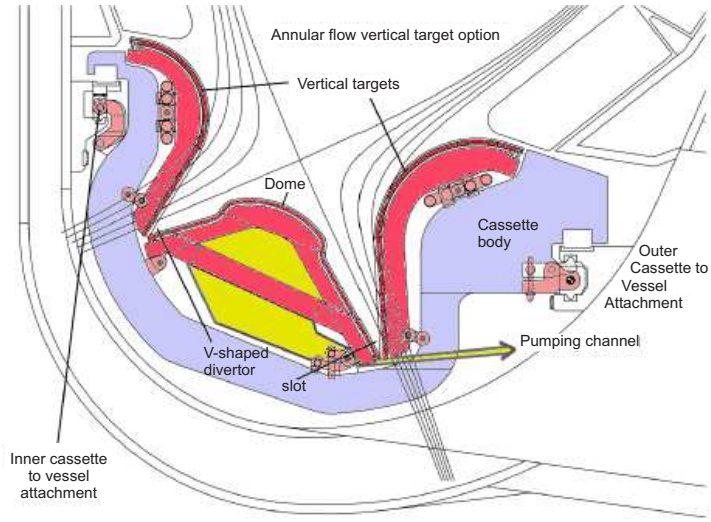

Figure 4.4: *Scheme of a divertor designed for ITER.*

4.1.3 Geometry of SOL

The SOL can be unfolded and straightened into an orthogonal block as shown in figure 4.5. The shape is bounded by:

- Opposite solid surfaces. These can be two surfaces of poloidal limiters or two sides of a single one, or two sides of the flux tube touching the poloidal limiter or entering the divertor. The surface is usually not perpendicular to the magnetic field lines. In this case, we need to take the orthogonal projection of the surface. The distance between the two solid surfaces is $2L$.
- The LCFS or separatrix on the top of the block, and chamber wall at the bottom.
- The last two sides can be defined in an arbitrary way. One can for example take $w = 1$ m to have a "unit" portion of SOL or w equal to one tile extent. They are always perpendicular to both the B and the radial direction. We will use this boundary as two sides of one cut, in order to include the whole plasma volume in our cube.

For a tokamak with circular poloidal cross-section, single poloidal limiter and centralized plasma column, the dimensions of the block are: $w = 2\pi a$, $2L$, and the width of the limiter, as depicted in figure 4.6.

4.2 Transport in Scrape Off Layer

4.2.1 Characteristic time in SOL

The projection of the particle velocity in the direction of toroidal magnetic field is similar when compared to the ion sound speed c_S. The *characteristic particle dwell*

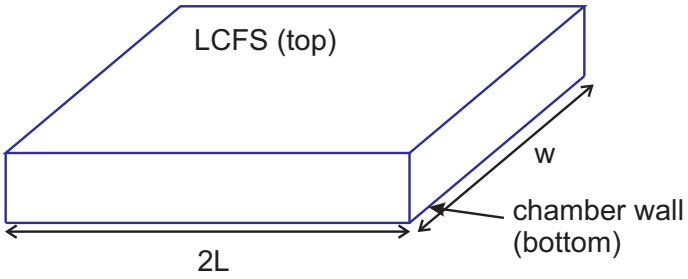

Figure 4.5: *Scheme of unfolded SOL.*

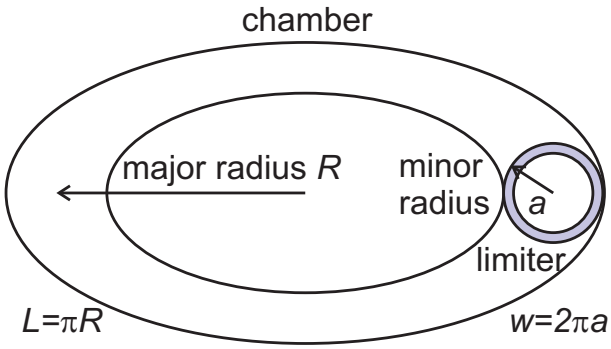

Figure 4.6: *SOL of a tokamak with one poloidal limiter and a circular cross-section.*

time in the SOL is

$$\tau_{SOL} = \frac{L}{c_S}. \tag{4.3}$$

For the tokamak CASTOR in the shadow of limiter, the $L = \pi R$. The $L \simeq 1.3$ m since the major radius $R = 0.4$ m. The temperature in the SOL is ~ 10 eV, thus the $c_S \approx 4 \cdot 10^4$ m s^{-1}. The $\tau_{SOL} \simeq 0.03$ ms. For JET-sized tokamaks with toroidal divertor, $L = \pi R q$. For the major radius of ~ 3 m and $q = 4$, $L \approx 40$ m. The temperature in the SOL is typically $1 - 100$ eV, then the $c_S \approx 10^4 - 10^5$ m s^{-1}. The $\tau_{SOL} \approx 0.4 - 4$ ms.

4.2.2 Diffusion coefficient in SOL

Diffusion across the magnetic field lines is very important for plasma confinement. While the *diffusion coefficient* in the confined region is an empirical value, not possible to be calculated theoretically, the diffusion in the SOL can be estimated from simple principles.

For a rough estimation of the *diffusion coefficient in the SOL* $D_\perp^{SOL}$, we can use the following consideration. In the SOL, the velocity of particles along the magnetic field lines (in the toroidal direction) dominates the velocity in the perpendicular direction. Thus, the source of particles is the LCFS - the particles are penetrating from the confined area. Once they reach the SOL, they leave in the parallel direction to the limiter or the divertor tiles.

The total particle flux coming from the confined area through LCFS is

$$\gamma_\perp = -D_\perp^{SOL} \left.\frac{\mathrm{d}n}{\mathrm{d}r}\right|_{LCFS} S \tag{4.4}$$

where $S = 2Lw$ is the surface of LCFS (see figure 4.5). Defining the *characteristic length of radial density decay* λ_n as

$$\lambda_n \equiv -\left(\frac{1}{n}\frac{\mathrm{d}n}{\mathrm{d}r}\right)^{-1}, \tag{4.5}$$

the decrease of the density in the SOL can be expressed as

$$\frac{\mathrm{d}n}{\mathrm{d}r} = -\frac{n}{\lambda_n} \tag{4.6}$$

and

$$\gamma_\perp = -D_\perp^{SOL} \frac{n_{LCFS}}{\lambda_n} S. \tag{4.7}$$

The total particle flux in the parallel direction is

$$\gamma_\parallel = 2w \int_{r=LCFS}^{\infty} n c_S \mathrm{d}r \tag{4.8}$$

with using Bohm/Chodura sheath criteria [25]. Assuming that the $n(r)$ is exponential

$$n(r) = n_{LCFS} e^{-r/\lambda_n} \tag{4.9}$$

and the $c_S(r)$ is constant, the particle flow (4.7) can be written as

$$\gamma_\parallel = 2w \frac{1}{2} n_{LCFS} c_S \lambda_n. \tag{4.10}$$

The particle balance says that all the particles coming from the SOL in the perpendicular direction ($\gamma_\perp$) leave to the limiter in the parallel direction ($\gamma_\parallel$) due to higher velocity in the parallel direction, thus we can write $\gamma_\perp = \gamma_\parallel$. It gives

$$D_\perp^{SOL} = \frac{c_S \lambda_n^2}{2L}. \tag{4.11}$$

It is worth noting that the introduced model has certain limitations. Recent research shows that the transport is significantly influenced by turbulence. Blobs and ELMs present in the edge plasma can increase the convection and consequently raise the transport by order of magnitude. As the turbulence is developed in the inner layers of plasma, the diffusion coefficient is not a local variable anymore, it depends also on parameters in the confinement area. The model described in the equations (4.4)–(4.11) is thus only a rough approximation.

4.3 CASTOR edge plasma

4.3.1 Geometry of the CASTOR edge plasma

CASTOR tokamak has a specific geometry of the edge plasma. The plasma column is typically shifted downward because of insufficient capabilities of the feed back system which controls the plasma position. The poloidal cross-section is schematically shown in figure 4.7. We can distinguish three areas: the confinement area (core), the Scrape Off Layer (SOL), and the shadow of the limiter. In the confinement area, the magnetic field lines are closed or infinite. In the shadow of the limiter, the connection length is only one half of a single turn along the torus. Completely different situation is in the region labelled as SOL: The connection length is several turns along the chamber, and the magnetic field lines are terminated at the limiter surface. The number of turns depends on the safety factor q (see section 3.2.7).

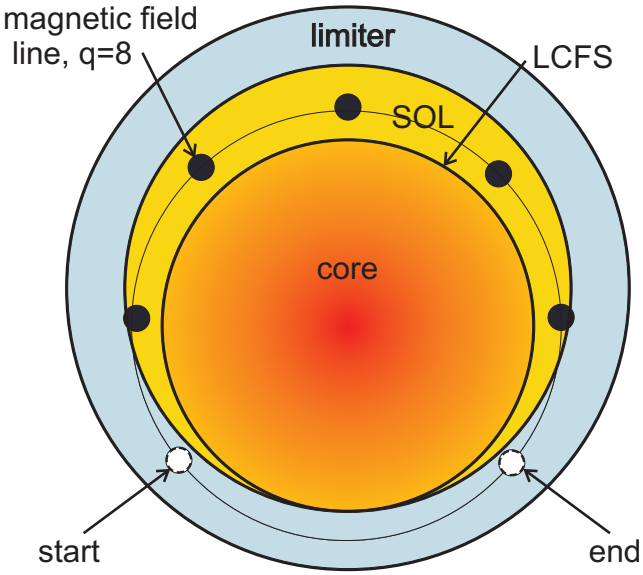

Figure 4.7: *Vertical shift of plasma in the CASTOR tokamak. Black and white circles demonstrate intersections of a magnetic field line and the poloidal cross-section.*

Such configuration was experimentally confirmed by measurements of radial and poloidal profiles of floating potential, described in following text. The subsections 4.3.3-4.3.6 concern about "typical profiles" of ohmic discharge. A significantly different regime is reached by biasing of the edge plasma, explained in chapter 5.

4.3.2 Connection length of the CASTOR edge plasma

The connection length L is not uniform along the radius, as is implied in section 4.3.1. Radial profile of L is shown in figure 4.8. In the limiter shadow, $L_{lim} = \pi \cdot R$ (equation (4.1)). At the LCFS, the situation corresponds to a toroidal limiter at the bottom of the chamber, thus $L_{LCFS} = q \cdot R \cdot \pi$. In between, the L varies linearly in the midst of these two values.

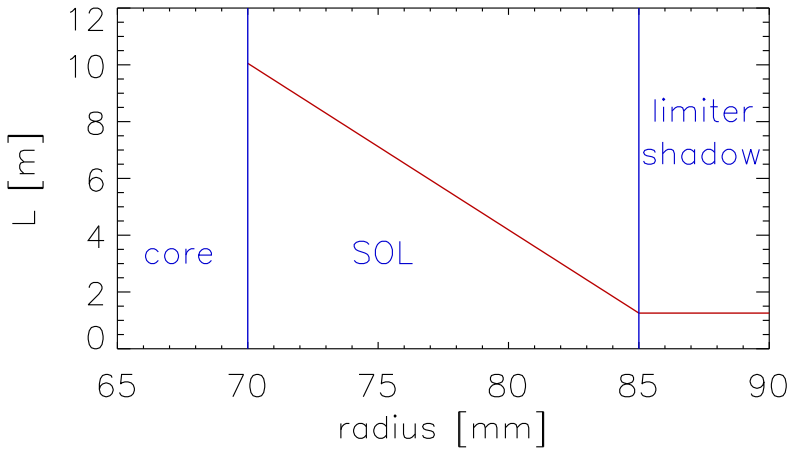

Figure 4.8: *Radial profile of the connection length for CASTOR edge plasma for* $q(70) = 8$.

4.3.3 Radial profile of floating potential

Radial profile of floating potential at the plasma edge is presented in figure 4.9. The profile is obtained from the rake probe (3.3.1) inserted from the top of the vacuum vessel. The CASTOR tokamak has no possibility of magnetic reconstruction of the plasma shape, radial profile of U_{fl} was therefore a clue how to disclose the position of the LCFS.

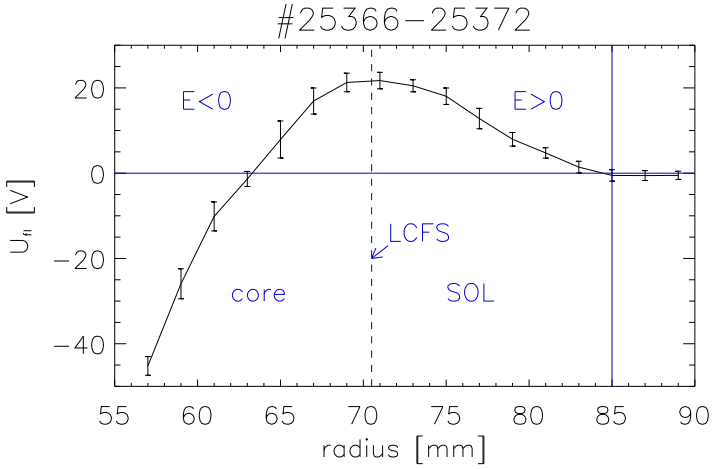

Figure 4.9: *Radial profile of the floating potential [10].*

Once plasma reaches the limiter, it decays on it. More electrons escape to the limiter due to their higher mobility, thus the area in the shadow of the limiter is being charged positively. As the plasma protrudes from the LCFS out, more electrons end up at the limiter surface and the potential decreases in this area. This imbalance is proportional to the temperature, that is another reason why we can observe a maximum of the floating potential near the LCFS, as marked in figure 4.9. In the

direction to the core, the floating potential drops and it gets negative values in the plasma bulk. It is caused by ion orbit losses: due to larger Larmor radius, the ions escape faster.

One more effect contributes to the shape of the radial profile of U_{fl}, which is caused by a turbulent process. The Reynolds stress (also termed tilting instability) [26] generates a poloidal velocity shear $\mathrm{d}v_{pol}/\mathrm{dr}$, yielding related radial electric field: $E_{rad} = B_{tor} \times v_{pol}$. The direction of this field depends on a trigger mechanism and can be randomly positive or negative; the shape of the U_{fl} profile, however, does not qualitatively change. It implies that the ion orbit loss mechanism must dominate the E_{rad} profile. Quantifying this mechanism requires complex numerical simulations.

It is obvious from figure 4.9 (and figure 4.7) that in the upper part of the chamber, the position of the LCFS does not correspond to the limiter position. This discrepancy between the measurements with Langmuir probes and the feed back system was explained by measurements using Hall sensors: the feed back coils for measurements of the plasma position are affected by an additional magnetic field generated by other sources than the plasma current [27].

4.3.4 Poloidal profiles of floating potential and velocity

The downward plasma shift can also be deduced from the poloidal distribution of the floating potential (U_{fl}) obtained from the poloidal ring of Langmuir probes (section 3.3.1), plotted in figure 4.10. In the upper part of the circumference, the U_{fl} is positive, which indicates that the probes are in the SOL, according to the profile shown in figure 4.9. In the HFS/bottom area, the probes measure negative U_{fl}, means they are effectively deeper in the plasma, they reach the confinement area.

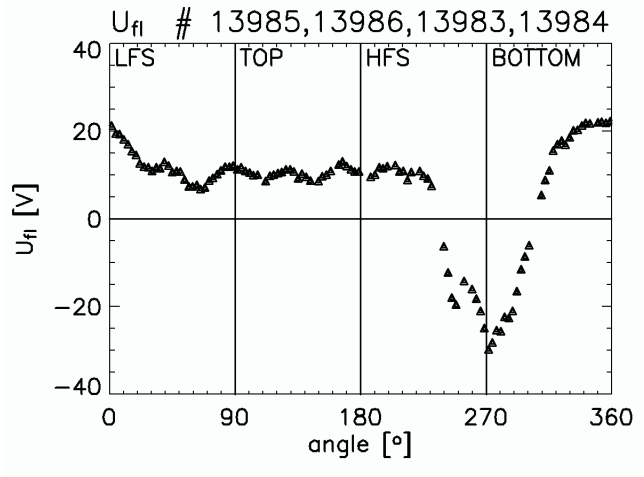

Figure 4.10: *Poloidal distribution of the radial potential [28].*

The same phenomenon can be deduced from the poloidal distribution of the sign of the poloidal velocity due to the $E_{rad} \times B_{tor}$ drift, shown in figure 4.11. The poloidal velocity

$$\vec{v}_{pol} = \frac{\vec{E}_{rad} \times \vec{B}_{tor}}{B_{tor}^2} \tag{4.12}$$

is obtained from the poloidal ring of Langmuir probes from cross-correlations of signals of adjacent probes as will be described in chapter 7. The opposite signs of the velocity in figure 4.11 indicate that the respective probes are on different sides

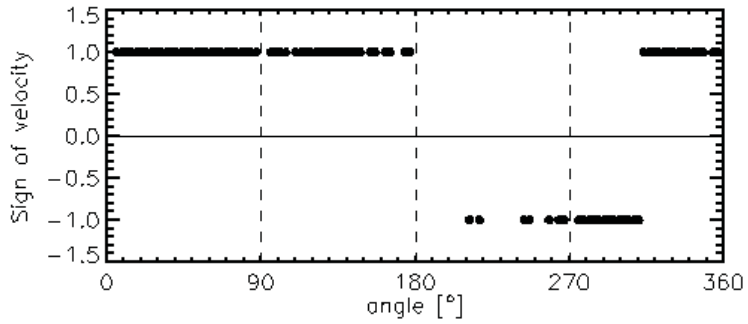

Figure 4.11: *Poloidal distribution of the sign of the poloidal velocity, #13985, 13986, 13983, 13984, [28].*

of the velocity shear layer: the positive velocity is for the probes located in the SOL with $E_{rad} > 0$ (see figure 4.9), while the negative velocity corresponds to the plasma in the core with $E_{rad} < 0$.

4.3.5 Radial profiles of temperature and density

Radial profiles of electron temperature and density obtained from the rake probe (section 3.3.1), are shown in figure 4.12. The individual tips were swept by a triangular voltage with amplitude ±100 V and frequency of 500 Hz. The electron temperature was obtained from the current voltage characteristics, density from the values of ion saturation current. In the density profile, two plateaus are observable: the first is located slightly inside the LCFS, the second one in the SOL. Although they seem to indicate areas with an enhanced radial transport, these plateaus are well below the experimental error.

The electron temperature was also measured by the standard tunnel probe (STP) (see section 3.3.2) and compared with the ion temperature. The result is in figure 4.13, top panel. The STP is oriented in the parallel direction to the magnetic field lines, thus it can measure upstream parameters (the magnetic field lines as well as the plasma current are entering into the tunnel) or downstream (the tunnel is facing the electron part of the plasma current). The upstream and downstream currents were averaged in order to obtain the radial profile of the electron and ion temperature - red and blue colour in figure 4.13 respectively. The profiles were compared to measurement of the electron temperature obtained from the rake probe – the green line in figure 4.13. The measurements show that in the SOL, the electron and ion temperatures are roughly equal.

The ion saturation current measured by the STP and the rake probe is compared in figure 4.13, bottom panel.

Another method for measurement of the radial profile of the electron and the ion temperature is by the Katsumata probe (see section 3.3.2). The result is shown

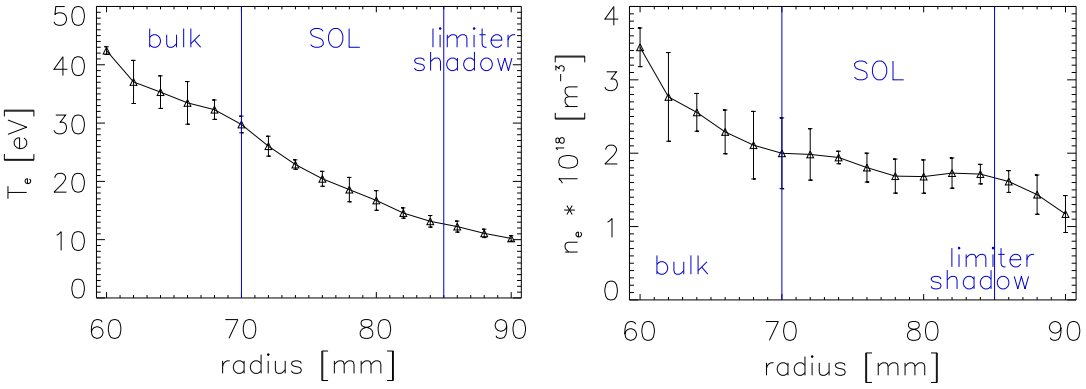

Figure 4.12: *Radial profiles of temperature (left panel) and density (right panel), #26398-26399 & #26402-26403 measured by Renaud Dejarnac in the CASTOR tokamak. The error bars show the standard deviation of fluctuations.*

in figure 4.14. It is clear that in the CASTOR tokamak $T_e \simeq T_i$ in the confinement region and in the SOL near LCFS, while in the far SOL (limiter shadow) $T_i > T_e$. This is consistent with many experimental observations summarized in [32].

4.3.6 Diffusion coefficient in the CASTOR SOL

Diffusion coefficient in the CASTOR SOL $D_\perp^{SOL}$ can be derived from formula (4.11):

$$D_\perp^{SOL} = \frac{c_S \lambda_n^2}{2L}.$$

The ion sound speed is

$$c_S = \sqrt{\frac{k_B(T_e + T_i)}{m_i}} \tag{4.13}$$

where k_B is the Boltzmann constant, T_e and T_i are given in eV, and m_i is the ion mass. $T_e \simeq T_i$ as was shown in figures 4.13 and 4.14, thus the c_S can be approximated as

$$c_S \approx \sqrt{\frac{2k_B T_e}{m_i}}. \tag{4.14}$$

A typical radial profile of c_S in the CASTOR tokamak is shown in figure 4.15.

To estimate the radial profile of the characteristic length of radial density decay λ_n according to the formula 4.5

$$\lambda_n \equiv -\left(\frac{1}{n}\frac{\mathrm{d}n}{\mathrm{d}r}\right)^{-1},$$

the density $n(r)$ has to be fitted by the exponential function (4.9) at page 39. The fit was performed in two ranges of radii as shown in figure 4.16 by the red lines: around $r \simeq 73$ mm and $r \simeq 85$ mm. The derived $\lambda_n \simeq 3$ cm (for $r \simeq 73$ mm) and $\lambda_n \simeq 1.5$ cm (for $r \simeq 85$ mm).

Finally, for the connection length L, the profile shown in figure 4.8 is used.

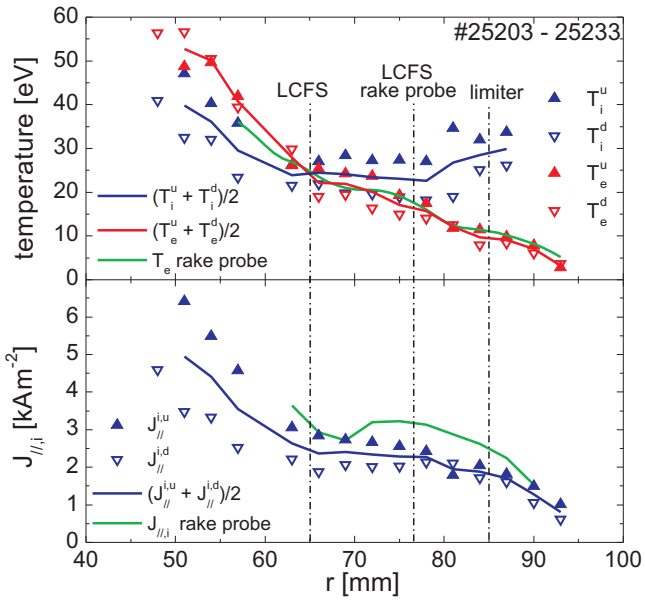

Figure 4.13: *Radial profiles of the electron and ion temperature (top panel) and the parallel ion saturation current density (bottom panel) measured by the standard tunnel probe (blue and red) compared to measurements from the rake probe (green). The figure was extracted from [29, 30].*

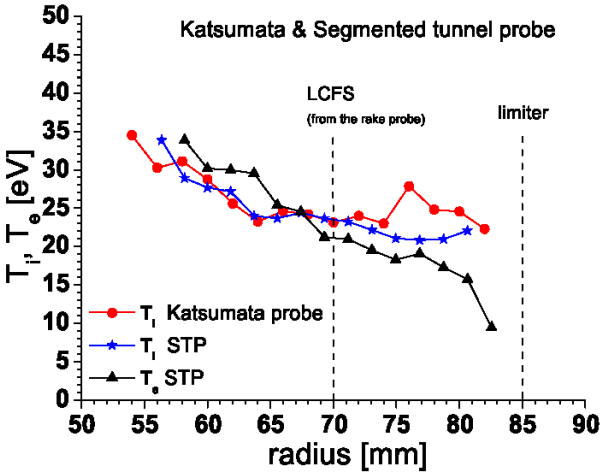

Figure 4.14: *Radial profiles of electron and ion temperature measured by Katsumata probe (red dots) and standard tunnel probe (black triangles and blue asterisks). The figure was extracted from [31].*

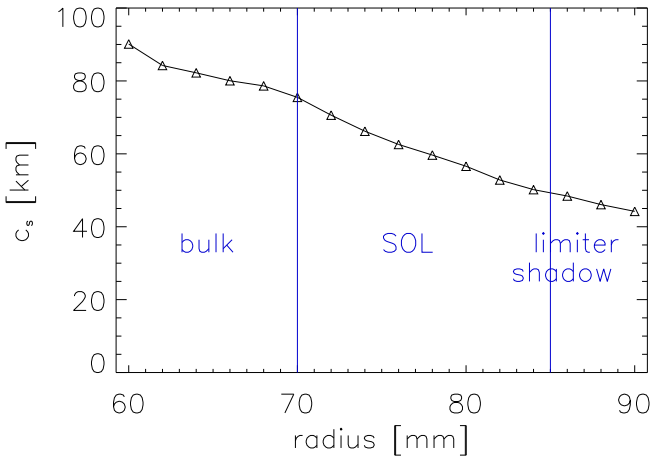

Figure 4.15: *Radial profile of the ion sound speed* c_S.

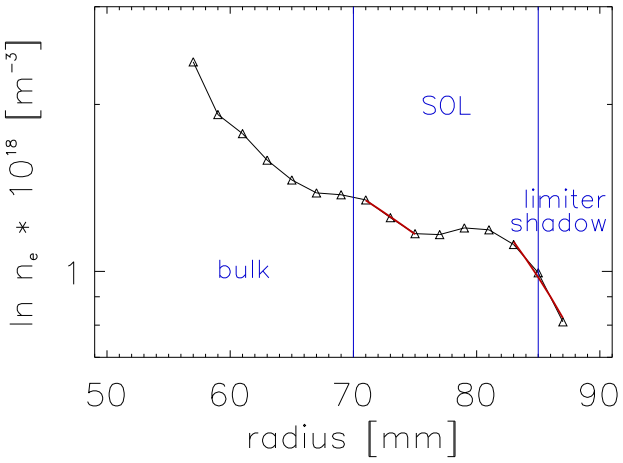

Figure 4.16: *Radial profile of the electron density in logarithmic scale with an exponential fit in the SOL area according to the formula (4.9) depicted by the red lines.*

Using these profiles, the diffusion coefficient in the CASTOR SOL $D_\perp^{SOL}$ is derived in the two above mentioned points: $D_\perp^{SOL} \sim 4\ \mathrm{m}^2/\mathrm{s}$. This value is in agreement with the diffusion coefficient calculated from the Bohm's diffusion [33] and from the Ball-pen probe measurements [33, 34]. These articles are in chapters 12 and 13.

Chapter 5

Biasing experiments

For improvement of plasma confinement, regimes with modified profiles of edge electric field are used. It is usually achieved by imposing an electric field by an electrode immersed into the edge plasma and biased at a DC voltage with respect to the vacuum vessel. This chapter describes the method, the improved plasma parameters and shows the biasing electrodes used in the CASTOR tokamak.

Ohmic discharges do not enable to achieve regimes with confinement sufficient for a fusion reactor. The fusion power is proportional to the particle confinement time τ_p [39], hence we need to increase it by the means of creating transport barriers. Biasing of the edge plasma (called simply biasing) is a way how to improve confinement not only in tokamaks, but also in other types of fusion devices such as stellarators. It is used in small-size machines since inserting an electrode into the edge plasma of large facilities is not wise: it would not survive due to high temperatures and long durations of the discharges. Biasing experiments enable us to study the influence of the velocity shear caused by radial electric field imposed into the edge plasma to the structure of turbulences in this region and consequently the influence of the shear to the plasma confinement. These experiments are of high importance for the CASTOR tokamak since a significant part of the research programme is based on them.

Typical arrangement of the biasing experiments is shown in figure 5.1. The biasing electrode is immersed from the top of the chamber into the confinement region to the radial position up to 40 mm of the minor radius, and biased at positive voltage up to +300 V with respect to the limiter. An electric field arises between the layer at the radial position of the electrode and the LCFS, which is connected with limiter. This electric field in combination with the strong toroidal magnetic field creates $E_{rad} \times B_{tor}$ drift which rotates the plasma. A transport barrier is established as will be shown in following sections. Negative biasing does not have a significant influence on plasma since the current driven by the electrode is too small ($\sim$ 5 A) to modify the edge plasma [35].

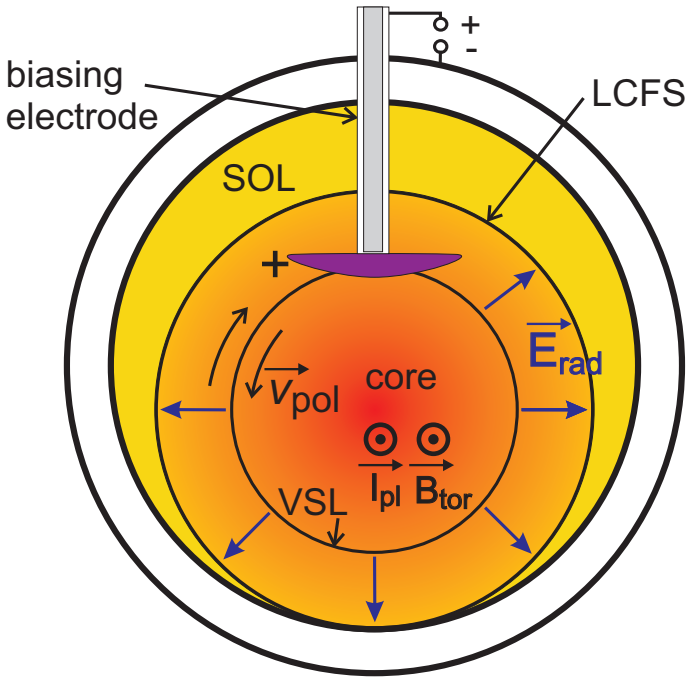

Figure 5.1: *Position of the biasing electrode, poloidal cross-section. White ring depicts the limiter. Toroidal magnetic field as well as plasma current are perpendicular to the plane of the picture.*

Biasing electrodes at the CASTOR tokamak

- Massive biasing electrode (standard biasing electrode)

  A commonly used electrode is a massive graphite mushroom-shaped electrode, shown in figure 5.2. It is radially thick 0.5 cm in the broadest place, 5 cm long in the poloidal extent and 3 cm in the toroidal one which determines its surface to be 15 cm^2. A positive voltage of $100-300$ V is applied between the electrode and the tokamak vessel and the current $-(10-30)$ A is driven.

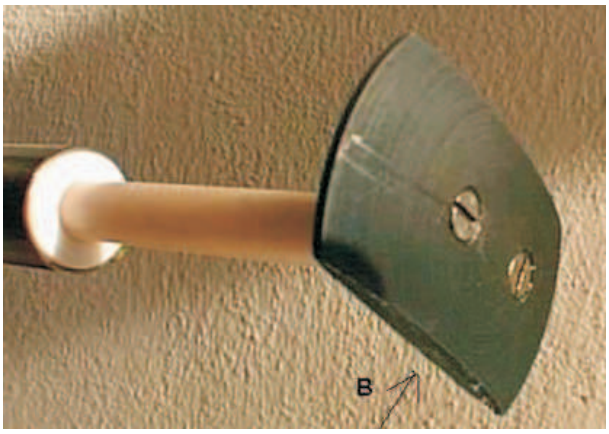

Figure 5.2: *Massive biasing electrode.*

- Segmented biasing electrode

  The segmented biasing electrode consists of five metal rings with diameter of 16 mm and thickness of 1 mm, radially spaced by 3 mm on a PTFE support as shown in figure 5.3. Each of the rings can be biased separately with respect to the vacuum vessel or can be left floating or grounded to the vessel. This electrode was used in the first experimental campaign when the relaxation events were observed (chapter 9).

Figure 5.3: *Segmented biasing electrode.*

5.1 Improvement of the global plasma parameters

During the biasing phase of the discharge, global plasma parameters change. An example is in figure 5.4. The temporal evolution of the line averaged electron density n_e is plotted, showing a clear increase after the beginning of the biasing phase. During the whole discharge, there is a continuous inflow of the working gas into the chamber which covers the particle loses during the discharge. As the transport barrier raises during the biasing phase and these loses are reduced, the averaged density increases. After the end of biasing phase, a significant amount of plasma is expelled to the walls, and the n_e returns to its original values.

Under favourable conditions (the amount of impurities is low, the imposed electric field is high), we can observe a decrease of the H_α line intensity (further simply H_α) which is perceptible shown in figure 5.4. H_α is proportional to recycling of

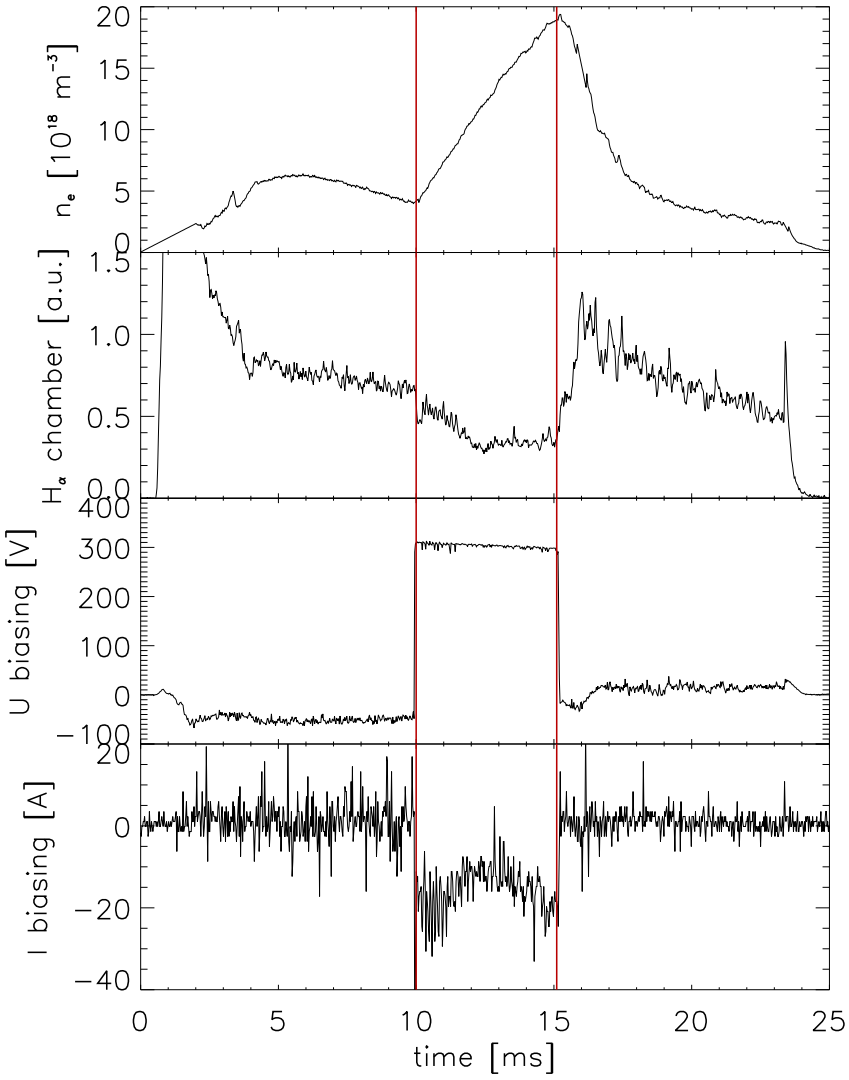

Figure 5.4: *Temporal evolution of main plasma parameters during discharge #23999 with the biasing phase between* $10 - 15$ ms. *From top to bottom: averaged plasma density* n_e*, intensity of the* H_α *line emission, voltage and current carried by the biasing electrode.*

neutral hydrogen atoms knocked from the inner wall of the vacuum vessel. The decrease of H_α is another sign of improvement of global confinement. The bottom panels in figure 5.4 show the voltage applied to the biasing electrode with respect to the limiter (third panel) and the current driven by the electrode (bottom panel).

The increase of global particle confinement during the biasing phase of discharge can be deduced from the temporal evolution of H_α and the line averaged density as [35]

$$\frac{\tau_p^B}{\tau_p^{OH}} = \frac{\bar{n}_e^B}{\bar{n}_e^{OH}} \cdot \frac{I_{H_\alpha}^{OH}}{I_{H_\alpha}^B} \tag{5.1}$$

where τ_p^B and τ_p^{OH} is the particle confinement time during the biasing and the ohmic phase, $\bar{n}_e^B$ and $\bar{n}_e^{OH}$ is the line averaged density during biasing and ohmic phase, and $I_{H_\alpha}^B$ and $I_{H_\alpha}^{OH}$ is the intensity of emission of H_α during the biasing and the ohmic phase. The temporal evolution of the ratio $\frac{\tau_p^B}{\tau_p^{OH}}$ for the same discharge as in figure 5.4 is plotted in figure 5.5. It is worth emphasizing that the particle confinement time in some cases increases by the factor of 8. It is a high value in comparison with spontaneous L-H transitions in large tokamaks with X-point divertors, where the ratio $\frac{\tau_p^B}{\tau_p^{OH}}$ raises typically only twice.

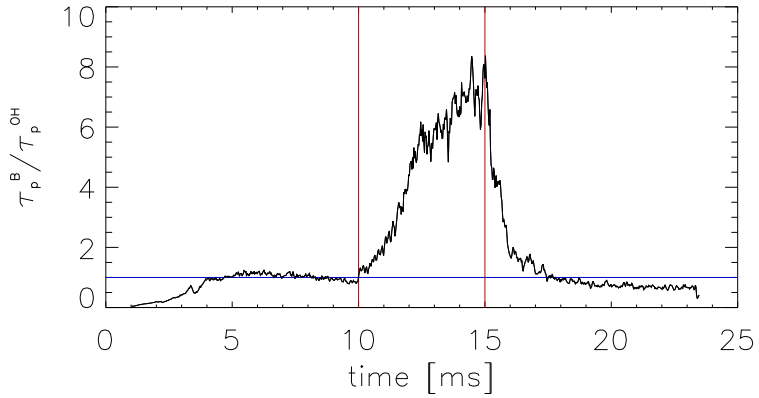

Figure 5.5: *Temporal evolution of the ratio τ_p^B/τ_p^{OH}, shot #23999. The vertical red lines indicate the beginning and the end of the biasing phase, the horizontal blue line depicts the ratio $\tau_p^B/\tau_p^{OH} = 1$.*

5.2 Radial profiles of U_{fl} and E_{rad} at the plasma edge during biasing experiments

During ohmic discharges, the radial profile of the floating potential U_{fl} reaches its maximum near the LCFS [36] and then drops down to negative values towards the plasma centre as shown in figure 5.6, left panel. The E_{rad} (plotted in the right panel) reverses its sign, this level is known as the Velocity Shear Layer (VSL).

When the biasing is on, the radial profile of U_{fl} changes from a hollow profile to a profile of a mesa (table). The maximum of U_{fl} is shifted to the position of the electrode. The value of U_{fl} dramatically increases and a strong radial electric field

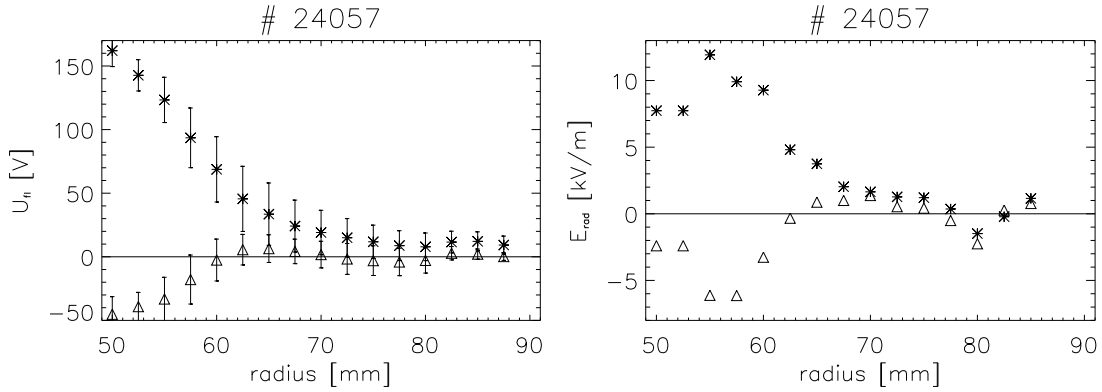

Figure 5.6: *Radial profile of U_{fl} (left panel) and E_{rad} (right panel): during ohmic regime (triangles) and during biasing of the edge plasma (stars). The biasing electrode is at the radial position of 40 mm.*

is created as shown in figure 5.6. This radial electric field drives a strong poloidal rotation due to $E_{rad} \times B_{tor}$ drift as depicted in figure 5.1. The poloidal motion shears turbulent structures in the edge plasma and the transport barrier is established.

The transport barrier established by the imposed electric field in the edge plasma decreases the energy and particle loses. This effect is observable in a radial profile of the ion saturation current I_{sat} (which is proportional to the electron density) shown in figure 5.7. During the biasing phase of the discharge, the I_{sat} rises in the inner part of the plasma, indicating an improvement of particle confinement.

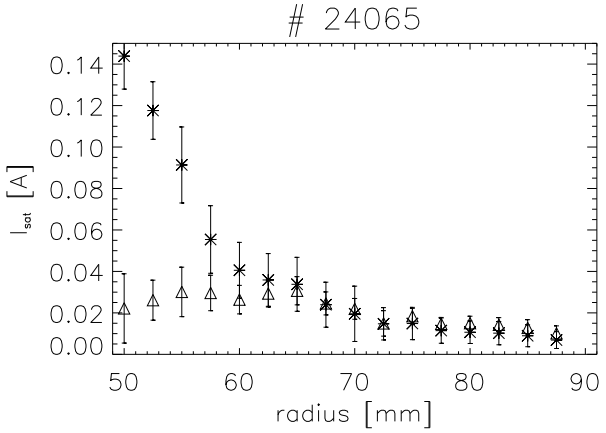

Figure 5.7: *Radial profile of I_{sat}: during ohmic regime (triangles) and during biasing of the edge plasma (asterisks). The biasing electrode is at the radial position of 40 mm.*

Chapter 6

Statistical tools

This chapter gives a brief summary of the statistical methods used for evaluation of CASTOR edge plasma turbulences and describes the ways of calculating them.

Plasma turbulence in the CASTOR tokamak is measured mainly by means of Langmiur probes. The signal contains a high level of noise, which needs to be filtered out. For this purpose, using of sophisticated statistic methods is necessary. The data are processed in the IDL programming language (Interactive Data Language).

In this thesis, mostly the turbulence of the floating potential and ion saturation current is investigated. The turbulence part of the signal is obtained by subtracting of the smoothed signal (usually smoothing is done over $600 - 1000$ μs). Using one Langmuir probe only, several types of important information about the plasma turbulence can be investigated: the moments, auto-correlation functions and power spectra. Using arrays of probes, radial and poloidal profiles of these parameters can be obtained. Moreover, space-resolved parameters can be obtained, like the cross-correlation functions, cross-power spectra, coherence, and phase-spectra.

6.1 Single point methods

6.1.1 Probability distribution function

Probability distribution function (PDF) of a random variable x is defined as

$$P(x) = \int_{-\infty}^{x} p(t)dt, \tag{6.1}$$

and we express the *density of probability* as

$$p(x) = \frac{dP(x)}{dx}. \tag{6.2}$$

The *moments* of the probability distribution function are defined as

$$\begin{aligned} M_1 &= E[x] = \int_{-\infty}^{\infty} p(x)x dx \\ M_n &= E[(x - M_1)^n] = \int_{-\infty}^{\infty} p(x)(x - M_1)^n dx \quad \text{for} \quad n > 1, \end{aligned} \tag{6.3}$$

n is so-called order of the respective moment. For our analysis, the most important moments are the first four: *mean value* μ ($n = 1$), *variance* σ^2 ($n = 2$), *skewness* S ($n = 3$) and *kurtosis* K ($n = 4$)[1]:

$$\mu = E[x(t)] \tag{6.4}$$

$$\sigma^2 = E[(x(t) - \mu)^2] \tag{6.5}$$

$$S = \frac{1}{\sigma^3} E[(x(t) - \mu)^3] \tag{6.6}$$

$$K = \frac{1}{\sigma^4} E[(x(t) - \mu)^4] - 3. \tag{6.7}$$

Variance (it's square root is the *standard deviation*) indicates the variability of the distribution. Skewness shows the dominating part of the data: the negative value

[1]For kurtosis, the definition is modified according to (6.7).

of skewness indicates that the left tail of respective PDF is longer that the right one. The skewness for a normal distribution is equal to zero. Kurtosis indicates how "peaked" the distribution is. In order to have kurtosis of a normal distribution equal to zero, -3 is added in the definition (6.7). Thus, "peaked" distributions have positive kurtosis while "flat" ones have negative values of kurtosis.

The IDL language uses the function MOMENT where the moments are defined as:

$$\mu = \bar{x} = \frac{1}{N}\sum_{j=0}^{N-1} x_j \tag{6.8}$$

$$\sigma^2 = \frac{1}{N-1}\sum_{j=0}^{N-1}(x_j - \bar{x})^2 \tag{6.9}$$

$$S = \frac{1}{N}\sum_{j=0}^{N-1}\left(\frac{x_j - \bar{x}}{\sqrt{\sigma^2}}\right)^3 \tag{6.10}$$

$$K = \frac{1}{N}\sum_{j=0}^{N-1}\left(\frac{x_j - \bar{x}}{\sqrt{\sigma^2}}\right)^4 - 3 \tag{6.11}$$

where N is the number of elements of the data vector $x \equiv (x_0, x_1, ..., x_N)$.

6.1.2 Auto-correlation

Auto-correlation function is the second moment of the PDF of $x(t)$:

$$R(\tau) = E[x(t)x(t-\tau)]. \tag{6.12}$$

This function describes the agreements of the signal $x(t)$ with itself shifted by a *time lag* τ. When we subtract the mean value from the analysed signal, we obtain the *auto-covariance function*

$$C(\tau) = E[(x(t) - \mu)(x(t-\tau) - \mu)]. \tag{6.13}$$

Thus, we can write $C(\tau) = R(\tau) - \mu^2$.

The auto-covariance function is used in a normalized form

$$\rho(\tau) = \frac{C(\tau)}{C(0)} \tag{6.14}$$

termed as the *auto-correlation coefficient*. This function takes values from -1 (anti-correlation) to $+1$ (perfect correlation) and is often mentioned simply as *auto-correlation* in the literature, which is also the case of this thesis.

The IDL language uses a function A-CORRELATE

$$\rho(Lag) = \rho(-Lag) = \frac{\sum_{k=0}^{N-Lag-1}(x_k - \bar{x})(x_{k+l} - \bar{x})}{\sum_{k=0}^{N-1}(x_k - \bar{x})^2} \tag{6.15}$$

where Lag is the time lag τ.

6.1.3 Power spectrum

The *power spectrum* is defined as the Fourier transform of the auto-correlation function

$$S(f) = \int_{-\infty}^{+\infty} R(\tau) e^{-2\pi i f \tau} d\tau. \tag{6.16}$$

If $x(t)$ is real, the $S(f)$ as well as $\rho(t)$ are real even functions. $S(f)$ shows how the mean square of $x(t)$ is distributed over frequencies. The power spectrum of the fluctuating part of the signal indicates the type of turbulence (*e.g.*, diffusion behaviour if the power spectrum as a function of frequency shows an exponential decay) and can also reveal a dominant frequency caused by a physical phenomenon or by a parasitic signal. An example of power spectra from the RFX-mod reversed field pinch and from the CASTOR tokamak are shown in figure 14.4 in section 14.3 and in figure 2 in the article in chapter 12.

For the numerical evaluation, the experiment should be repeated M times. Since this is not possible for us, we realize it by dividing the signal $x(t)$ into M slices $x_T^{(k)}$ with length T ($k = 1...M$). Then, the power spectrum estimator will be

$$S_n = \frac{1}{M} \sum_{k=1}^{M} |X_n^{(k)}|^2 \tag{6.17}$$

where $X_n^{(k)}$ is the n-th element of the discrete Fourier transform of the slice k.

6.2 Double point methods

6.2.1 Cross-correlation

The *cross-correlation function* is defined in a similar way as in (6.12)

$$R_{xy}(\tau) = E[x(t)y(t-\tau)]. \tag{6.18}$$

It shows an agreement between two different signals as a function of the time lag.

Further, *cross-coherence* is defined as

$$C_{xy}(\tau) = E[(x(t) - \mu_x)(y(t-\tau) - \mu_y)], \tag{6.19}$$

so that R_{xy} and C_{xy} are related as $C_{xy}(\tau) = R_{xy}(\tau) - \mu_x \mu_y$. The *cross-correlation coefficient* is defined as follows:

$$\rho_{xy}(\tau) = \frac{C_{xy}(\tau)}{\sqrt{(C_{xx}(0) C_{yy}(0))}}. \tag{6.20}$$

This cross-correlation coefficient is also called simply the *cross-correlation*. An example of cross-correlation is shown in figure 7.2 in section 7.3.

The IDL language uses the function C-CORRELATE for evaluation of the cross-correlation:

$$\rho_{xy}(Lag) = \frac{\sum_{k=0}^{N-|Lag|-1}(x_{k+|Lag|} - \bar{x})(y_k - \bar{y})}{\sqrt{\left[\sum_{k=0}^{N-1}(x_k - \bar{x})^2\right]\left[\sum_{k=0}^{N-1}(y_k - \bar{y})^2\right]}} \quad \text{for} \quad Lag < 0 \tag{6.21}$$

$$\rho_{xy}(Lag) = \frac{\sum_{k=0}^{N-Lag-1}(x_{k+Lag} - \bar{x})(y_k - \bar{y})}{\sqrt{\left[\sum_{k=0}^{N-1}(x_k - \bar{x})^2\right]\left[\sum_{k=0}^{N-1}(y_k - \bar{y})^2\right]}} \quad \text{for} \quad Lag \geq 1$$

Here the symbols have the same meaning as in (6.15) at page 55.

6.2.2 Cross-power spectrum, coherence, phase spectrum

In a similar way as the power spectrum (6.16), we can define the *cross-power spectrum* as the Fourier transform of the cross-correlation function (6.18):

$$S_{xy}(f) = \int_{-\infty}^{\infty} R_{xy}(\tau) e^{-2\pi i f \tau} d\tau. \tag{6.22}$$

If $x(t)$ and $y(t)$ are real then

$$S_{xy}(-f) = S_{xy}^*(f), \tag{6.23}$$

thus the part of the spectrum at positive frequencies is sufficient for determination of $S_{xy}(f)$ similarly as in the case of the power spectrum.

The cross-power spectrum is a complex function. Thus, it can be written as

$$S_{xy}(f) = C_{xy}(f) + iQ_{xy}(f) \tag{6.24}$$

where $C_{xy}(f)$ is termed as the *co-spectrum* and Q_{xy} as the *quad-spectrum*. Using the polar representation, the cross-power spectrum can be re-written as

$$S_{xy}(f) = |S_{xy}(f)| e^{i\Theta_{xy}(f)}. \tag{6.25}$$

Normalized amplitude of the cross-power spectrum is defined as

$$\gamma_{xy}(f) = \frac{|S_{xy}(f)|}{\sqrt{S_x(f) S_y(f)}}. \tag{6.26}$$

Variable $\gamma_{xy}(f)$ is termed the *coherence spectrum* (or *coherence*) and indicates the correlation of two signals in the frequency domain. It takes values from zero to one.

The quantity $\Theta_{xy}(f)$ in equation (6.25) is termed the *phase spectrum* and it gives the averaged phase difference for each frequency in the Fourier spectrum of the signals. An example of cross-power spectrum as well as the phase spectrum is in figure 7.3 in section 7.3.

For the numerical estimation, the signals are (in similar manner as for the power spectrum) divided into M slices: $x_T^{(k)}(t)$, $y_T^{(k)}(t)$ and Fourier transformed into $X_n^{(k)}$, $Y_n^{*(k)}$. Then, the cross-power spectrum estimator is

$$S_{xy,n} = \frac{1}{M} \sum_{k=1}^{M} Y_n^{(k)} X_n^{*(k)}. \tag{6.27}$$

6.2.3 Wavenumber-frequency spectrum

In turbulent plasma, there is no clear relation between the frequency and the wavenumber. Thus, for an overall picture, it is worth to calculate the spectral density function for each couple of frequencies and wavenumber. Let us consider a function of time and space $g(x,t)$, which is stationary in both the time and the space dimensions. The second order moment of this function will be

$$E[g(x,t)g(x-\chi),t-\tau)] = R(\chi,\tau). \tag{6.28}$$

The *wavenumber-frequency spectrum* $S(k,\omega)$ is defined similarly to the power spectrum: it is the Fourier transform of the second order moment of the function $g(x,t)$, but in both space and time:

$$S(k,\omega) = \int_{-\infty}^{+\infty}\int_{-\infty}^{+\infty} R(\chi,\tau) e^{-i(\omega\tau - k\chi)} d\chi d\tau. \tag{6.29}$$

Using this method for data from two probes only brings difficulty in summing over large space extent. The phase difference between the two signals is thus used as an estimate of the wavenumber at each frequency. The signals are, as in previous case, divided into M slices: $x_T^{(j)}(t)$, $y_T^{(j)}(t)$ and Fourier transformed into $X_n^{(j)}$, $Y_n^{*(j)}$. The local wavenumber for each slice j is

$$k_n^{(j)} = \frac{\arg(Y_n^{*(j)} X_n^{(j)})}{\Delta x} \tag{6.30}$$

where the index n runs over frequencies. The two-dimensional function $S(k,\omega)$ will be then approximated by a discrete two-dimensional histogram

$$S_n^{(j)} = |Y_n^{*(j)} X_n^{(j)}| \tag{6.31}$$

which is the power at frequency n in the slice attributed to the wavenumber $k_n^{(j)}$. An example of the wavenumber-frequency spectra $S(k,\omega)$ from the RFX-mod reversed field pinch and the CASTOR tokamak are shown in figure 6.1.

Finally, the numerical estimator can be expressed as

$$\hat{S}(k,\omega) = \hat{S}(p\Delta k, 2\pi n \Delta f) = \frac{1}{M} \sum_{j=1}^{M} S_n^{(j)} I_p\left[k_n^{(j)}\right] \tag{6.32}$$

where I_p is the histogram function defined as

$$I_p\left[k_n^{(j)}\right] = \begin{cases} 1 & \text{for } \left(p-\frac{1}{2}\right)\Delta k < k_n^{(j)} < \left(p+\frac{1}{2}\right)\Delta k \\ 0 & \text{elsewhere} \end{cases} \tag{6.33}$$

and p marks the wavenumber bins.

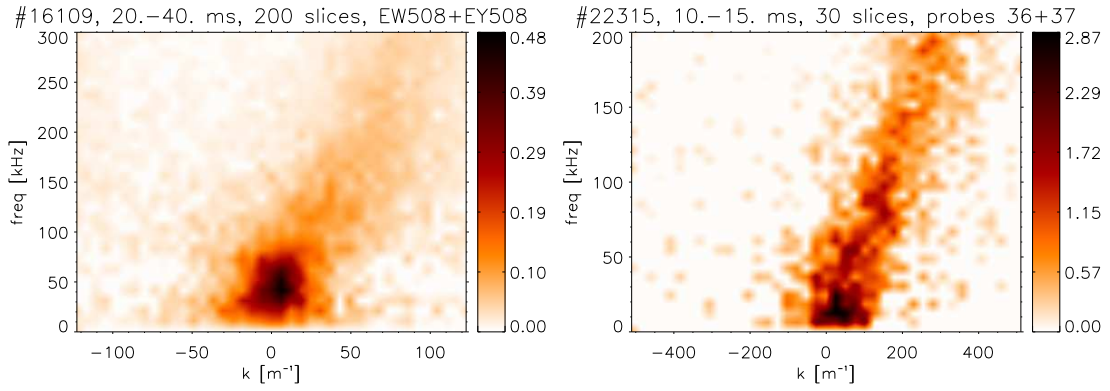

Figure 6.1: *Wavenumber-frequency spectra $S(k, \omega)$ of floating potential at the plasma edge of RFX-mod (left panel) and CASTOR (right panel). The spectra were used as reference analyses for calculating the poloidal velocity in the CASTOR tokamak in [37, 38].*

Part II

Fluctuations measurements

Chapter 7

Measurements of sheared electric fields and flows at the plasma edge of the CASTOR tokamak

Ion saturation current and floating potential are measured with high temporal and spatial resolutions at the plasma edge of the CASTOR tokamak by two poloidally spaced radial arrays of Langmuir probes. The radial electric field and the phase velocity of plasma fluctuations are determined. It is found that radial profiles of both of these quantities are strongly sheared in the proximity of the Last Closed Flux Surface. The position of the velocity shear layer is determined with a high precision. The shearing rate is determined. It was concluded that the system is in the state of marginal stability outside the VSL, while in the proximity of the VSL, the shear slightly dissipates the turbulent structures.

Poloidal velocity and radial electric field are measured at the plasma edge of the CASTOR tokamak by means of arrays of Langmuir probes. The shape of the radial profile of the floating potential results in a *shear of the radial electric field*, causing a *shear of plasma poloidal velocity* [39]. Shear of poloidal velocity is one of the mechanisms reducing turbulence at the plasma edge. It occurs naturally in magnetic fusion devices, nevertheless it needs to exceed certain limiting value to suppress the radial transport significantly. When this condition is fulfilled, the turbulent structures are dissipated and a so-called *transport barrier* arises which improves global plasma confinement.

7.1 Experimental set-up

The edge plasma parameters are measured by the double rake probe (described in section 3.3.1) which is immersed into plasma from the top of the tokamak chamber. The individual tips of the double rake probe measure either the floating potential U_{fl} or the ion saturation current I_{sat} with sampling rate of 1 μs. The radial position of the double rake probe was moved on the shot-to-shot basis to improve radial resolution. Two sets of reproducible shots were used for the following analysis: #27036 – #27045 for the U_{fl} measurements and #27046 – #27056 for the ion saturation current measurements.

7.2 Radial profiles at the plasma edge

Radial profiles of the floating potential and ion saturation current are shown in figure 7.1 [40]. The maximum of the floating potential roughly corresponds to the radial position of the LCFS [25], as explained in section 4.3.

The radial electric field E_{rad} is derived as

$$E_{rad} = -\frac{d\phi}{dr} \tag{7.1}$$

where ϕ is the plasma potential which can be calculated for hydrogen plasma in the CASTOR tokamak as

$$\phi \doteq U_{fl} + 2.5 \cdot T_e \ . \tag{7.2}$$

T_e was not measured in this experiment, instead, a typical profile from a campaign with similar plasma parameters [41, 42] was used. This profile is shown in figure 7.1 at page 43.

Radial electric field is positive in the SOL while it takes negative values inside the LCFS. This electric field, in combination with the strong toroidal magnetic field B_{tor}, causes $E_{rad} \times B_{tor}$ rotation in the poloidal direction. The poloidal rotation thus should change sign at the LCFS. Therefore, the position of the LCFS is sometimes labelled as the Velocity Shear Layer (VSL).

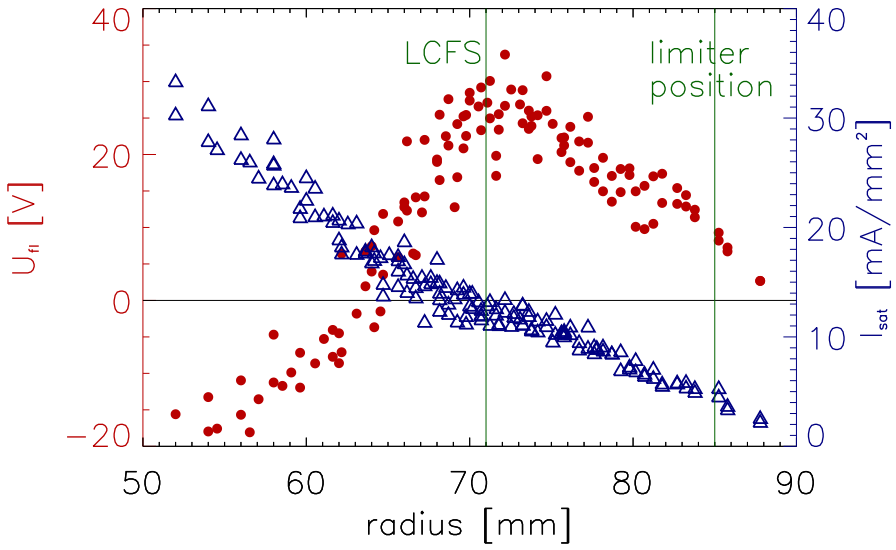

Figure 7.1: *Radial profile of the floating potential (red dots) and the ion saturation current (blue triangles). Green vertical lines show the position of the LCFS and the limiter.*

7.3 Determination of the poloidal velocity of plasma fluctuations

The plasma flow velocity is not directly measured in this experiment. Instead, we determine the poloidal phase velocity of plasma fluctuations v_{ph} by means of two poloidally spaced Langmuir probes, it means in the laboratory frame. In principal, the phase velocity of the turbulence with respect to the ambient rotating plasma may be non-zero; previous studies (summarized in [43]) show that the propagation of the turbulent structures is dominated by the $E_{rad} \times B_{tor}$ shear and thus the v_{ph} well represents the poloidal plasma velocity.

Two statistical methods are exploited in order to estimate the poloidal phase velocity v_{ph}: cross-correlation and cross-coherence techniques. The cross-correlations (see section 6.2.1) were calculated from the fluctuations of the U_{fl} or I_{sat} measured by poloidally spaced probes of the double rake probe. The sampling rate of the measured data and thus the temporal resolution of the cross-correlations is 1 μs. The poloidal phase velocity of turbulent structures v_{ph} is identified with ratio of mutual distance of poloidally adjacent probes d over the time delay of the signal appearing successively at these two probes. This delay was determined as the time lag of the maximum of the cross-correlation of two signals, lag_{max}. An example of a cross-correlation is shown in figure 7.2.

The *characteristic poloidal size of turbulent structures* in the CASTOR edge plasma λ is 1 cm [44, 45], which is higher than the poloidal distance of the probes. Thus, the maximum of the cross-correlation is rather broad and establishing of lag_{max} is not easy. Moreover, lag_{max} usually appears around 1 μs. In order to improve the resolution of this technique below the sampling period (1 μs), the cross-

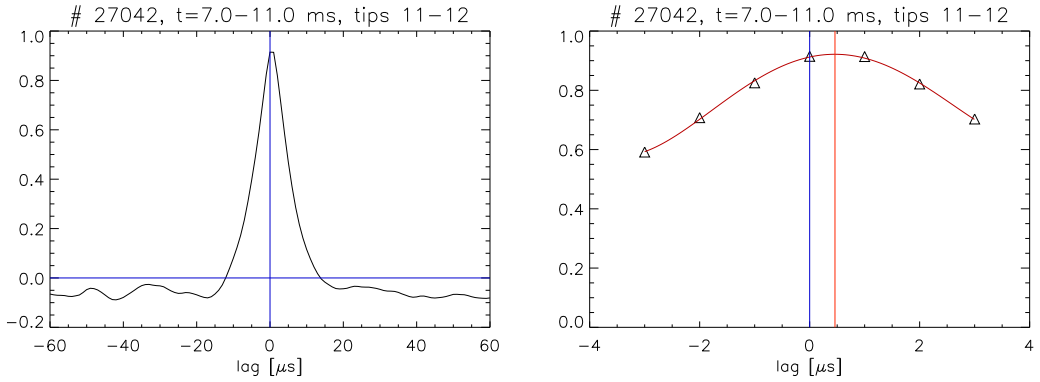

Figure 7.2: *Cross-correlation of two adjacent probes (left panel), and a detail of the function near its maximum (right panel, triangles). The red line in right panel shows a polynomial fit near* lag_{max}*. The vertical red line indicates the value of* lag_{max}*.*

correlation is fitted by a polynomial function near its maximum as shown in figure 7.2 in the right panel. As a result, the phase velocity is calculated according to a simple relation [46]

$$v_{ph} = \frac{d}{lag_{max}}. \tag{7.3}$$

Another method for evaluating the phase velocity is from the cross-coherence (described in section 6.2.2). The phase velocity is calculated from the phase of the cross-coherence as [47]:

$$v_{ph} = \frac{d \cdot 2\pi}{\frac{\Delta ph}{\Delta f}} \tag{7.4}$$

where $\frac{\Delta ph}{\Delta f}$ is the derivative of the phase with respect to the frequency. An example of a cross-coherence and its phase spectrum is shown in figure 7.3.

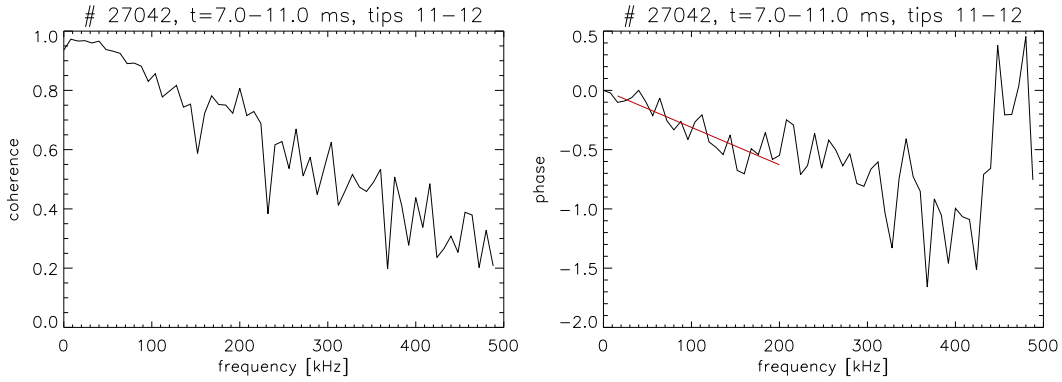

Figure 7.3: *The coherence (left panel), and the phase spectrum (right panel) of two adjacent probes. The red line on the right panel is a linear fit* $\frac{\Delta ph}{\Delta f}$ *used for evaluation of the phase velocity according to the formula (7.4).*

Both the cross-correlation and cross-coherence methods were performed for each poloidally spaced couple of tips.

7.3.1 Radial profile of the phase velocity - double rake probe

The resulting radial profiles of the poloidal phase velocity, obtained from the double rake probe, for U_{fl} (red dots) and I_{sat} (blue triangles) fluctuations are shown in figure 7.4. Both the methods (equations (7.3) and (7.4)) gave the same results, thus they are not distinguished in the figure. It can be clearly seen that the sign of v_{ph} reverses at the radius of 70.5 mm corresponding to the LCFS (see figure 7.1): In the confinement region, the poloidal phase velocity is negative, while in the SOL it takes positive values. The position of the velocity shear layer is established with a high precision in this experiment, as obvious from figure 7.4.

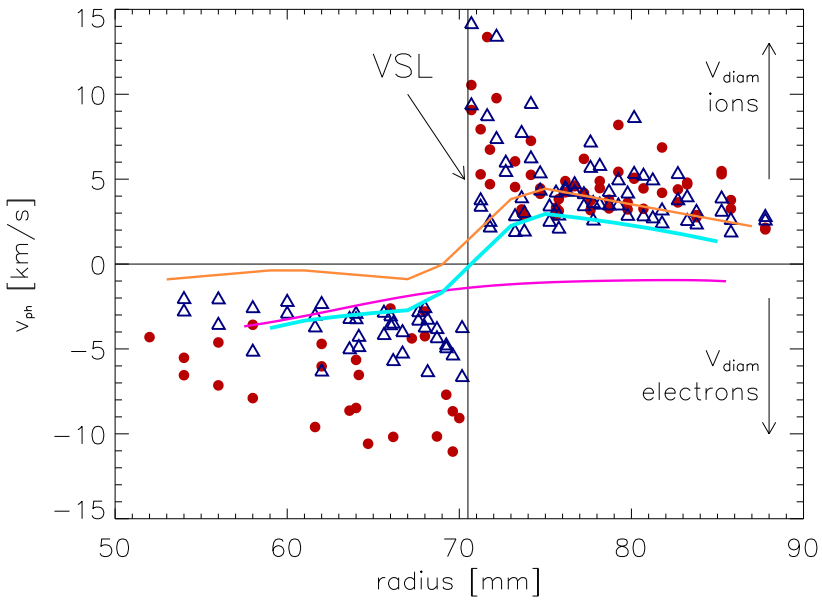

Figure 7.4: *Radial profile of the poloidal phase velocity. Red circles denote U_{fl}, blue triangles I_{sat}. Yellow line: $E_{rad} \times B_{tor}$ drift velocity (7.5), pink line: the electron part of the diamagnetic drift velocity v_{diam} (7.6), blue line: the sum of these two: $v_{E\times B} + v_{diam}$. The black vertical line depicts the VSL, the arrows indicate directions of two components of the v_{diam}.*

The values of v_{ph} were compared to $E_{rad} \times B_{tor}$ drift estimation (yellow line):

$$\vec{v}_{E\times B} = \frac{\vec{E}_{rad} \times \vec{B}_{tor}}{|\vec{B}_{tor}|^2} \doteq \frac{-\nabla(U_{fl} + 2.5 \cdot T_e)}{|\vec{B}_{tor}|} \tag{7.5}$$

according to (7.1). It is worth noting that a good agreement of the predicted velocity shear with the experimentally established one is observed when the electron part of

the *diamagnetic drift velocity*[1]

$$\vec{v}_{diam} = -\frac{\nabla p \times \vec{B}_{tor}}{q_p n_e B_{tor}^2} \tag{7.6}$$

is added to the $E_{rad} \times B_{tor}$ drift velocity (the v_{diam} is represented in figure 7.4 by the pink line, resulting $v_{E\times B} + v_{diam}$ by the sky-blue line) [48]. For this phenomenon, we have no solid explanation.

Further, the position of the VSL estimated from the $E_{rad} \times B_{tor}$ drift (the yellow line in figure 7.4) has about 1.5 mm uncertainty. This is probably caused by adding the temperature profile: i) it may slightly differ since we used a profile from a different campaign, ii) the shear of the plasma potential is not as clear as the shear of the floating potential and the numerical derivation is burdened by higher error. Figures 7.1 and 7.4 show that we for a rough estimation of the VSL, we can use the radial profile of U_{fl} instead the profile of ϕ.

In the proximity of the VSL, determination of the absolute values of the poloidal velocity using the cross-correlation and cross-coherence methods fails. The reason is omitting the radial velocity, which may cause serious over-estimation of the poloidal phase velocity as we describe in following section.

The absolute values of v_{ph} from U_{fl} and I_{sat} in figure 7.4 are similar in the SOL, which means that the potential and the density structures are linked together. In the confinement area, however, the potential velocity seems to be higher. The reason is unknown.

Model for calculation of the phase velocity over-estimation

In order to judge the error of the poloidal v_{ph} estimation introduced by the radial component of phase velocity, a simple model was developed. A turbulent structure of Gaussian shape passing over the probe was considered:

$$A = \exp\left[-\left(\frac{r}{\Delta r}\right)^2 - \left(\frac{z}{\Delta z}\right)^2\right] \tag{7.7}$$

where A is the structure amplitude and

$$r = r_i - v_r t, \qquad z = z_i - v_z t \tag{7.8}$$

are its radial and poloidal positions, r_i and z_i are the radial and poloidal positions of the probe i ($i = 1, 2$), v_r and v_z are the radial and poloidal phase velocities. It can be shown by the numerical model that the ratio of the poloidal phase velocity established by the cross-correlation method v_{ph} and the real poloidal phase velocity v_{zR} can be expressed as

$$\frac{v_{ph}}{v_{zR}} = \exp\left[\frac{v_{rR}}{v_{zR}} \cdot \frac{\Delta z}{\Delta r} \cdot \ln 2\right] \tag{7.9}$$

[1] q_p is the particle charge (in our case, for the electron component we take $q = -e$), n_e is the electron density and finally p is the plasma pressure: $p = k_B n_e T_e$. The radial electron density and temperature profiles are shown in figure 4.12 in section 4.3.5 at page 43.

where v_{rR} is the real radial phase velocity and Δr, Δz are the radial and poloidal extent of the structure.

Relation (7.9) implies that even a small contribution of the radial velocity may cause a significant over-estimation of v_{ph}. This effect is particularly visible in the proximity of the VSL where the radial velocity probably dominates the poloidal one.

In order to test the above mention hypothesis and to estimate the impact or the radial component of velocity to the calculation of the poloidal velocity, we have applied the relation (7.9) to the experimental data. The left panel of figure 7.5 shows the dependency of the measured v_{ph} on the real poloidal velocity v_{zR}. This plot shows that one value of the poloidal velocity can result in two different estimations using the cross-correlations.

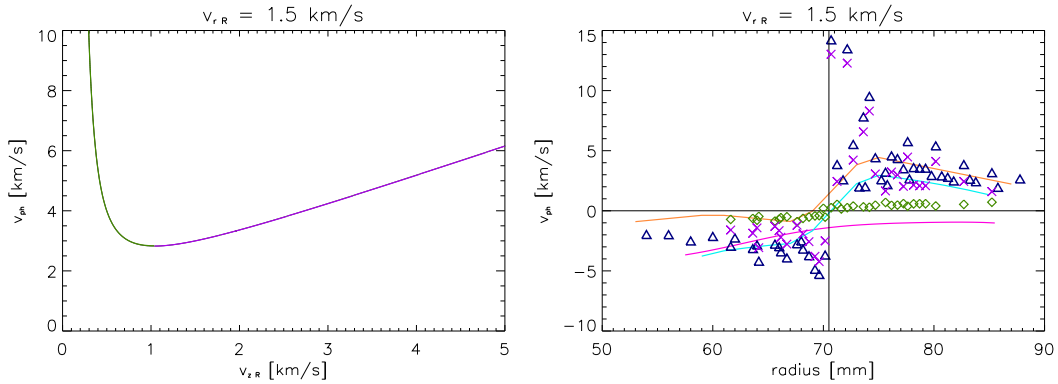

Figure 7.5: *Left: the relation (7.9): v_{ph} as a function of v_{zR}. Right panel: experimentally obtained v_{ph} from cross-correlations applied to I_{sat} data (blue triangles) compared to the correction according to the model 7.9: the violet crosses are for the high velocity branch (violet line in left panel), the green diamonds for the low one (green line in left panel).*

The real poloidal velocity v_{zR} was estimated by finding relevant values for each v_{ph} and plotted into figure 7.5, right panel. The blue triangles are the experimental v_{ph}, green diamonds show the v_{zR} estimation coming from the low velocities part of the function 7.9 (green part of the curve in figure 7.5, left panel) and the violet crosses show the v_{zR} from the high velocities part (violet part of the curve). The three curves from figure 7.4 are over plotted for illustration: yellow for the $E_{rad} \times B_{tor}$ drift velocity, pink for the electron part of the diamagnetic drift velocity, and sky-blue is the sum of these two. The radial velocity was assumed constant, the exponent $\frac{v_{rR}}{v_{zR}} \cdot \frac{\Delta z}{\Delta r}$ was considered as equal to 1.5. The velocities from ion saturation current was used, the floating potential gives similar result.

The left panel of figure 7.5 shows how the v_{ph} estimated from the cross-correlations is over-estimated. Near the VSL, the low velocity branch (green) is meaningful, while further, the experimental values as well as the estimations from the drifts agree with the high velocities branch (violet). The method has certain limitations, for example it assumes that all the structures have Gaussian shape, they are symmetric in radial and poloidal direction, and they have equal amplitudes, while in reality, they may be tilted and of a different shape (short rising time and a long tail). Nevertheless,

it is a nice illustration of limits of the method for evaluation of the phase velocity from Langmuir probe couples using cross-correlation technique.

Due to above mentioned reasons, we have a confidence in estimating the direction (sign) of the poloidal phase velocity, but the information on its absolute values is just qualitative.

7.3.2 Poloidal profile of the phase velocity - poloidal ring

In order to confirm the values of the poloidal phase velocity far from the VSL, we used experimental data measured by the poloidal ring. The tips are 5.7 mm distant, moreover, we can use every other, which gives the distance 11.4 mm.

A section laying on one magnetic surface was selected: only tips with equal values of U_{fl} were included in the further calculations. The averaged U_{fl} was 5 V, which corresponds to the radial position of 86 mm (see figure 7.1). The poloidal phase velocities were calculated and displayed in figure 7.6: the values obtained from the cross-correlations of adjacent tips (black triangles), every other tips (blue triangles) and from the cross-coherence of adjacent tips (red diamonds). The values of the poloidal phase velocity agree with the calculations from the double rake probe as well as with previous measurements [49].

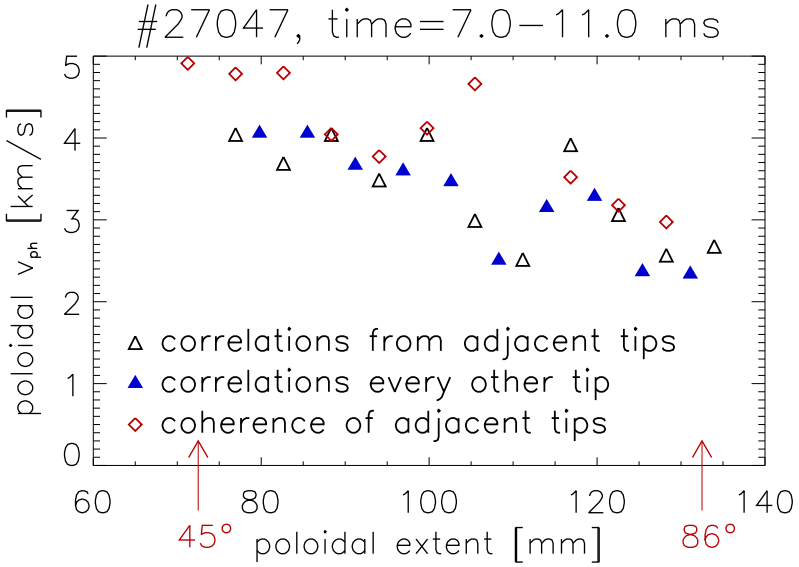

Figure 7.6: *Poloidal phase velocity obtained from the ring measurements at* $r = 86$ *mm.*

The model for calculation of v_{ph} over-estimation was applied to the poloidal ring data as well. As in the case shown in figure 7.5 in the right panel, only data from cross-correlations of U_{fl} were evaluated. The result is plotted in figure 7.7: black symbols show the velocities obtained from adjacent tips, blue are from every other. The v_{ph} estimated from the cross-correlations is depicted by triangles, the low velocities part of the function 7.9 and the crosses show the v_{zR} from the high velocities part.

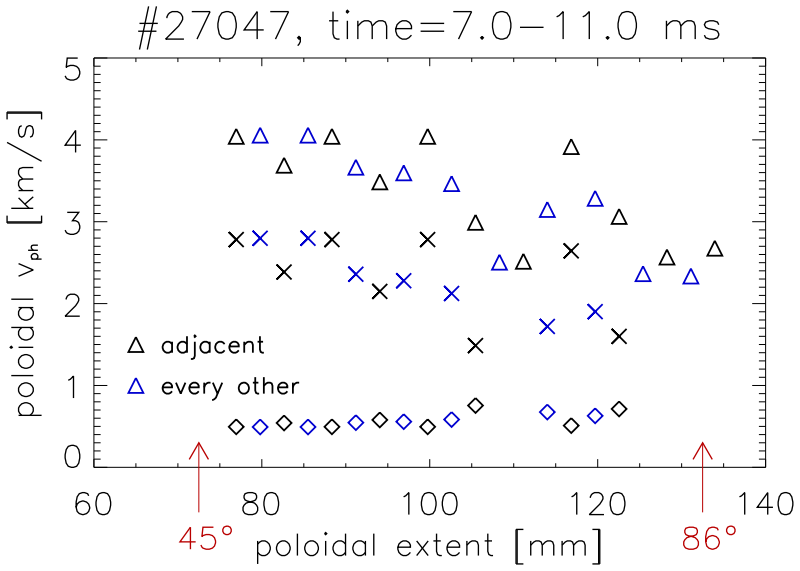

Figure 7.7: *Experimentally obtained v_{ph} from cross-correlations (triangles) of the U_{fl} data compared to the correction according to the model (7.9): the violet are for the high velocity branch, the diamonds for the low one. Black colour shows the couples of adjacent tips, blue of every other.*

7.4 Turbulent structures versus velocity shear

It is widely recognized that the velocity shear has an impact on turbulent structures [50]. In order to estimate this effect for the CASTOR tokamak, the *shearing rate* $\omega_{E\times B} = \frac{\mathrm{d}v_{pol}}{\mathrm{dr}}$ has to be compared with the inverse of the *correlation time of fluctuations* $1/\tau_{ac}$. When the shear grows too much, the turbulent structures are dissipated [51]. For a small shear, in contrary, the turbulence generates shear through tilting instability (Reynold stress) [52, 53]. Therefore, SOL turbulence remains in the state of marginal stability by the process of exchange of energy between poloidal velocity and fluctuation level.

The maximum shearing rate $\omega_{E\times B}$ in the plasma edge of CASTOR can be estimated from the $E_{rad} \times B_{tor}$ drift as a radial derivative of the poloidal plasma velocity v_{pol} (represented by the yellow line in figure 7.4, assuming $v_{pol} \simeq v_{ph}$):

$$\omega_{E\times B} = \frac{\mathrm{d}v_{pol}}{\mathrm{dr}} \leq 1 \cdot 10^6 s^{-1}. \tag{7.10}$$

The radial profile of $1/\tau_{ac}$ is shown in figure 7.8.

The natural shearing rate, as seen in figure 7.8, is comparable to $1/\tau_{ac}$ outside the VSL. In the proximity of the VSL, the shearing rate is about five times higher than the $1/\tau_{ac}$. Therefore, we can expect that the shear will dissipate the structures in this region.

Plotting the statistical properties of the edge plasma signals can check the impact of the shear on the amplitude of fluctuations. The variance of U_{fl} normalized to the T_e and the relative level of the density fluctuations ($\tilde{I}_{sat}/\bar{I}_{sat}$ where $\tilde{I}_{sat}$ is the

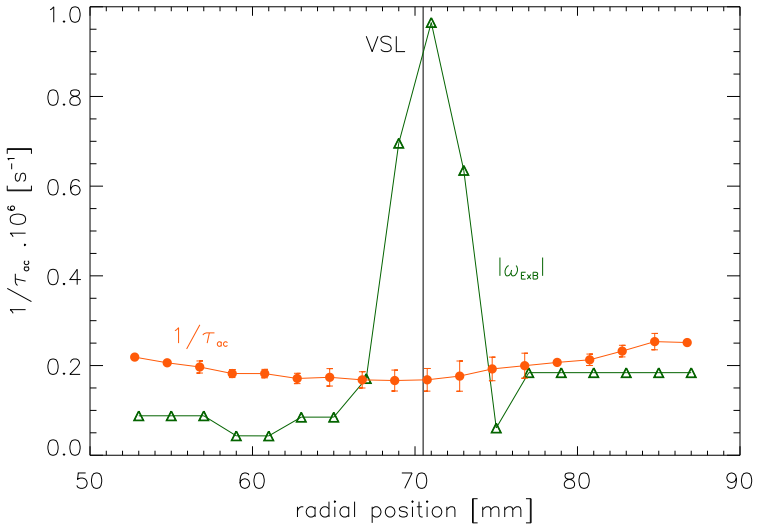

Figure 7.8: *Radial profile of* $1/\tau_{ac}$ *of the edge fluctuations (orange line, circles). The green line (triangles) shows absolute value of the shearing rate* $\omega_{E\times B}$*. The vertical black line depicts the position of the VSL.*

fluctuating part of the ion saturation current and $\bar{I}_{sat}$ is its mean value) is plotted in figure 7.9. We can observe a local minimum in the relative level of density fluctuations near the VSL, which is a sign of a disturbance of the structures. This effect is not so apparent in the potential fluctuations.

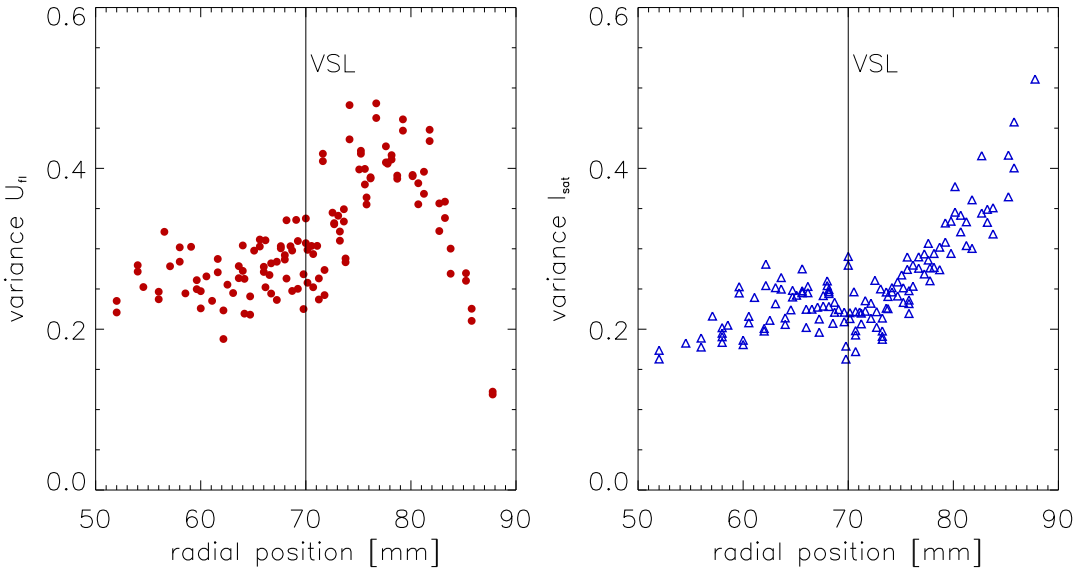

Figure 7.9: *Radial profiles of the variance of the* U_{fl} *normalized to the electron temperature (left panel) and the relative level of fluctuations* $\tilde{I}_{sat}/\bar{I}_{sat}$ *(right panel).*

7.5 Summary

Fluctuations of the ion saturation current (proportional to plasma density) and the floating potential (proportional to plasma potential) are measured at the edge of the CASTOR tokamak with high spatial resolution. The radial profile of the phase velocity is determined by two statistical methods. With high precision ($\sim$ 1 mm) we can determine the radial position of the velocity shear layer where the poloidal rotation changes the sign. A simple model was introduced to judge the error of the poloidal v_{ph} estimation introduced by its radial component. The shearing rate is estimated in the proximity of the VSL as $\omega_{E\times B} \leq 1 \cdot 10^6\ s^{-1}$. It has the same values as the inverse of the correlation time of fluctuations $1/\tau_{ac}$ outside the VSL, but it is about five times higher in the proximity of the VSL. A small reduction of the relative level of fluctuatuations at the VSL is observed in the statistical parameters of the U_{fl} and I_{sat} signals. The system is in the state of marginal stability outside the VSL, while in the proximity of the VSL, the shear slightly dissipates the turbulent structures.

Chapter 8

Investigation of the CASTOR SOL by means of 2D matrix of Langmuir probes

Two probe arrays are used to characterize the edge plasma with a high temporal and spatial resolution: the 2D probe and the rake probe. Biased flux tubes formed by imposing a voltage to the edge plasma region as well as toroidal structures occurring naturally in the ohmic plasma, are investigated in this chapter.

Control of the *parallel* and *perpendicular fluxes* in the Scrape Off Layer (SOL) is an important issue for the fusion reactor. *Plasma-wall interaction* is the main source of impurities. This interaction can be suppressed be decreasing of the radial transport in the SOL. In the divertor region, on the contrary, the radial transport needs to be high enough to spread the energy over a large area, avoiding a damage of divertor plates by focusing the plasma into hot spots. Inside the LCFS, a transport barrier is required for better plasma confinement.

An extensive experimental activity has been carried out on the CASTOR tokamak, aimed at gaining a better understanding of the SOL properties and at finding ways to control it [16, 18, 54]. Among the attempts which have been made, we can cite the creation of convective cells by means of a biasing electrode, exploiting the periodic structure of the SOL due to the local safety factor [55]. In this part, we report results on the use of electrode and probe arrays for mapping the magnetic field lines periodicity in the SOL, and for determining the geometry of edge fluctuations.

8.1 Experimental set-up

Two kinds of Langmuir probe arrays were used for measurement of the edge plasma parameters: the 2D matrix of Langmuir probes (shortly 2D probe) and the rake probe, both described in section 3.3.1. The edge electric field was in some discharges modified by the massive biasing electrode (chapter 5).

Both these probe arrays were inserted into the tokamak from the top and their radial positions could be adjusted on the shot-to-shot basis. Typically, the range of radii from 60 to 90 mm was investigated.

The experimental set-up is shown in scale in figure 8.1, which displays the toroidal and poloidal position of all key elements on an unfolded magnetic surface associated with the biasing electrode. Orientation of the 2D probe could be either parallel,

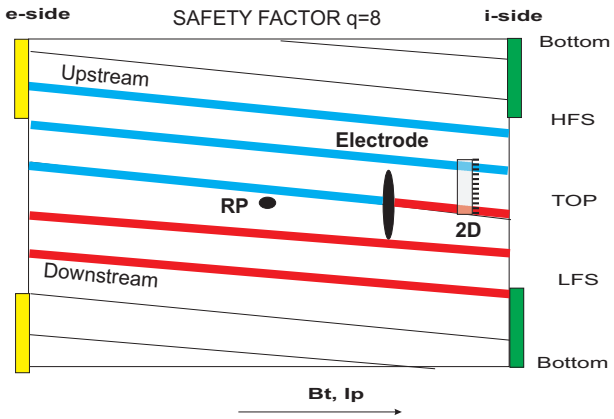

Figure 8.1: *Unfolded magnetic surface: The surface is poloidally cut along the limiter and toroidally at the bottom. Toroidal and poloidal positions of the probe arrays and of the electrode are depicted. The flux tube emanating from the electrode either upstream or downstream along the magnetic field line is emphasized by different colour. RP indicates the position of the rake probe, 2D is the 2D probe.*

or anti-parallel to the magnetic field lines (and also to the plasma current) which have the anti-clockwise direction when viewed from the top of the tokamak chamber. Thus, in the anti-parallel case, the tips of the 2D probe are oriented towards the biasing electrode while in the clockwise case they are oriented to the opposite direction. For anti-parallel orientation, the 2D probe is poloidally in the middle of the chamber while for the parallel orientation it is shifted of about 4 cm to the Low Field Side due to asymmetry of the probe holder.

8.2 Mapping of magnetic field lines in the SOL

First experiment was devoted to mapping the magnetic field lines at the plasma edge of the CASTOR tokamak. It was performed by using the biasing electrode and the 2D probe.

In order to "mark" the magnetic field lines, we have applied a harmonic voltage ($\pm$80 V) of different frequencies (1, 5 or 10 kHz – the results do not vary with frequency) to the electrode. Power spectrum was evaluated from U_{fl} fluctuations of individual 2D probe tips. The power spectra amplitude for driving frequency as a function of the radial and poloidal coordinates for the anti-parallel orientation of the 2D probe is plotted in figure 8.2, left panel.

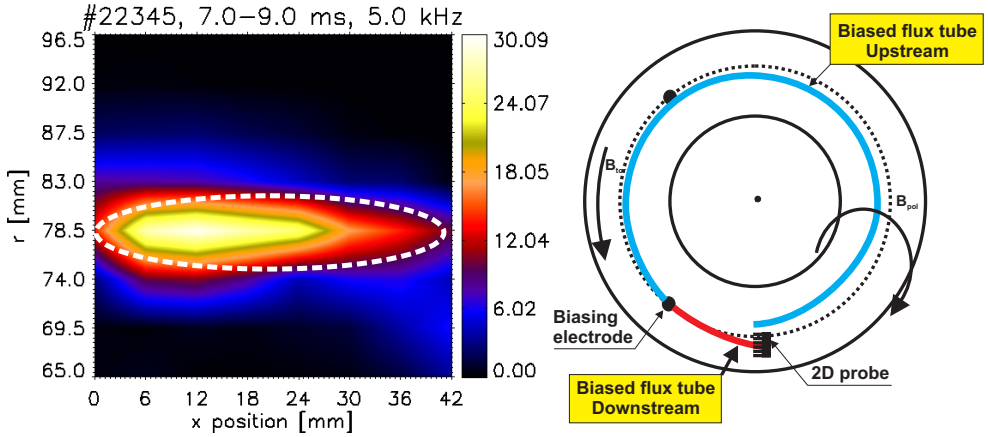

Figure 8.2: *Left: Power spectrum amplitude from the 2D probe with anti-parallel orientation, calculated for the frequency of the voltage applied to the electrode. Right: Trace of the flux tube associated with the electrode depicted in a scheme of the top-view at the tokamak vessel.*

The clear pattern observable in figure 8.2 corresponds to a projection of the biasing electrode in the 2D probe from the distance of 30 cm. The poloidal ($\sim$ 50 mm) and radial ($\sim$ 5 mm) extent of the biased flux tube can be determined. They roughly correspond to the dimensions of the electrode.

Another kind of pattern can be observed in figure 8.3 (left panel) for the 2D probe turned to the opposite side and shifted poloidally. On the right-hand side, we see just a part of the upstream flux tube. The second pattern (on the left) is a shadow of the downstream flux tube coming from back of the probe (see the right

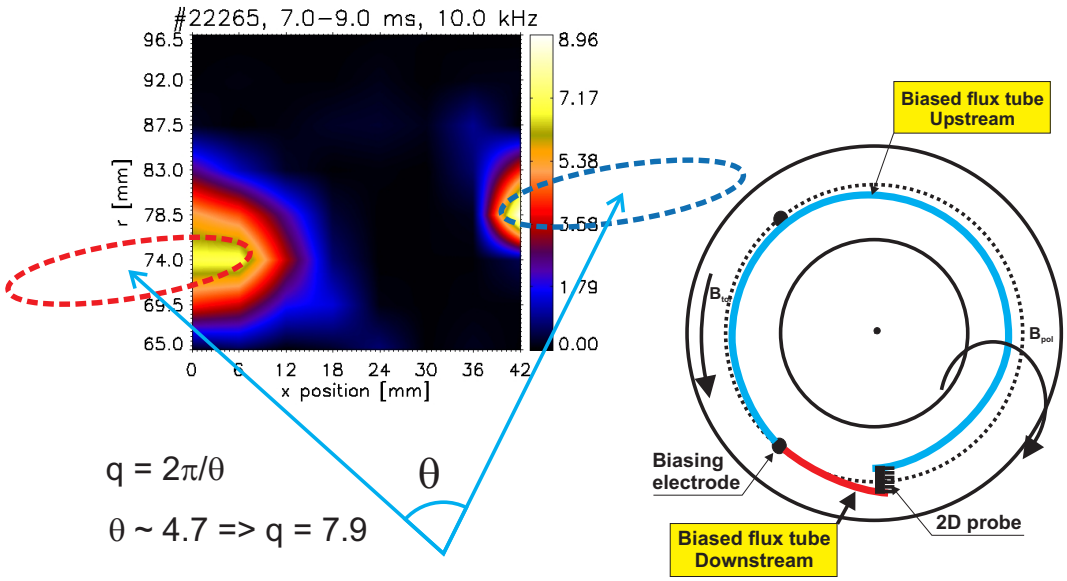

Figure 8.3: *Left: Power spectra from the 2D probe with parallel set-up. The blue arrows schematically point from the plasma column centre to the centre of the electrode projection. Right: Trace of the flux tube associated with the electrode depicted in a scheme of the top-view of the tokamak vessel.*

panel). The virtual shift of the patterns in radial direction is caused by the shift of the probe in the poloidal direction as is implied by tilting of the ellipses: the 2D probe is misaligned to the left with respect to the vertical axis of the chamber, therefore one row of tips does not lay on one magnetic surface. The length of the upstream flux tube is ~ 30 cm and of the downstream flux tube is ~ 220 cm.

The safety factor q (see section 3.2.7) can be estimated from the projections of the electrode. Considering the size of the biased flux tube as obtained from the anti-parallel lay-out (figure 8.2) and the distance between two patterns from the parallel lay-out (figure 8.3), we can find out that the angle between them is equal to about 47°. From this angle, we can estimate the edge safety factor $q = 7.9$. This value is in a good agreement with the value calculated in section 3.2.7.

8.3 Fluctuations measurements by the 2D probe and the rake probe

Once we have checked the geometry of the edge plasma, we can trace the turbulent structures using the 2D probe and the rake probe in ohmic regime. The toroidal distance between the rake probe and the 2D probe was about 1 m, the biasing electrode was retracted from the plasma. One reference tip of the rake probe was selected and its signal was confronted with all the 2D probe tips by computing the cross-correlations with the time lag = 0 ms. The result is shown in figures 8.4 and 8.5.

A pattern of a structure with high cross-correlation can be noticed in figure 8.4,

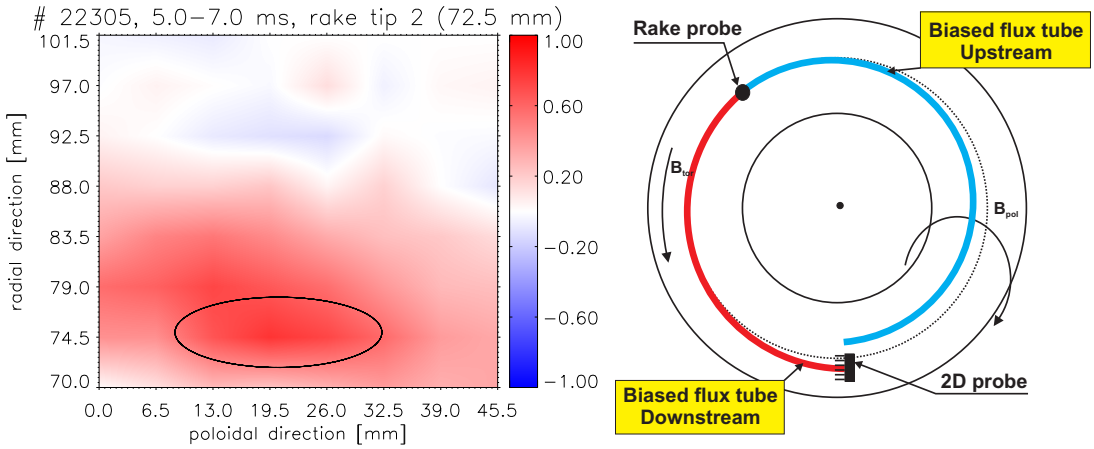

Figure 8.4: *Left: Cross-correlations with* lag $= 0$ *of the 2D probe for the anti-parallel orientation with the rake probe tip 2 (radial position 72.5 mm). The ellipse marks a "projection" of a typical turbulent structure. Right: Trace of the structure depicted in a top-view of the tokamak vessel.*

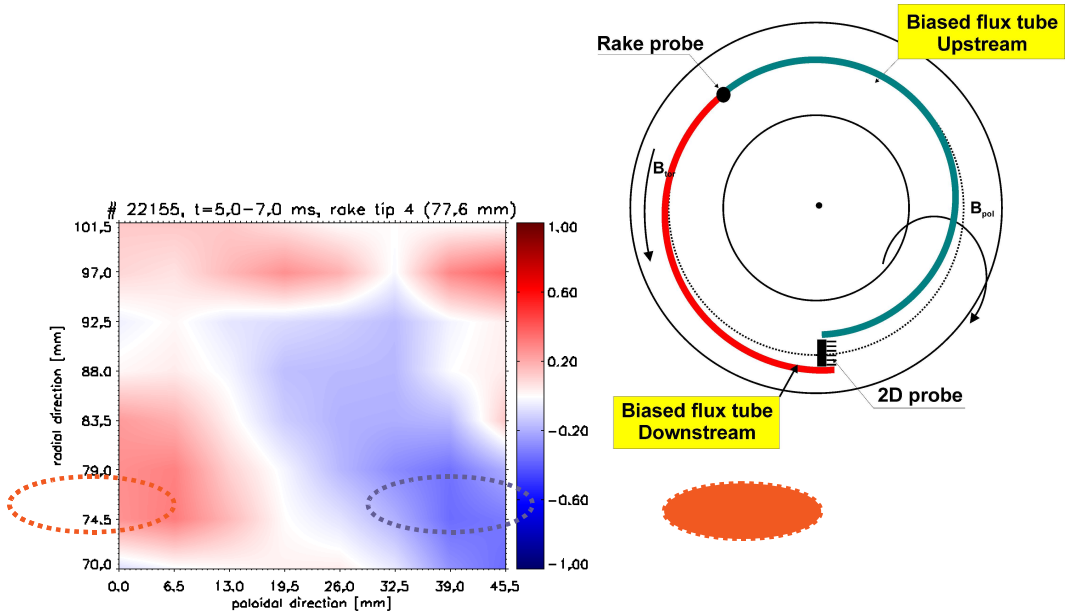

Figure 8.5: *Left: Cross-correlations with* lag $= 0$ *of the 2D probe in parallel orientation with the rake probe tip 4 (radial position 77.6 mm). The red ellipse on the left shows a "projection" of a typical turbulent structure, the blue ellipse shows an anti-correlation pattern. The filled red ellipse on the right side depicts an expected position of another maximum of cross-correlation for* $q = 8$*. Right: Trace of the structure depicted in a top-view of the tokamak vessel.*

left panel[1]. Its poloidal extent can be estimated as 2.3 cm while the radial extent is 0.6 cm. The toroidal length of this structure is longer than 1 m, as follows from the experimental arrangement. The geometry of the lay-out is shown in figure 8.4 in the right panel.

A similar pattern of a structure can be observed also in figure 8.5, left panel. A maximum of cross-correlations can be recognized in the bottom left corner of the picture. The other side of the structure is out of the range of the 2D probe but we can see an anti-correlation pattern on the right. Such a bi-polar character of the edge turbulence has been identified in CASTOR in [57]. If we mark the correlated and anti-correlated pattern as shown in figure 8.5 and compute the edge safety factor, we obtain $q = 8$, which is in good agreement with previous results.

8.4 Poloidal velocity of turbulent structures with DC biasing

Now, we return to the experimental arrangement with the biasing electrode. This time, a DC voltage of 50 V is applied. It causes a high gradient of the plasma potential and thus a strongly sheared electric field. This field creates the $E_{rad} \times B_{tor}$ drift that rotates the plasma generating convective cells [55].

Orientation of the 2D probe is anti-parallel, thus the magnetic field lines enter the plane of the picture. Floating potential of the 2D probe tips is plotted in figure 8.6 in the left panel. The pattern of the biasing electrode is well pronounced, the directions of the E_{rad} are shown by black arrows.

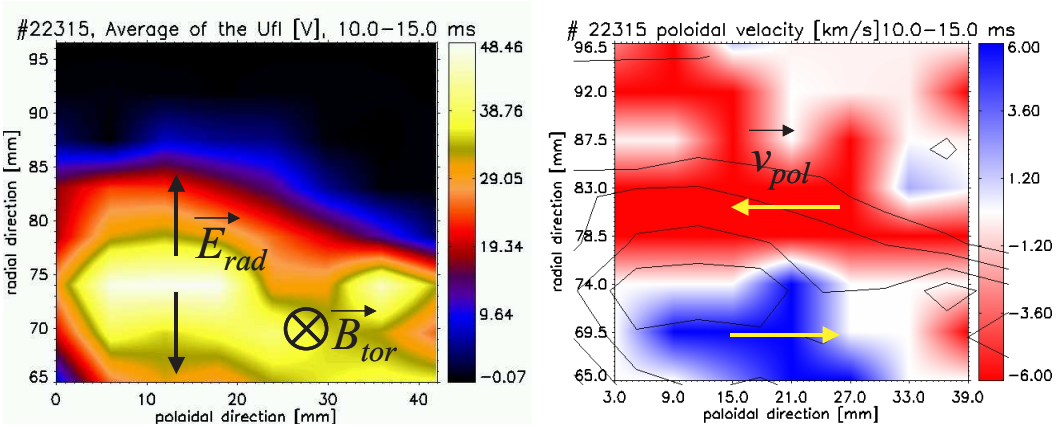

Figure 8.6: *Left: 2D plot of the floating potential. Right: 2D plot of the poloidal velocity. Red and blue colours represent two opposite directions of the velocity.*

The $E_{rad} \times B_{tor}$ drift rotates plasma in the poloidal direction. The poloidal plasma velocity is not measured directly, instead, the poloidal phase velocity of plasma fluctuations was evaluated in the same way as in chapter 7: the time lags of the maxima of the cross-correlations of adjacent tips were divided by the distance

[1]The pattern is more clear in the electronic version of the picture.

of the tips. The resulting velocities are plotted in figure 8.6 in the right panel. The red and blue colour show different directions of the plasma motion.

Values of the poloidal velocity were established as < 6 km/s. It is in a good agreement with the close study in chapter 7. The 2D probe is very large and it's disturbance to the edge plasma can not be neglected. Thus, for proper analysis, using of smaller probe arrays is more suitable.

Evaluation of the radial velocity is burdened by a high error since the poloidal component of the phase velocity significantly influences the process as we discuss in chapter 7.

8.5 Summary

Magnetic field configuration of the edge plasma region of the CASTOR tokamak was investigated by means of biasing flux tubes by imposing a harmonic voltage in the plasma. Furthermore, turbulent structures can be characterized by the cross-correlation analysis between two toroidally spaced probe arrays. This allows us to establish the radial and poloidal extent of turbulent structures in the SOL. Poloidal velocities driven by $E_{rad} \times B_{tor}$ drift were calculated. The values are ~ 6 km/s in the shear region. The results of this experiment are linked up with the previous ones [56], [57], chapter 7, where the velocities reached values $4 - 6$ km/s in the same region.

Chapter 9

Analysis of relaxation events in the CASTOR tokamak using deeply immersed biasing electrode

A strong radial electric field is generated by a biasing the plasma edge of the CASTOR tokamak. If the E_{rad} is strong enough, the edge plasma parameters relax with periodicity of about 100 μs. This phenomenon is experimentally studied by a complex system of electric and magnetic diagnostics.

Transport of plasma to the walls is one of the crucial topics in magnetic confinement fusion research. Large tokamaks operate in regimes with high confinement (*H-mode*) [39], which will be also the reference regime for the future fusion reactor (ITER). The H-mode is characterized by a steep gradient of plasma pressure at the edge responsible for creation of a transport barrier. This barrier periodically collapses and rises again, which is manifested by relaxation events termed *Edge Localized Modes* (ELMs [58]). ELMs are connected with degradation of plasma confinement and consequent release of energy and particles to the wall. Since the amount of energy and particles can be quite high, ELMs can cause a serious damage of the vacuum vessel and of divertors of large tokamaks.

Tokamak CASTOR does not operate in H-mode, which is typical for tokamaks with divertor configuration (section 4.1.2). Nevertheless, during discharges with strong biasing of plasma, we observe relaxation events which can resemble ELMs. Arrays of diagnostics with exceptionally high spatial and temporal resolution make CASTOR a unique facility to study these relaxation phenomena in detail.

9.1 Experimental set-up

Two kinds of sets-up were used for the biasing experiments: First, with the segmented electrode, and second, with the massive carbon mushroom-shaped electrode (the standard electrode). Both the electrodes (described in chapter 5) were immersed deep into the plasma from the top of the chamber, in all the presented cases at the radial position of 40 mm. A positive voltage of $100 - 300$ V was applied between the electrode and the tokamak vessel during the flat top phase of the discharge, and consequently the current $10 - 30$ A was driven.

Toroidal distribution of the diagnostics in the tokamak chamber for the experiments is depicted in figure 9.1. Radial profiles of the electric fields and I_{sat} (which is proportional to the density) are measured by the rake probe (the first campaign) and from the double rake probe (the second campaign). During the second cam-

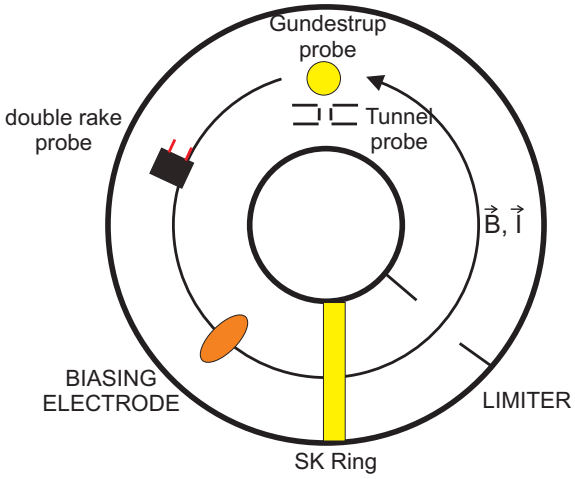

Figure 9.1: *Set-up of the experiment: top view of the tokamak vessel.*

paign, toroidal and poloidal flows are measured by the Gundestrup probe (section 3.3.2). All these probes are immersed from the top of the torus. All the data from the electric and magnetic probes are acquired with the frequency up to 1 MHz.

Moreover, poloidal profiles of the electric field, ion saturation current, and magnetic field is monitored by the SK ring[1] during the second campaign. This ring is located slightly behind the poloidal limiter ($r = 87$ mm), the poloidal distance of the tips is 5.7 mm. The Langmuir probes can measure local values of U_{fl} and I_{sat} while the coils monitor poloidal magnetic field from the plasma volume.

9.2 Relaxation events

The relaxation phenomena were first monitored in a campaign with the segmented electrode and the single rake probe. For the next campaign, appropriate diagnostics were inserted in order to obtain additional plasma characteristics. The relaxation phenomena are reproducible, though, these two campaigns showed some interesting differences.

Texture of a probe signal

When the biasing electrode is immersed deep enough into the plasma ($r/a \simeq 0.5$) and biased to high enough voltage (more than +220 V), periodic oscillations can be observed in signal of Langmuir probes.

Examples of signals from a single tip of the rake probes is shown in figure 9.2. During the biasing phase of discharge, the floating potential U_{fl} is clearly modulated with the frequency of approximately 10 kHz. After the biasing is switched off, U_{fl} drops and shows only a broadband fluctuations.

In some discharges, the relaxation events occur through the whole biasing phase of discharge (shot #29552, bottom panel of figure 9.2) while in another cases, they start later, in the middle of the biasing phase of discharge only (middle panel). Another option is shown in the bottom panel: the relaxation events were generated immediately after the triggering of the biasing and they were soon damped; in some shots, at the end of this phase, new events with longer period raised.

Radial profiles of U_{fl}

Using the whole radial column of the rake probe, we can obtain a temporal evolution of radial profile of the U_{fl}. An example is given in figure 9.3, during and after biasing. We can clearly see strong relaxations of the profiles with the characteristic frequency of about 10 kHz.

A detail of temporal evolution of floating potential is given in figure 9.4. One zoomed-in relaxation event is plotted in left panels. The red vertical lines depict three different times, characterizing the phases of development of the transport barrier; radial profiles of U_{fl} in these particular moments are plotted in the right panels. The top panels are devoted to the first campaign (segmented electrode,

[1]Poloidal ring of 96 Langmuir probes and of 16 magnetic coils, see section 3.3.1 for details.

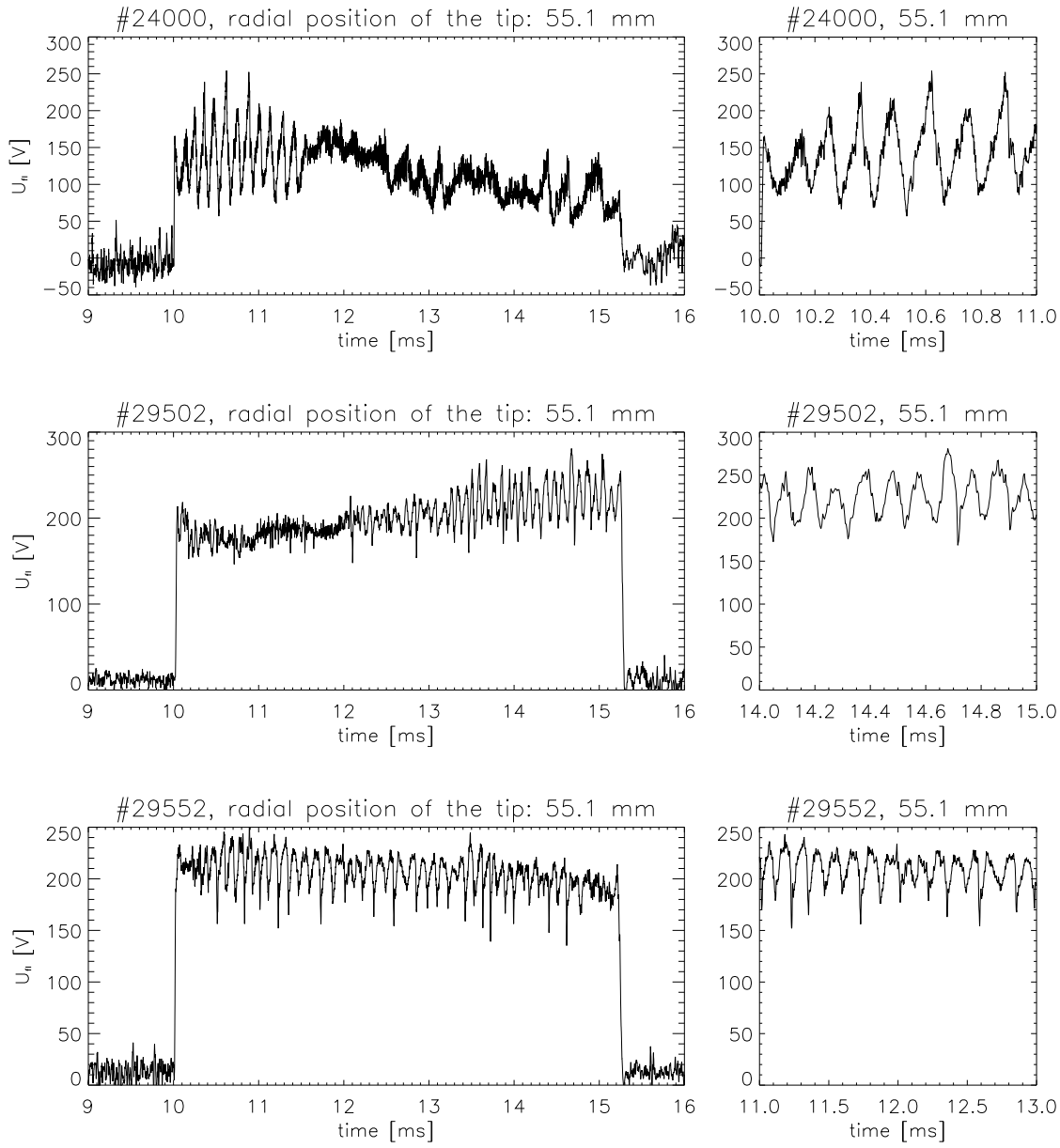

Figure 9.2: *Raw signal of tips of the rake / double rake probe. The left panels show the whole biasing phase of the discharge (10-15.2 ms); the right ones show details of the relaxation events. The top panels are from the first campaign (with the segmented electrode and the single rake probe) while the middle and bottom panels show the data from the second campaign (with the standard electrode and the double rake probe).*

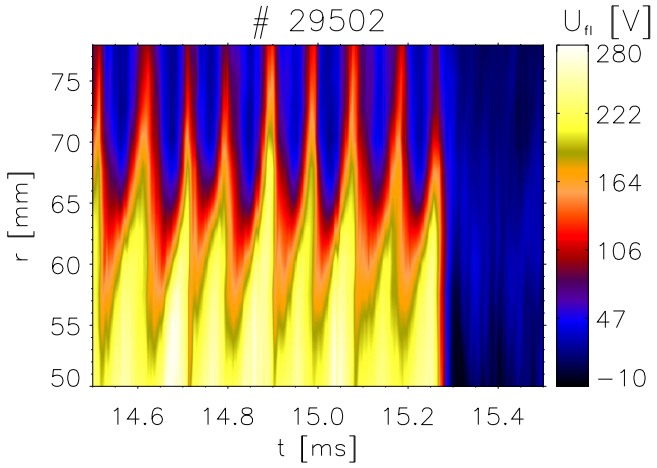

Figure 9.3: *Temporal evolution of radial profile of the floating potential during the biasing of the edge plasma, and after the biasing is switched off (15.3 ms).*

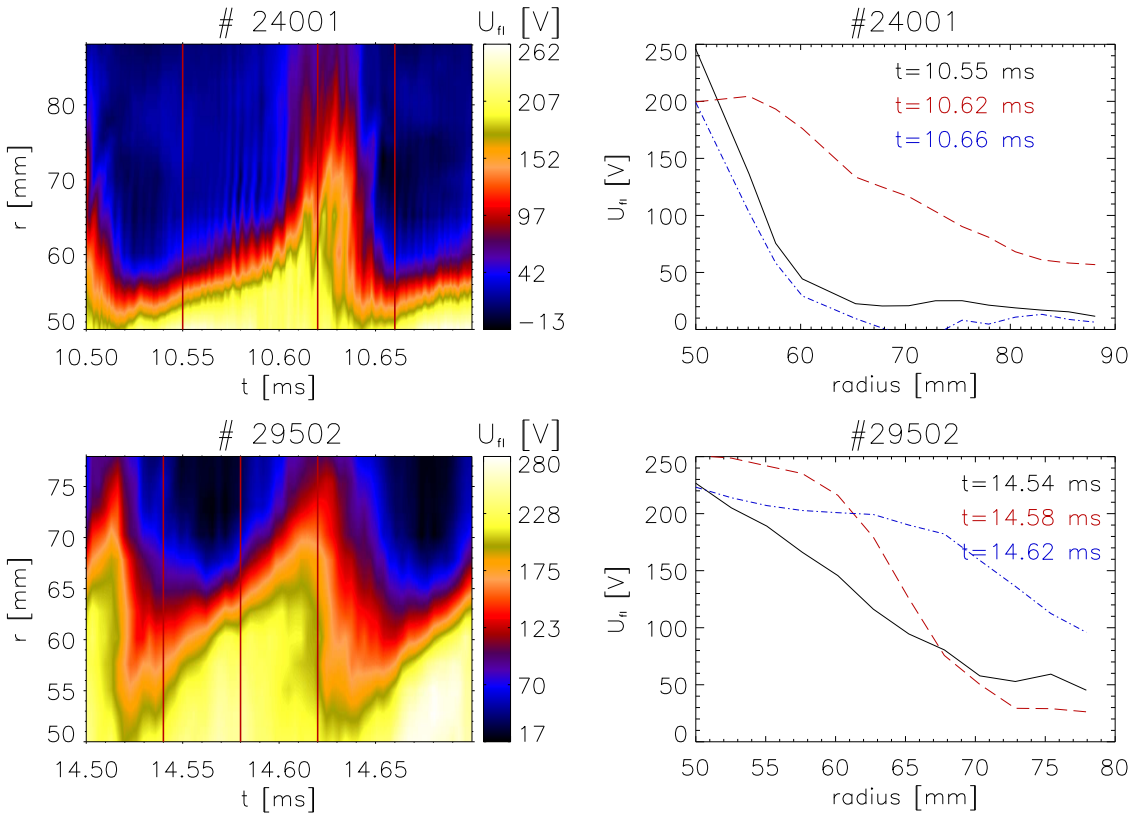

Figure 9.4: *One zoomed-in event of the relaxation of transport barrier. Left: Temporal evolution of U_{fl}. Right: Radial profiles of U_{fl} at the times depicted by the red vertical lines in the left panels. Top panels show the data from the first campaign, bottom panels from the second one. Biasing electrodes were inserted in the radial position of 40 mm.*

single rake probe) while the bottom panels show events from the second campaign (standard electrode, double rake probe).

It is interesting that the shapes of the radial profiles of floating potential of the relaxation events are slightly different: In the first campaign, the gradient of U_{fl} (E_{rad}) is formed immediately after the relaxation event and slowly travels outward ($t = 10.55$ ms). When it reaches LCFS, it suddenly collapse ($t = 10.62$ ms) to be formed again in the confinement region. On the other hand, the events from the second campaign are much broader at the beginning and the maximum of the gradient U_{fl} is established gradually. The radial movement of these events is higher.

Radial profile of E_{rad}

Radial electric field E_{rad} in combination with the strong magnetic field B_{tor} rotates plasma in poloidal direction by $E_{rad} \times B_{tor}$ drift as described in chapter 7. At positions with strong E_{rad}, we can expect a strong shear of poloidal velocities, which results in dissipating turbulent structures and hence in decreasing of transport.

In the plot of temporal evolution of radial electric field (figure 9.5), we can observe a strong transport barrier being periodically formed inside the LCFS, in the range of radii $50-60$ mm in this particular case. The barrier is formed in the confinement region (as was mentioned above) and after some time, it starts to propagate radially towards the wall with velocity up to 220 m/s. The barrier collapses, when it is approaching the LCFS, which is located at r = 69 mm as depicted by the white dashed line. Dissipating of the barrier is accompanied by fine modulation of electric field which propagate radially quite fast, with the velocity of ~ 1.5 km/s. Radial profile of the floating potential is given in the bottom panel of figure 9.5 to illustrate the connection of U_{fl} and E_{rad}.

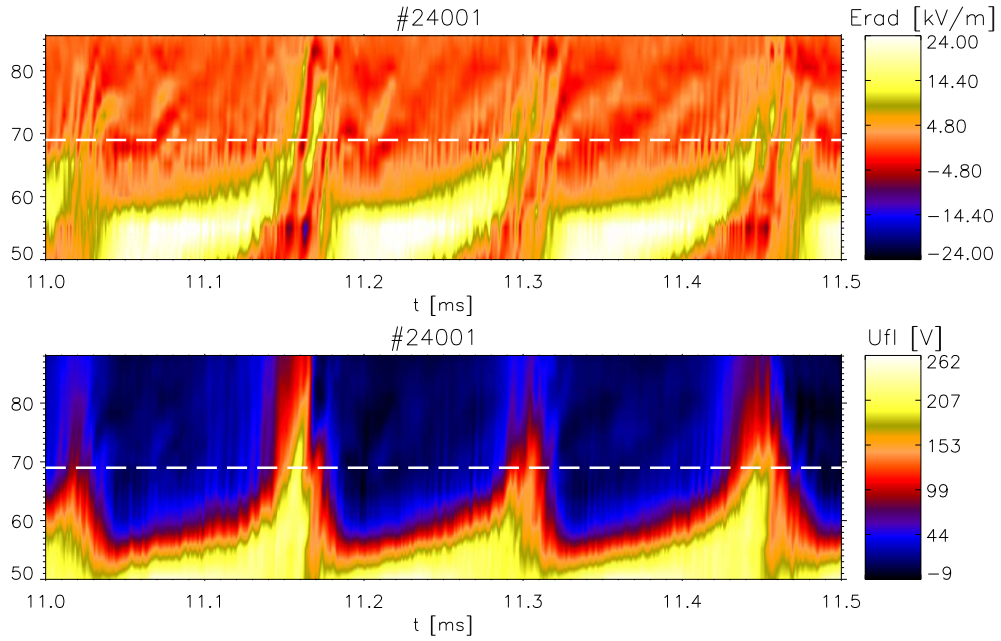

Figure 9.5: *Top panel: temporal evolution of radial electric field. Bottom panel: radial profile of floating potential. The white dashed line depicts LCFS.*

Interplay between E_{rad} and E_{pol}

The poloidal electric field can be obtained from the floating potential of the double rake probe. While the radial electric field rotates plasma in the poloidal direction, poloidal electric field E_{pol} contributes to the radial velocity either inward or outward, depending on the sign of E_{pol}.

Figure 9.6 shows the interplay between the radial and poloidal electric field. Values of E_{pol} are about three times lower ($\sim \pm 7$ kV/m) than the values of the E_{rad} ($\sim \pm 25$ kV/m). During the relaxation event, E_{pol} has positive value (yellow spots in the figure), the radial velocity according to the $E_{pol} \times B_{tor}$ drift is directed inward the plasma which helps to steepen the plasma density profile as depicted by the black arrows pointing down. On the other hand, during the collapse of the transport barrier (blue spots), the radial velocity points outward and contributes to repelling plasma to the wall.

The intensity of the H_α line emission (further only H_α) over-plotted by white curve starts to decrease, when the strong barrier is formed at $55 - 60$ mm and the velocity points inside the plasma column. This can be interpreted as a reduction of convective transport towards the wall and consequently the reduction of recycling. When the barrier starts decreasing (and the $E_{pol} \times B_{tor}$ drift velocity points out of the plasma), the plasma stream propagates towards the wall and the H_α (recycling) increases.

We have observed two types of patterns in the E_{pol}. Maxima are always inside the LCFS, but the minima (negative values) may develop in different radial positions: inside in LCFS or even outside in the SOL. Also, the frequency of the relaxation events varies. It seems to be dependent on the radial velocity of the barrier, also a dependence on the distance of the biasing electrode and the LCFS was investigated [59]. There are no clear results so far.

Radial profile of I_{sat}

Behaviour of the plasma density can be traced by examination of the ion saturation current I_{sat}. Temporal evolution of the radial profile of ion saturation current is shown in figure 9.7. U_{fl} and E_{rad} are plotted in the first two panels to show the dynamics the transport barrier. The VSL is at the position of 69 mm, as depicted by white dashed lines. Third panel shows I_{sat}, which is clearly modulated with the same frequency as of the potential relaxations. During collapse of the barrier, plasma is repelled towards the wall as described in previous sections and well confirmed by H_α over-plotted by white curves. In the bottom panel, the ion fluctuations[2] $I_{sat} - < I_{sat} >$ is plotted to emphasize the structure of I_{sat}.

Ion saturation current is proportional to the density, the relaxation events are thus connected with periodical expelling of plasma bursts towards the walls. Radial propagation of the density bursts can be estimated from the bottom panel as $\sim$ 0.5 km/s, as depicted by the sky-blue arrows in figure 9.7, bottom panels.

[2] $I_{sat} - < I_{sat} >$ is calculated for each probe separately, the time window for averaging the I_{sat} corresponds to the window in figure 9.7

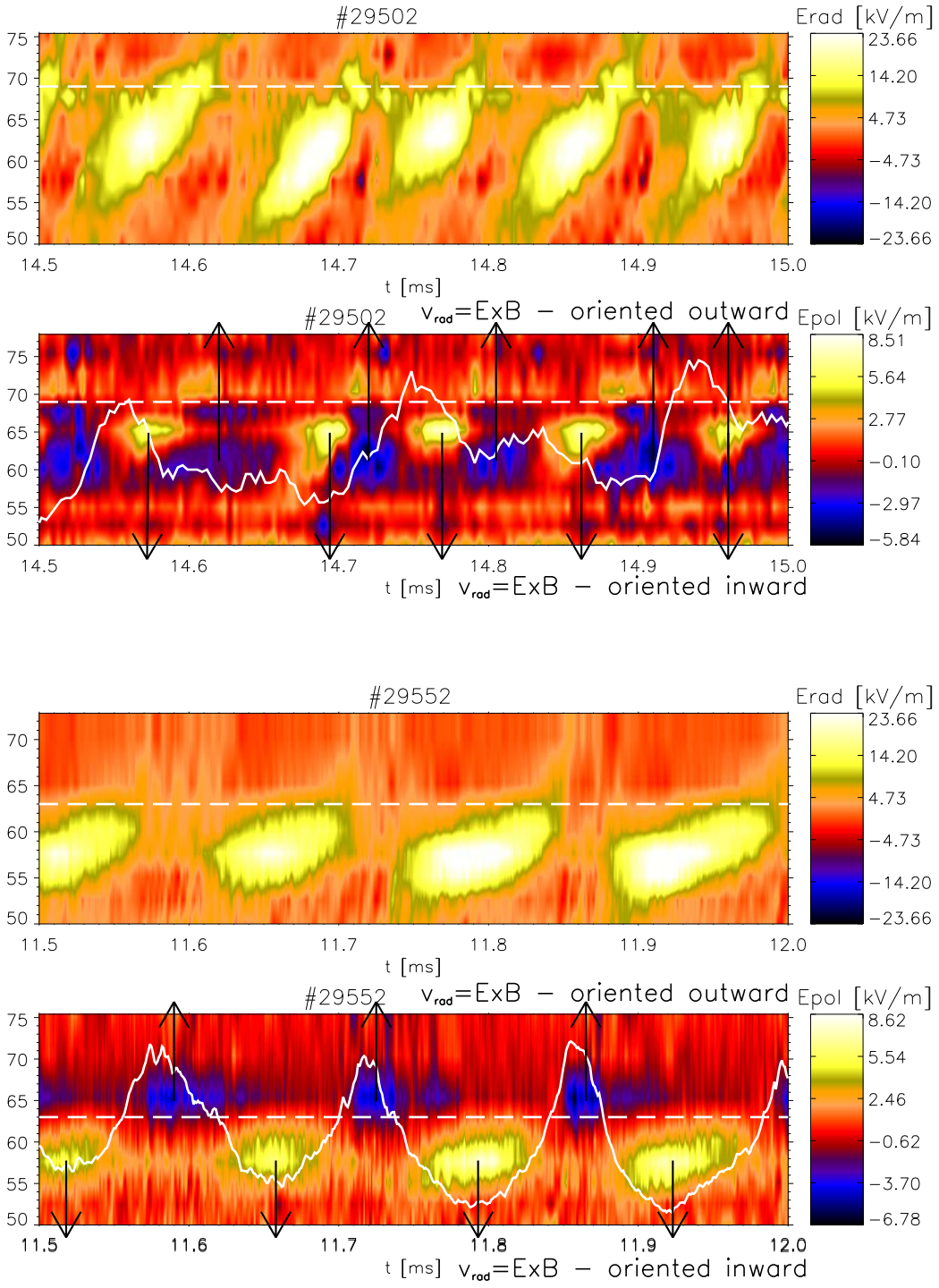

Figure 9.6: *Radial profile of E_{rad} (1st and 3rd panel) and E_{pol} (2nd and 4th panel) for two shots. The black arrows show the direction of the radial velocity. White curve is the temporal evaluation of H_α line intensity in arbitrary units, white dashed line depicts the LCFS.*

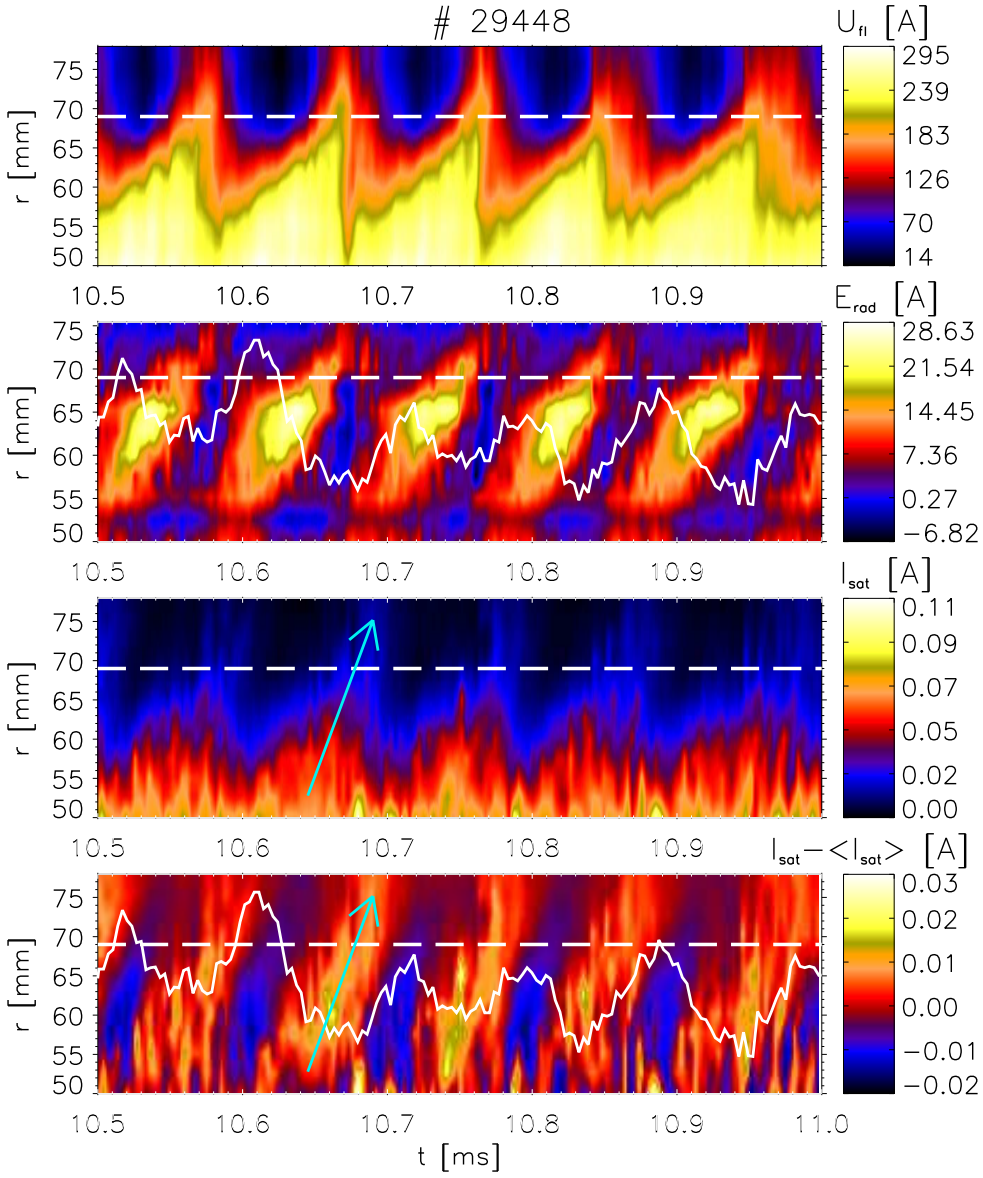

Figure 9.7: *Temporal evolution of the ion saturation current. U_{fl} and E_{rad} are plotted in first two panels. The third panel shows I_{sat}, the bottom one depicts $I_{sat} - < I_{sat} >$. VSL is denoted by white dashed lines, H_α chamber is o-plotted by white curves (in arbitrary units). Sky-blue arrows show the direction of the plasma streams movement.*

Ion flow velocities

Toroidal and poloidal ion flow velocities can be obtained by calculating the *Mach numbers*. The parallel $M_{\parallel}$ (toroidal) and perpendicular $M_{\perp}$ (poloidal) Mach number give the ratio of parallel and perpendicular velocity, respectively, to the ion sound speed.

Temporal evolution of $M_{\parallel}$ and $M_{\perp}$ (obtained using a validated 1D fluid probe model [60]) are shown in figure 9.8. We can observe an interesting interplay between these two flows: when the transport barrier is established and the poloidal flow takes the highest values due to fast rotation in the poloidal direction, the toroidal flow drops down to its minimum. Plasma rotates several times faster in the poloidal direction than in the toroidal one. During the collapse of the barrier, the poloidal flow is transformed into the toroidal one. The poloidal ion flow velocity reaches values up to 25 km/s, which is about half of the ion sound velocity (50 km/s).

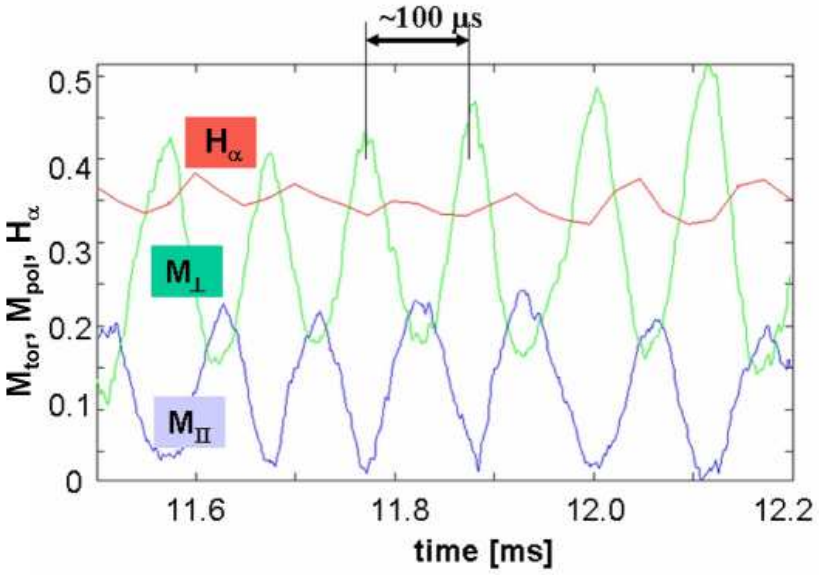

Figure 9.8: *Temporal evolution of parallel ($M_{\parallel}$, blue) and perpendicular ($M_{\perp}$, green) Mach numbers of ion flow measured by the Gundestrup probe, #24076. Red line is an evolution of the H_α line intensity (in arbitrary units) [61].*

Poloidal profile of U_{fl} and E_{rad}

Radial character of the transport barrier is clearly described by the probes immersed into the plasma from the top of the vessel. Now, we concern about the poloidal shape: whether the relaxations are poloidally symmetric, or whether it is a perturbation travelling in the poloidal direction. Unfortunately, only a segment of the SK ring Langmuir probes was connected due to insufficient number of the data acquisition system channels. In the following experiment, it was the upper HFS quarter of poloidal cross-section. Obtained time evolution of the floating potential poloidal profile is presented in figure 9.9, top panel. It shows that the relaxation events are poloidally symmetric (*poloidal mode number* $m = 0$).

Small periodical structures are also visible in temporal evolution of the poloidal profile of poloidal electric field shown in figure 9.9, bottom panel. The amplitude is not significant since the probes are located in the limiter shadow, at the radial position of 87 mm. Still, the patterns are in agreement with previous investigations and a clear poloidal symmetry of the poloidal electric field was confirmed. We can conclude that the barrier, though formed locally on one poloidal position, spreads over the poloidal cross-section homogeneously, we say that the plasma is "breathing".

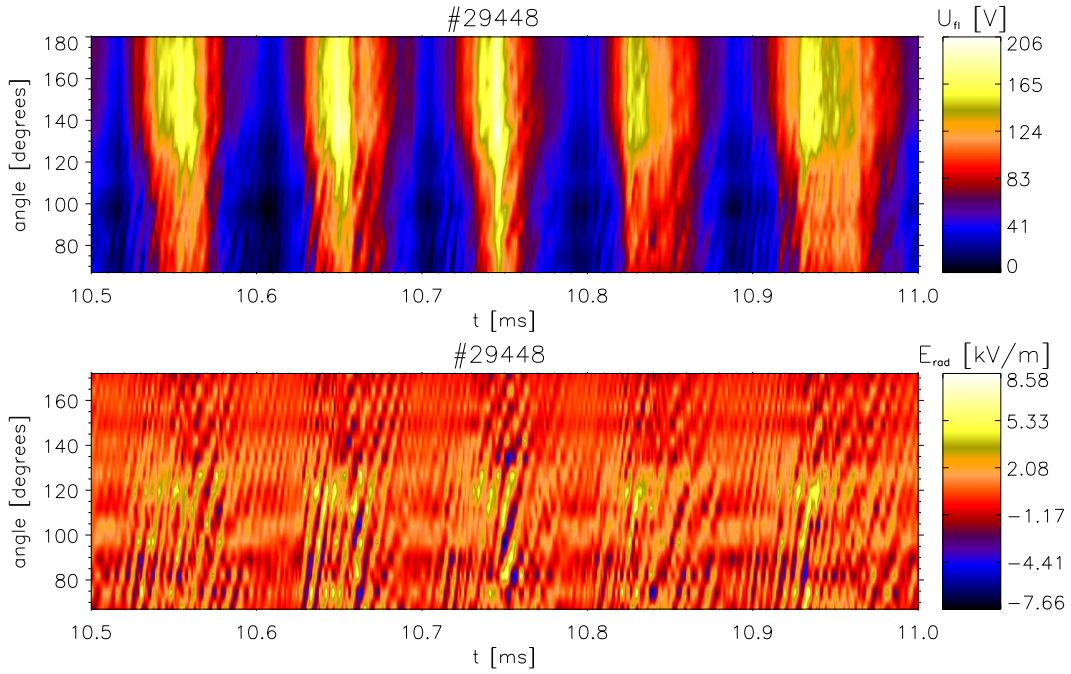

Figure 9.9: *Top panel: temporal evolution of the poloidal profile of floating potential. Bottom panel: temporal evolution of the poloidal profile of poloidal electric field. The y-axis signifies angular position of the probes: 0° is the LFS mid plane, 90° is the top of the chamber, 180° the HFS mid plane and finally 270° is the bottom. Only the upper HFS quarter of the poloidal cross-section is shown.*

Poloidal profile of I_{sat}

Poloidal behaviour of the density can be traced by examination of the ion saturation current I_{sat}. It was measured by individual segments of the SK ring: at LFS, top, HFS and bottom. The result is plotted in figure 9.10. Maxima of I_{sat} at the top of the chamber (bottom panel) agree with the profiles of E_{rad} and E_{pol} in figure 9.6 (top panels): when the plasma is repelled to the walls, the ion saturation current near the wall increases. H_α is over-plotted to clarify the effect. The highest transport of plasma is at HFS, the lowest one at LFS and bottom. The two top panels (LFS and bottom) have twice enlarged z-range (from 0 to 0.05 A) to emphasize the structures.

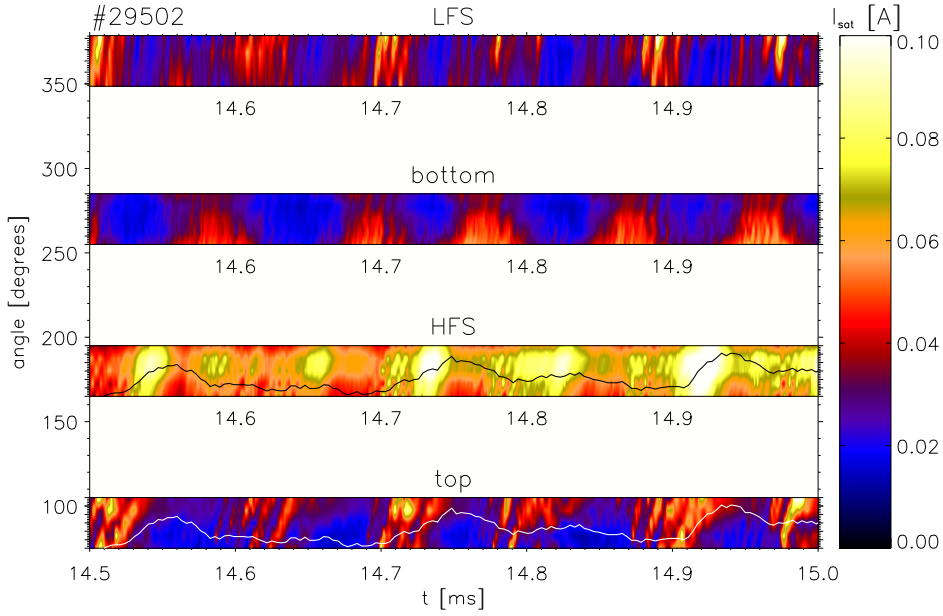

Figure 9.10: *Temporal evolution of the ion saturation current poloidal profile. Four segments were used for measurements: LFS, top, bottom and HFS. The white spaces correspond to areas where we have no measurements. The two top panels (showing LFS and bottom) have twice enlarged z-range (from 0 to 0.05 A) to emphasize the structures. The black and the white curve in the bottom panels shows the intensity of H_α line (chamber).*

9.3 Magnetic activity of plasma

Transport barrier was described by means of local measurements of electric properties at the plasma edge, namely by giving the radial and poloidal profiles of floating potential and ion saturation current. An interplay between E_{rad} and E_{pol} and between $M_{\parallel}$ and $M_{\perp}$ was demonstrated as well. The electric probes are sensitive neither to the magnetic activity of plasma, nor to phenomena acting deeper inside the plasma. In order to uncover an impact of the transport barrier on the magnetic characteristic, magnetic coils enclosing the plasma column were connected.

Magnetic coils of the SK ring measure the time derivative of the poloidal component of magnetic field. The provided measurements are of non-local character. Plot of the poloidal mode number intensity as a function of the poloidal number m versus frequency is given in figure 9.11 ($S(f,m)$ spectra). The $S(f,m)$ spectra during ohmic phase (left panel) show a magnetic island with $m \simeq 3-4$ and the frequency of 80 kHz, localized in the plasma centre at the magnetic surface with the safety factor $q = 3$. The magnetic coils are not at the same radius due to the downward shift of the plasma, which is the reason of uncertainty of the determination of the poloidal mode number.

When the relaxation events are present (right panel of figure 9.11), a strong peak in $S(f,m)$ spectra appears with $m = 0$ and with the frequency equal to the frequency of the relaxations ($\sim$ 10 kHz), while the original magnetic activity is suppressed. This indicates a significant redistribution of the current density profile. It is not clear yet why the relaxation events located at the very edge modify the magnetic activity deep inside of the plasma column.

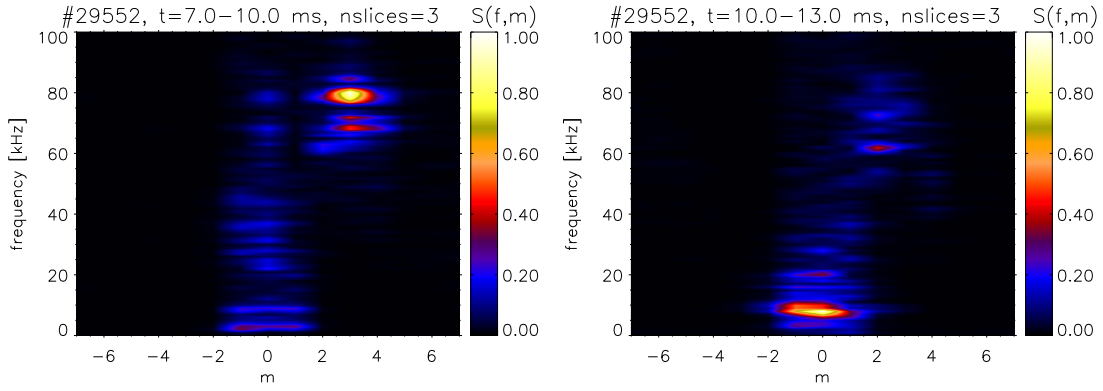

Figure 9.11: *S(f,m) spectra during the ohmic phase (left panel) and during the biasing phase (right panel) of the discharge.*

9.4 Summary

An onset of relaxation events is observed at the plasma edge of the CASTOR tokamak, during regimes with sufficiently strong biasing. These relaxations were studied with high spatial and temporal resolution by using a sophisticated system of plasma diagnostics.

The transport barrier raises and relaxes periodically with frequency $\sim$ 10 kHz. The maximal radial electric field is up to 30 kV/m, which causes $E_{rad} \times B_{tor}$ rotation in poloidal direction up to 25 km/s, comparable with the ion sound velocity (50 m/s).

An interplay between the parallel and perpendicular flows is observed. Radial transport of plasma towards the wall and consequent enhancement of influx of neutrals into the plasma is observed. Relaxation events are poloidally symmetric (both, the electric and the magnetic components).

Chapter 10

Study of statistical properties of fluctuations in the plasma boundary region of the TJ-II stellarator

Improved confinement regimes are reached whenever turbulent transport is reduced and a highly sheared plasma flow is observed. This behaviour is interpreted as turbulence suppression occurring when the shearing rate of $E_{rad} \times B_{tor}$ velocity drift exceeds a critical value related to broadband turbulence frequency. The investigation of the influence of $E_{rad} \times B_{tor}$ sheared velocities and magnetic topology on the statistical properties of turbulence in the plasma boundary region of fusion devices is a topic of great interest. This chapter presents results from the TJ-II stellarator.

Statistical properties of fluctuations have been investigated in different toroidal and linear devices [62]. Analysis of skewness and time asymmetry of floating potential and ion saturation current is described in [63]. This analysis was performed for several fusion devices (tokamaks, stellarators) and non-fusion low temperature devices. A clear deviation from Gaussianity was observed in the SOL while in the proximity of the VSL, the statistical properties of the fluctuations show near Gaussian character. It was concluded in [63] that this behaviour was probably caused by $E_{rad} \times B_{tor}$ shear effects. This conclusion was later called into question in [66], showing that magnetic topology might play a leading role to explain the modification in the statistical properties of fluctuations in the proximity of the LCFS.

The task of this chapter is to assess the role of both magnetic topology and sheared flows on the statistical properties of fluctuations in the plasma boundary region of fusion plasmas. For this purpose, experimental data from the TJ-II stellarator were analysed.

10.1 Stellarator

A stellarator is a magnetic device which serves for heating and confinement of plasma as well as tokamak. The main difference is in the way how the magnetic field, which is encharged to confine plasma, is generated.

Toroidal magnetic field of a tokamak is generated by external coils while the poloidal magnetic field is generated by the strong toroidal plasma current. In stellarator, in contrast, both the toroidal and poloidal magnetic fields are generated by external coils. The main difficulty of a construction of a stellarator lays in manufacturing the magnetic field coils since even a small error in the shape of the coils may result in a major error of the magnetic field encharged in confinement of the plasma.

The need of the toroidal current in tokamak imposes a limitation on operation of the machine. The current can not be induced an unlimited time which makes the regime pulsed. This is not convenient for a fusion reactor, moreover, the materials of the first wall must deal with high and fast changes of temperature. For these reasons, methods of driving the current after the transformer is saturated, are being developed. Stellarator, in contrast, is a steady-state device from its principle. On the other hand, stellarator miss the ohmic heating at the beginning of the discharge, the plasma must be generated by additional heating systems such as Electron Cyclotron Resonance Heating or injecting of neutral beams.

10.2 TJ-II

The TJ-II stellarator (shown in figure 10.1) is a facility with high degree of magnetic configuration flexibility, operating in CIEMAT in Madrid, Spain since 1998 [67, 68, 69]. A scheme of the magnetic field coils is in figure 10.2. Heating of the TJ-II plasma is achieved by an Electron Cyclotron Resonance Heating (ECRH) system and an Neutral Beam Injection (NBI) system [68, 69]. The ECRH system consists of two gyrotrons, each of them delivering microwave power up to 300 kW for the pulse length up to 1 s with the frequency of 53.2 GHz, which is the second harmonic

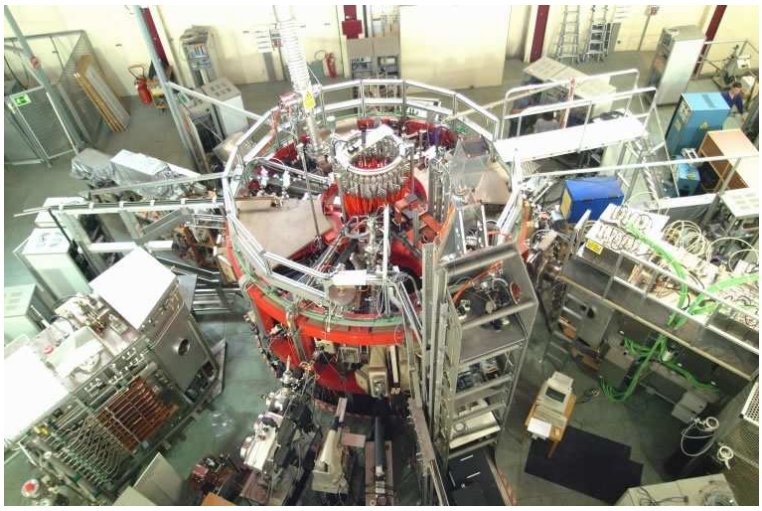

Figure 10.1: *TJ-II stellarator.*

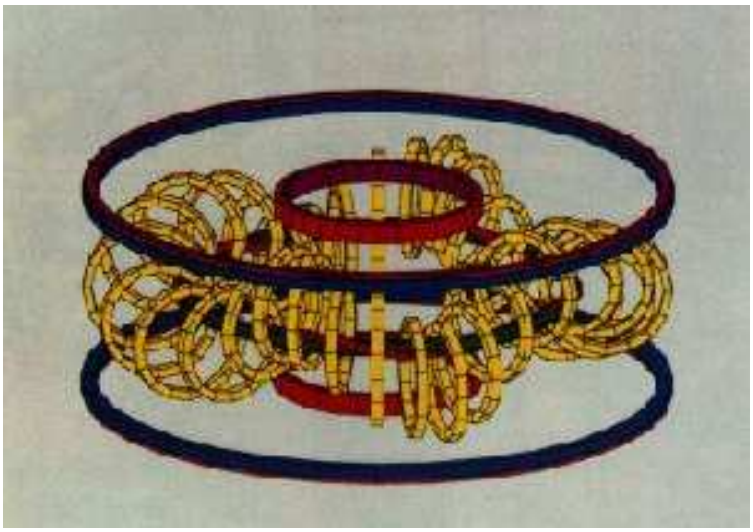

Figure 10.2: *Scheme of magnetic field coils of the TJ-II stellarator.*

of the electron cyclotron frequency in the TJ-II plasma. The NBI system includes two hydrogen beams of the power of 1 MW each, with the beam energy 40 keV and the maximal pulse length of 300 ms.

The physical programme of the TJ-II stellarator is focused mainly in plasma confinement [70, 71] and transport studies [69, 71, 72, 73], including the influence of heating of the plasma [74], and including modelling studies. Another topics are the studies in magnetohydrodynamics and basic theory. Its high magnetic configuration flexibility enables detailed description of the influence of magnetic topology on plasma confinement [69].

Main parameters of the TJ-II stellarator:

Major Radius, R	1.5 m
Minor Radius, a	< 0.22 m
Toroidal magnetic field, B_0	≤ 1.7 T
Power of the ECRH, P_{ECRH}	≤ 600 kW
Power of the NBI, P_{NBI}	≤ 2 MW

10.3 Experimental set-up

In order to investigate the statistical parameters of TJ-II stellarator plasma, data from reciprocating Langmuir probe system [75] were analysed. The probe head consists of three groups of Langmuir probes at different radial, poloidal and toroidal positions as shown in figure 10.3. This arrangement allows to measure radial profiles of different magnitudes at the plasma edge and to obtain the perpendicular and parallel flows as well as to deduce the radial turbulent particle flux. Each group includes one tip collecting the ion saturation current and two tips measuring the floating potential with sampling rate of 2 MHz. A boron-nitride probe head supports the tungsten tips (0.7 mm in diameter and 2.5 mm in length) which can be either exposed to the plasma in one radial position, or they can be quickly moved in and out of the plasma, scanning the plasma boundary during one shot.

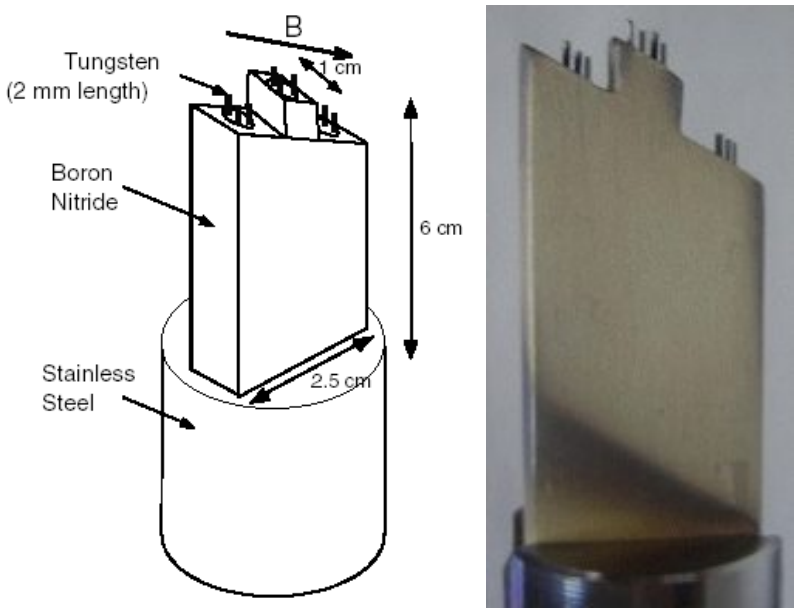

Figure 10.3: *Head of the reciprocated Langmuir probe system used in the TJ-II stellarator [76].*

A graphite electrode was used for biasing of the edge plasma region. The electrode head is mushroom shaped, made of 2-D Carbon composite, with height (radial extension) of 12 mm and the diameter of 25 mm. The electrode was inserted typically 2 cm inside the LCFS and biased with respect to one of the TJ-II limiters (typically +300 V).

10.4 Shears in the TJ-II stellarator

Previous experiments have shown that the plasma density (or density gradient) plays a crucial role in establishing the $E_{rad} \times B_{tor}$ shear in the TJ-II stellarator [76]–[81]. A threshold density has been identified to trigger the development of edge sheared flows. On the contrary, in plasmas with density below this threshold value, there is no natural shear.

The natural shear development mechanism can be described in the following way. With increasing density the floating potential at the edge decreases. When the density is above a critical value, the floating potential becomes negative and the shape of the radial electric field E_{rad} develops: it becomes oriented radially inward. The $E_{rad} \times B_{tor}$ drift develops a poloidal velocity shear, the level of fluctuations decreases, the edge gradients increase and a transport barrier is established. The situation is shown in figure 10.4, where the radial profiles of the ion saturation current (proportional to the density) and the floating potential for different values of the line averaged plasma density are plotted.

A similar effect can be obtained by imposing a radial electric field at the edge plasma externally [82]. Experiments with biasing of the edge plasma by means of an immersed electrode charged to a DC voltage with respect to the limiter have shown a reduction of the turbulent transport and improvement of confinement. The configuration enables reaching stronger E_{rad} than in the case of the natural shear which results in establishing a higher transport barrier and better confinement.

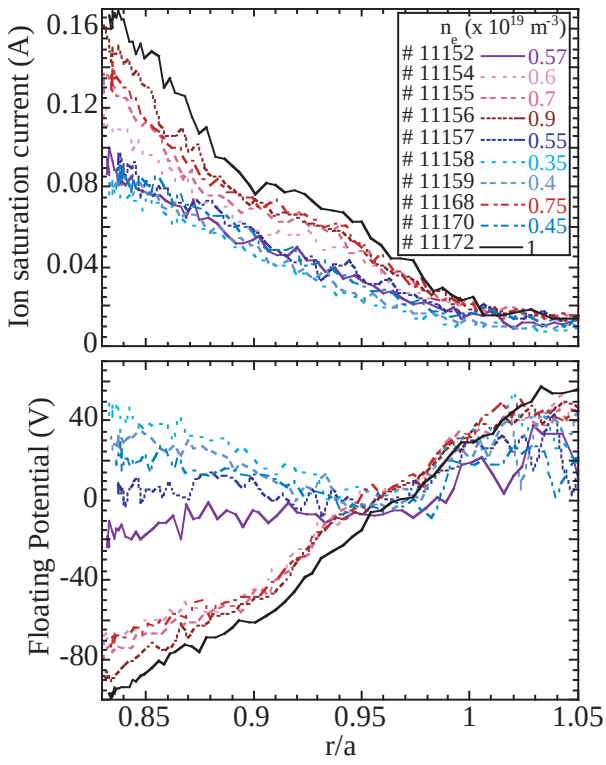

Figure 10.4: *Radial profiles of ion saturation current and the floating potential for different values of the plasma density [77].*

10.5 Experimental results

To shed more light on the previous results, regimes with and without the natural shear as well as regimes with imposed $E_{rad} \times B_{tor}$ shear were investigated. The main outstanding questions are:

- What is the role of the natural $E_{rad} \times B_{tor}$ shear in the statistical parameters of fluctuations?
- How the situation changes by imposing an $E_{rad} \times B_{tor}$ shear externally?
- What is the role of the magnetic topology?

Radial profiles of the floating potential of evaluated shots in ohmic regime (blue triangles) and during biasing (red diamonds) are presented in figure 10.5.

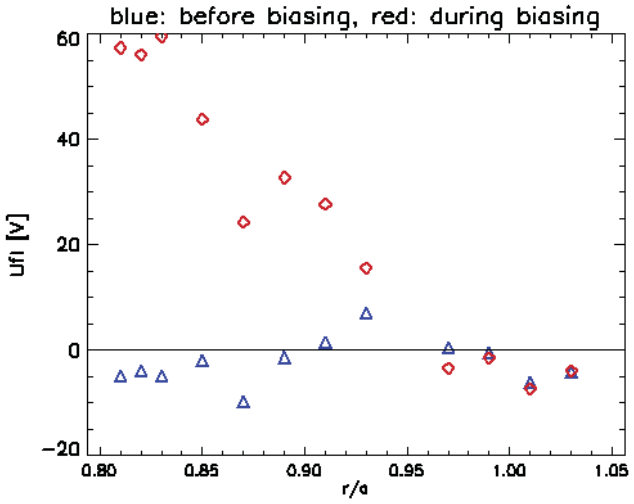

Figure 10.5: *Radial profile of the floating potential during ohmic regime (blue triangles) and during biasing (red diamonds). The radial position $r/a = 1$ is the LCFS.*

A broad spectrum of statistical properties was investigated: skewness, kurtosis[1] and time asymmetry A of both ion saturation current and floating potential. The clearest results of the statistical analyses come from the time asymmetry of the floating potential $A(U_{fl})$, thus only this parameter will be discussed in the following.

Parameter A is defined as the skewness of time derivative of the fluctuating part of the signal [63]:

$$A = \frac{1}{N} \sum_{j=0}^{N-1} \left(\frac{x'_j - \bar{x'}}{\sqrt{\sigma'^2}} \right)^3 \tag{10.1}$$

where N is the number of samples, $x'_j = \mathrm{d}x/\mathrm{dt}$ is the j-th element of the time derivative of the signal ($x'_j = [x_{j+1} - x_j]/\Delta t$ where Δt is time between two samples), and $x'_j = \frac{x_{j+1} - x_j}{\Delta t}$ are defined as the mean value of x' and the variance of x', respectively, according to (6.11) at page 55.

[1] See section 6.1.1 for the definitions.

The A parameter shows the time asymmetry of the fluctuating part of the signal. For a signal symmetric in time, $A = 0$ and consequently the time derivative has a Gaussian distribution. On the other hand, $A < 0$ is for the signal with structures with, in average, shorter rising time than the decay time (in average). Finally, $A > 0$ shows patterns which rise slower than they decay.

Let us see how to interpret the parameter A: In the SOL, blobs propagate from the LCFS outwards. We consider them to be mushroom-like shaped, consisting of two lobes, one with positive potential and one with negative, as described in [64, 65]. They have a steep front edge and they carry high temperature and density. When such blob passes over a probe, the floating potential shows a steep decrease in the structure, since $U_{fl} = \Phi - 2.5T_e$ and the overall plasma potential Φ does not change on average. Fast drop and slow raise of the structures in U_{fl} corresponds to negative values of $A(U_{fl})$. In the context of our analysis, negative A implies the presence of blobs.

Time evolution of the time asymmetry of floating potential ($A(U_{fl})$) in different radial positions is plotted in figure 10.6. The data were obtained on the shot-to-shot basis, each panel thus corresponds to one shot and one radial position. The left two columns show shots with high density (natural shear). In fact, it is one column divided in two running from the deepest position (top left plot) to the edge position (bottom right) of the probe. The right column shows low density data. The biasing phase of discharge is depicted by vertical lines. From the figure, we can conclude following:

1. **Natural shear - high density regimes** ($n > n_{\text{threshold}}$): $A(U_{fl})$ is negative inside the VSL and tends to zero around the shear location. It is demonstrated in figure 10.6 in the left and centre panel, during the ohmic phase of the discharge. According to our interpretation, this behaviour corresponds to the presence of blobs inside the VSL, which are dissipated at the proximity of the VSL.

2. **No natural shear - low density regimes** ($n < n_{\text{threshold}}$): $A(U_{fl})$ is negative at all radii, inside plasma it tends to come to zero as shown in figure 10.6 in the right panel, during the ohmic phase of the discharge. Number of blobs increases in the direction outwards.

3. **Biasing induced shear flow**: For the high density shots ($n > n_{\text{threshold}}$), the characteristics of $A(U_{fl})$ changes systematically in the radial direction. In the plasma region ($r/a \approx 0.83 - 0.91$), it rises to positive values whereas outside ($r/a \approx 0.99 - 1.03$) it becomes negative as shown in figure 10.6. Around the shear layer, $A(U_{fl})$ remains unchanged, around zero. Similar trends have been found at low density. These experiments clearly show the importance of electric fields on the statistical properties (parameter A) of fluctuations. This situation is shown in figure 10.6 in the left and centre column (for high density shots) and in the right column (for the low density shots), both during the biasing phase of the discharge (depicted by black vertical lines). The drop of the A in the SOL implies an increase of blobs.

4. **The role of magnetic topology**: Previous investigations [66] were well reproduced, showing that the time asymmetry of floating potential changes

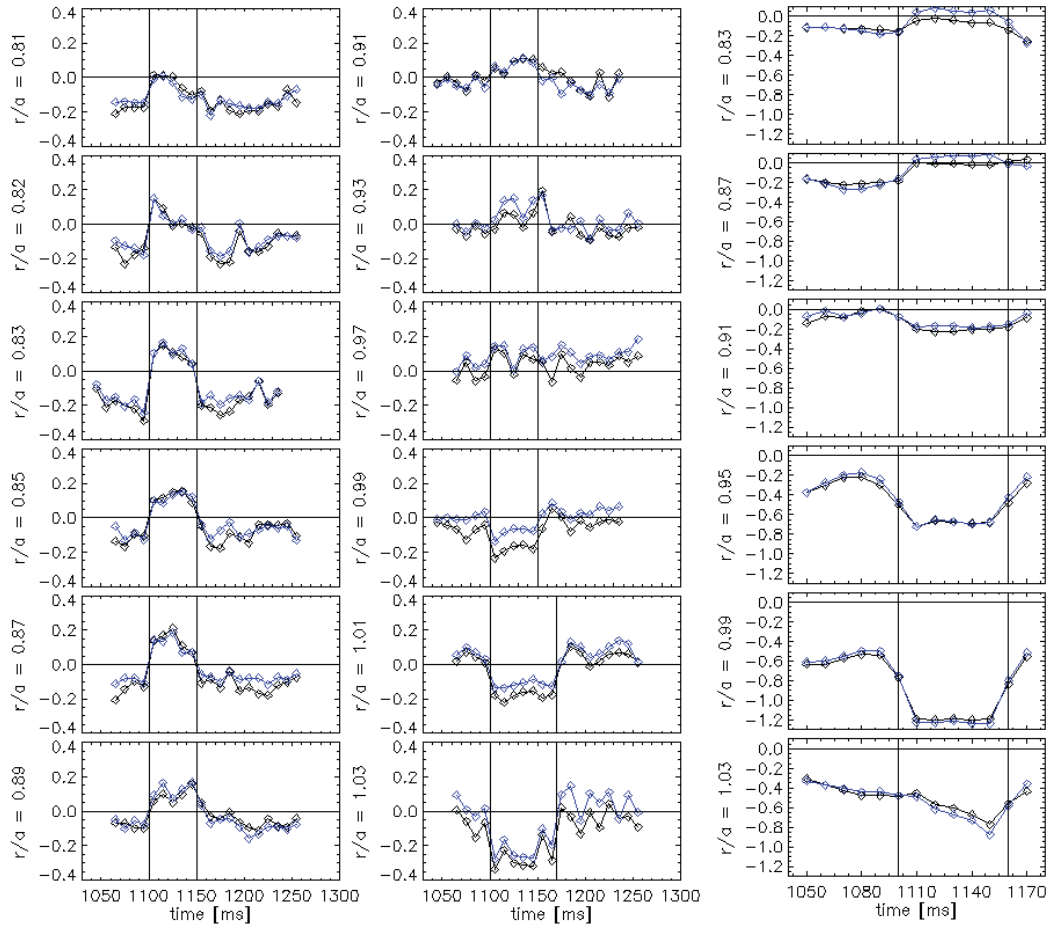

Figure 10.6: *Time evolution of the time asymmetry of floating potential ($A(U_{fl})$) for different radial positions (r/a). Black diamonds correspond to the probe 1, while blue one to the probe 2 of the central top group (see figure 10.3). Left and centre columns: regime with high density shots ($n > n_{\mathrm{threshold}}$), radial positions of the probes run from outward: from the top left panel to the bottom right one. Right column: regime with low density shots ($n < n_{\mathrm{threshold}}$). The biasing phase is depicted by the vertical lines.*

with the magnetic topology, increasing significantly from the open field lines region (SOL) to the region inside the LCFS as shown in figure 10.7. Inside the plasma bulk, the development of $E_{rad} \times B_{tor}$ shear does not change the behaviour of $A(U_{fl})$. The lower amplitudes of A in the SOL during the high density regimes (red lines) point to decrease of the number of blobs. This is an action which we expect from the natural shear.

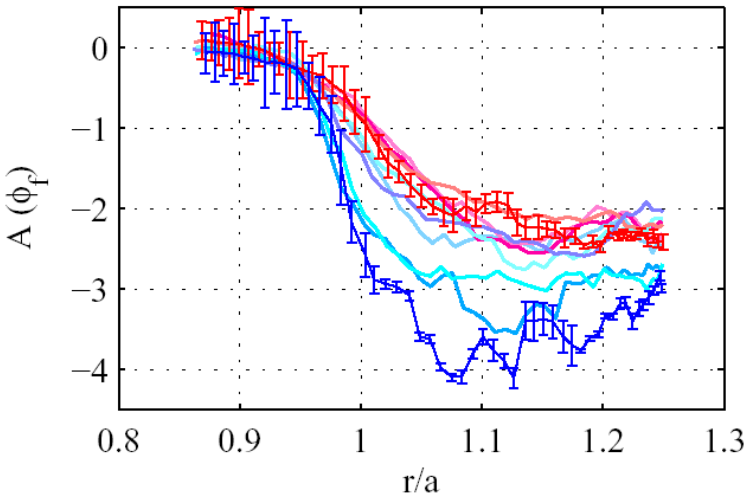

Figure 10.7: *Radial profile of time asymmetry of floating potential (named as Φ_f in the original work) [66]. Blue lines: low density (no shear). Red lines: high density (natural shear).*

10.6 Summary

In conclusion, the investigation of the statistical properties of fluctuations in the plasma boundary region of the TJ-II stellarator shows that the time asymmetry of turbulent bursts is affected both by magnetic topology and the radial electric fields. This means that the mechanism leading to changes in the shape of turbulence in the edge plasma is caused not only by the $E_{rad} \times B_{tor}$ shear, but it is also related to the magnetic topology.

Part III

Ball-pen probe

Chapter 11

Introduction to the Ball-pen probe measurements

A new probe, so-called "Ball-pen probe", was developed in IPP Prague and used in the CASTOR tokamak, the RFX-mod reversed field pinch and also in the ASDEX Upgrade tokamak. The probe is an innovative type of probe which is able to measure directly the plasma potential in magnetized plasmas. Moreover, plasma potential fluctuations measurements can be used for evaluation of the diffusion coefficient using a technique presented in following chapters.

Understanding the electric field and its turbulence in magnetic confinement devices is a very important tasks in the fusion research as explained in previous chapters. Proper knowledge of the plasma potential is required for calculation of the electric field and also for verification of numerical simulations of SOL [84, 85].

So far, we discussed only floating potential (U_{fl}) of the Langmuir probes in this thesis. The electric field was estimated from U_{fl}, usually neglecting the gradient of the electron temperature. This step was justified in chapter 7. Precise values of the plasma potential and electron temperature can be obtained from swept Langmuir probes (a harmonic voltage is applied to the probe in order to obtain the current voltage characteristics), which is a method with a poor time resolution. Another ways of direct measurement of plasma potential are by means of emissive probes [86] and heavy ion beam probes [87], though these methods are also burdened by various technical problems and peculiarities in measured data interpretation. The Ball-pen probe (BPP) is able to provide the plasma potential and the electron temperature with high time resolution.

Another important feature of the BPP is ability to estimate the plasma diffusion coefficient. The diffusion coefficient is also one of demanding topics since its calculation requires knowledge of the density gradient, the ion sound speed and further qualities as described in section 4.3.6.

The Ball-pen probe was developed in the Institute of Plasma Physics AS CR in Prague [19, 20, 88, 89]. It was used in several fusion facilities: in the CASTOR tokamak [19, 20, 88, 89], in the ASDEX Upgrade tokamak [90], and in the reversed field pinch RFX-mod [91].

11.1 Principle of the Ball-pen probe

The Ball-pen probe takes advantage of the difference between the electron and ion Larmor radii. It was developed on the basis of the Katsumata probe concept [92]. The BPP is made of a ceramic tube with a metal collector of a conical shape inside as shown in figure 11.1. The axis of the probe head is oriented perpendicularly to

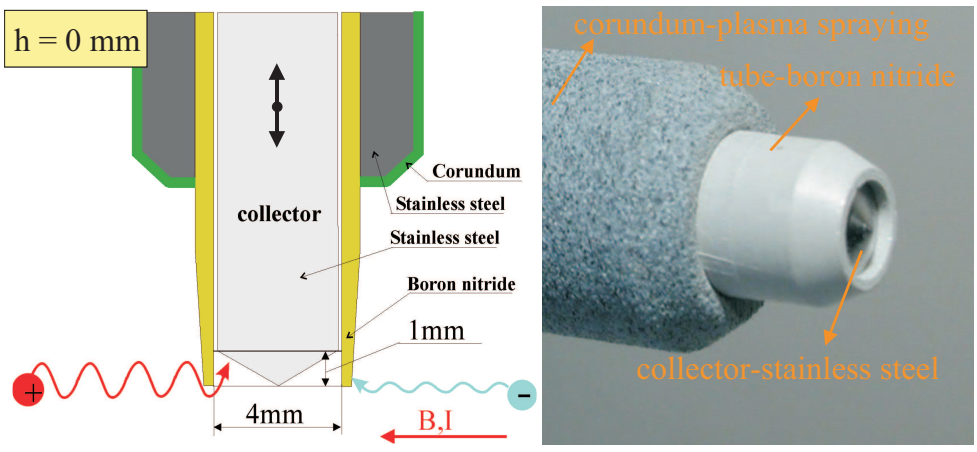

Figure 11.1: *Ball-pen probe developed for the CASTOR tokamak. Left panel: a schematic illustration of the probe principle. Right panel: picture of the probe head.*

the magnetic field lines. The ions can penetrate deep into the ceramic shaft due to their larger gyro-radii, while a certain part of the electrons is shielded. The collector can be used for measurements of either floating potential, or ion saturation current; it is movable with respect to the ceramic shaft.

According to the Langmuir probe theory for Maxwellian plasmas, the floating potential of the collector U_{fl} can be expressed as

$$U_{fl} = \Phi - \frac{k_B T_e}{e} \ln \left(\frac{I_{sat}^-}{I_{sat}^+} \right) \tag{11.1}$$

where Φ is the plasma potential, T_e is the electron temperature, I_{sat}^- and I_{sat}^+ is the electron and ion saturation current, respectively. For a certain position of the collector within the shielding tube, the I_{sat}^- and I_{sat}^+ are balanced and the potential of the floating BPP is equal to the plasma potential [19, 93].

The diffusion coefficient is evaluated from the spatial decay of power spectra of the BPP collector during ohmic discharge. The spectrum decays as the collector is pulled inside the shielding shaft; the decay is faster for higher frequencies. This is a typical behaviour of a diffusion process inside the probe. A model was developed and applied on experimental data, the results are published in articles presented in next two chapters.

Chapter 12

A probe-based method for measuring the transport coefficient in the tokamak edge region

Czechoslovak Journal of Physics, Vol. **56** *(2006), No. 12.*

Chapter 13

Novel Technique for Direct Measurement of the Plasma Diffusion Coefficient in Magnetized Plasma

Contributions to Plasma Physics, Vol. **48** *(2008), No. 5-7.*

Chapter 14

Measurements with Ball-pen probe on RFX-mod

The Ball-pen probe was installed and tested in the RFX-mod reversed field pinch in order to verify the behaviour of the probe in low magnetic field (~ 0.1 T). In this chapter, we give a short introduction to the RFX-mod facility, the new system for measurements the edge plasma parameters. Finally, we introduce the Ball-pen probe designed for the RFX-mod and we show preliminary results of calculations of the diffusion coefficient.

14.1 The reversed field pinch configuration

A reversed field pinch (RFP) is a magnetic device of the same principle as tokamak: the plasma is confined by a strong magnetic field of helical shape and driven by a strong toroidal current induced by a transformer. The main difference is the shape of the magnetic field and its temporal evolution.

While the toroidal magnetic field in tokamak is produced by external coils only, being ten times higher than the poloidal magnetic field and stationary during the discharge, the situation in RFP is more complex. The plasma confinement in RFPs is achieved by both the toroidal and the poloidal magnetic fields which are of the same order. Moreover, the toroidal magnetic field changes during the start-up phase of the discharge; during the flat-top phase it remains constant.

At the beginning of the discharge, the B_{tor} is generated by external coils only. When the plasma is formed, the poloidal component of the plasma current generates an additional B_{tor} in the inner part of the plasma column. It is worth noting that the helicity of RFP is much higher than of tokamak, thus this effect is negligible for tokamak, but significant for RFP. As the toroidal winding acts as a flux conservant, they respond to the rising toroidal field in the plasma core by decreasing and even reversing it at the edge. The level of reversing is adjusted by the value of the plasma current, but it can be also controlled by external circuits. The magnetic field configuration is schematically shown in figure 14.1.

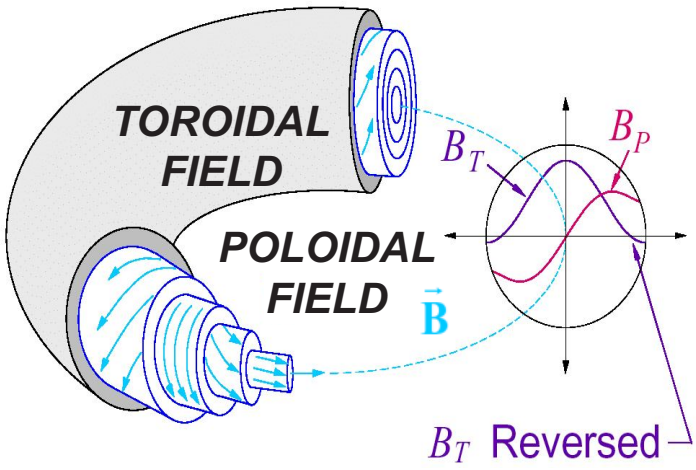

Figure 14.1: *A scheme of magnetic field in RFP during the flat-top phase of discharge. The toroidal magnetic field in edge region has the opposite direction than in the centre of the vessel.*

Parameters describing the RFP configuration are the *pinch parameter*

$$\Theta = \frac{B_{pol}(a)}{< B_{tor} >} \tag{14.1}$$

and the *reversal parameter*

$$F = \frac{B_{tor}(a)}{< B_{tor} >} \tag{14.2}$$

where $B_{pol}(a)$ and $B_{tor}(a)$ are the poloidal and the toroidal components of the magnetic field at the wall position and $< B_{tor} >$ is the toroidal magnetic field averaged over the plasma cross-section.

14.2 RFX-mod experiment

The Reversed Field eXperiment (RFX) reversed field pinch, operating in the Consorzio RFX in Padova, Italy, was recently modified (RFX-mod, see figure 14.2) in order to increase the passive and active control of magnetohydrodynamic modes [94]. For this, the former aluminium shell was replaced by a new copper one, with significantly lower time constant [95]. The new system consisting of 192 saddle coils installed inside the machine. It provides the active control of magnetic instabilities. Moreover, a new integrated system of internal sensors (ISIS) has been installed in order to detect the electrostatic and magnetic fluctuations [95, 96].

Main parameters of the RFX-mod:

Major Radius, R	2.0 m
Minor Radius, a	0.5 m
Maximum plasma current, I	2.0 MA
Maximum applied toroidal field	0.7 T
Current rise time	$15 - 50$ ms
Flat top time	250 ms
Core flux swing	15 V·s
Inductive storage	72.5 MJ

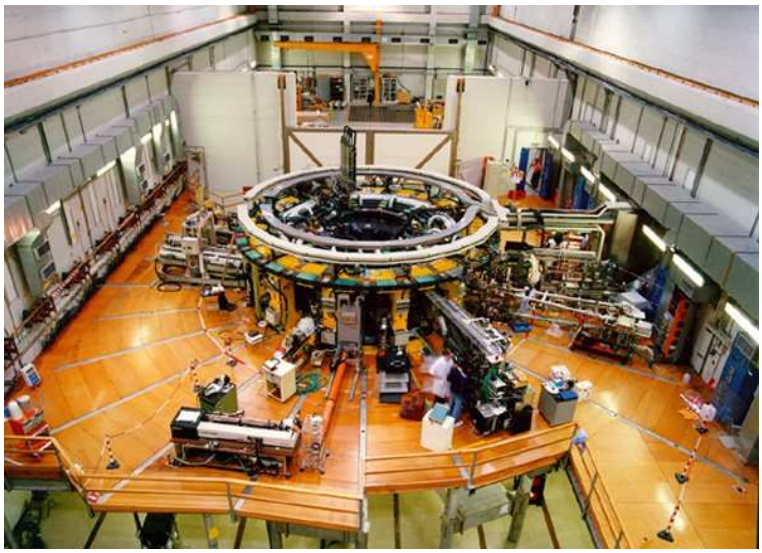

Figure 14.2: *RFX-mod experiment.*

14.3 Characteristics of turbulence in RFX-mod

Set-up and parameters of the ISIS system

The ISIS system [96, 97] consists of a large set of Langmuir probes placed on the first wall of the RFX-mod device [98] and of magnetic probes installed 16 mm below the tiles covering the first wall: 131 magnetic pick-up coils, 97 electrostatic probes, 8 saddle coils and 8 calorimetric sensors. The probe layout is complex; the main features are the presence of one full toroidal array of 72 Langmuir probes and of two toroidal arrays of 96 magnetic probes each. One poloidal array of each kind of probes is also present. As another diagnostics for detecting the plasma turbulence, the gas-puffing imaging (GPI) diagnostics [99] with range of 40 mm is used. A picture of the RFX-mod chamber inner walls with depicted positions of some electrostatic and magnetic probes is in figure 14.3.

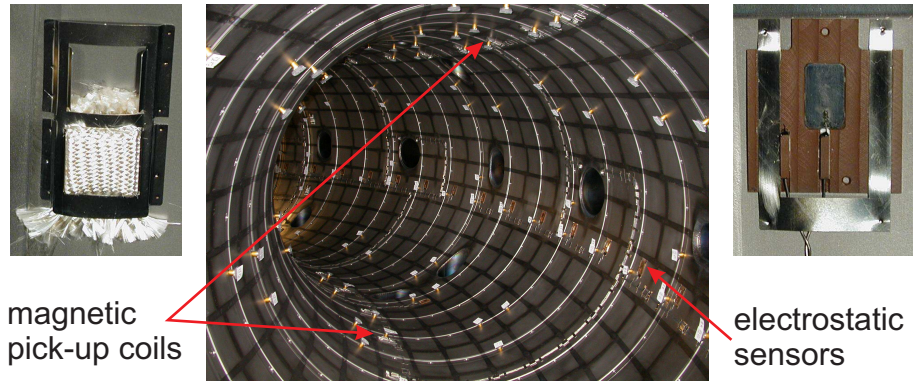

Figure 14.3: *RFX-mod vacuum vessel from inside. The magnetic pick-up coils are below the carbon tiles, the electric sensors are protruding from apertures in the tiles.*

Example of the power spectra in RFX-mod

An example of typical power spectra in the SOL of the RFX-mod is in figure 14.4. The spectra were obtained from the electrostatic probes and magnetic sensors of ISIS and from the GPI system. The power spectra show similar characteristics to other fusion facilities as described in [100, 101]. This fact implies universality of the turbulence and turbulent transport in spite of the one order lower magnetic field.

14.4 Experimental set-up of the Ball-pen probe measurements

The Ball-pen probe for the RFX-mod experiment consists of four collectors at fixed positions placed inside a single ceramic holder (boron nitride) as shown in figure 14.5. Radial profile of plasma potential and electron temperature was obtained from averaged values of the collector potential inside the shaft and published in

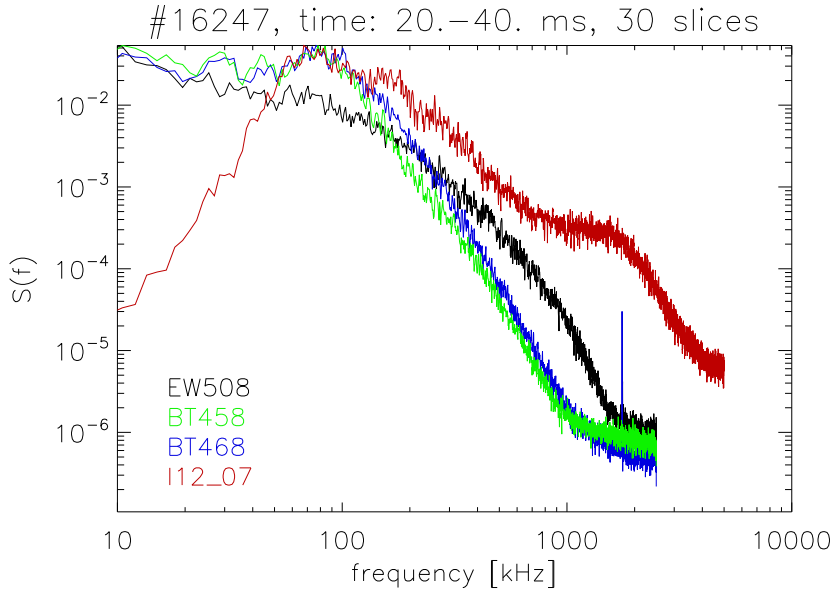

Figure 14.4: *Typical power spectra, #16247 (normalized). Black curve represents an electrostatic probe, green and blue are from magnetic probes and red is from the GPI.*

[91]. The decay of the plasma potential fluctuations inside the shaft was used for evaluation of the diffusion coefficient [33].

Two shot series with different F parameter were performed for the measurements of floating potential of the Ball-pen collectors. First series was performed with $F = -0.2$, the second one with $F = -0.04$.

The Ball-pen probe was inserted from the LFS at the mid plane. The measurements were taken with different radial positions of the Ball-pen probe on shot-to-shot basis.

Figure 14.5: *Ball-pen probe head for the experiment on RFX-mod.*

14.5 Evaluation of the diffusion coefficient

Fluctuations of the plasma potential decrease for deeper positions of the collector. The power spectra of the potential fluctuations show an exponential decay with frequency as shown in figure 14.6. In some cases, however, the behaviour of the power spectra has a different character than diffusion (higher frequencies drop faster for more shallow positions of the collector). Further analyses connected with other diagnostics (mainly magnetic) must be performed to explain this phenomenon.

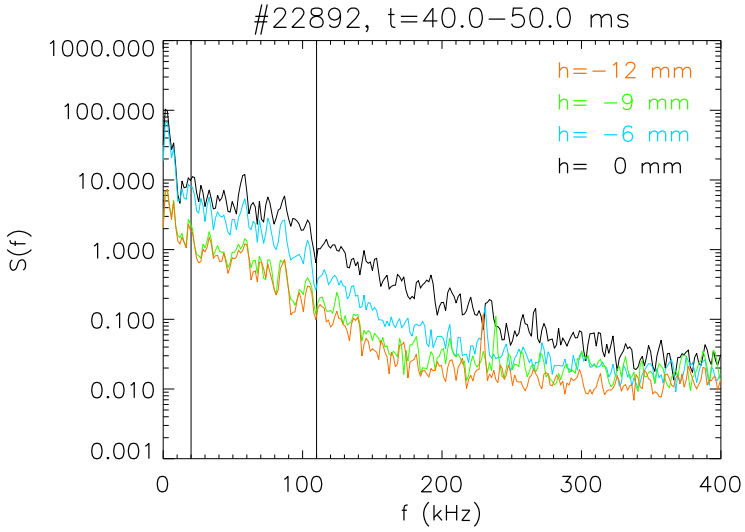

Figure 14.6: *Example of power spectra obtained by the Ball-pen probe collectors with different depth h. Measurement was performed at the RFX-mod.*

The diffusion coefficient (D) was evaluated by the method described in chapters 12, 13 for both series. To do so, we combined many parameters, like frequency intervals and number of slices used for the statistical evaluation of power spectra. We obtained radial profiles of the diffusion coefficient.

For the $F = -0.2$, D ranges from 10 m^2/s to 120 m^2/s as shown in figure 14.7. Close to the limiter, D takes the lowest values and increases to the centre. Inside the plasma, after $30 - 40$ mm, D tends to drop again. In the area behind the limiter, D increases in the direction outwards. The increase of D in the edge plasma is consistent with evaluation of D by other methods, namely by Langmuir probes and a homodyne reflectometer [102].

For $F = -0.04$, the situation is less clear. D varies from 10 to 50 m^2/s in the edge, in the positions deeper than 10 mm, D tends to increase to values around 100. It is problematic to use our method in this discharge regime since behaviour of the power spectra showing opposite trend than diffusion occurs more often in this series. More experiments and analyses need to be done to clarify this phenomenon, as mentioned above.

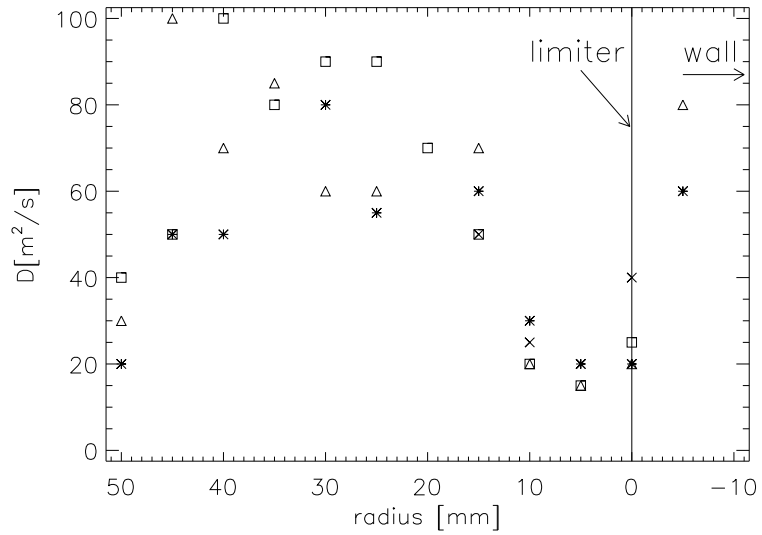

Figure 14.7: *Radial profile of diffusion coefficient for the reversal parameter* $F = -0.2$ *obtained by several combinations of the fitting parameters: asterisks are for 5 ms of time window and the signal divided into 50 slices for evaluation of power spectra. Rectangles denote 10 ms, 50 slices, crosses are for 15 ms, 50 slices and triangles represent 5 ms, 40 slices. Frequency interval used for evaluation of* D *is* $30 - 90$ *kHz. The vertical line depicts the limiter position.*

Part IV

Conclusions

Chapter 15

Conclusions

The main results of the work carried out in the scope of my PhD studies are summarized in this chapter.

Work on this PhD thesis was carried out mainly at the Institute of Plasma Physics of the Academy of Sciences of Czech Republic, part of it was done at the TJ-II stellarator in Madrid and at the RFX-mod reversed field pinch in Padova. It was focused on the study of the edge plasma turbulence by means of electric probes and on the development of new diagnostic tools for measurements in the plasma boundary region. The thesis can be summarized in the following points. References to the relevant publications are given in chapter 16: section 16.1 lists the journal articles, section 16.2 the conference proceedings and section 16.3 my own presentations at international conferences - presentations of my colleagues on similar topics are not included. The journal articles and conference proceedings where I am the first author are **emphasized in bold font**.

Part I - Introduction

The first part is devoted to an overview of fusion research and to some basics about tokamak configurations. The CASTOR tokamak was introduced along with the diagnostic tools used for measurements in this thesis. The geometry of the edge plasma and transport at the edge was briefly described, targeting the special features of the CASTOR tokamak.

Experiments with improved confinement were compared with experiments in standard regimes. The global plasma parameters were shown as well as the radial profiles of the floating potential, radial electric field and ion saturation current at the plasma edge.

In the last section, the statistical tools used for the experimental data analyses were described.

The results with my participation relevant to the Part I were published in [16.1-10], [16.2-1], [16.2-8] and [16.2-13].

Part II - Fluctuation measurements

In this part, the measurements of edge plasma fluctuations mainly by means of arrays of electric probes are presented. The results were presented at several international conferences and published in journals.

1. **Measurements of sheared electric fields and flows at the plasma edge of the CASTOR tokamak**

   - The experimental data were collected by the double rake probe and the poloidal ring of Langmuir probes.
   - Two methods for evaluation of the phase velocity were used: exploiting the cross-correlation and the cross-coherence.
   - The poloidal phase velocity of fluctuations was established from signals of adjacent Langmuir probes placed in different poloidal positions.
   - A radial profile of the velocity was obtained and compared to a theoretical calculation from the $E_{rad} \times B_{tor}$ drift.

- The radial position of the velocity shear layer was determined with high precision ($\sim$ 1 mm).
- A simple model was introduced to judge the error of the poloidal phase velocity estimation introduced by its radial component.
- A radial profile of the inverse of the correlation time of fluctuations $1/\tau_{ac}$ was calculated and compared to the $E_{rad} \times B_{tor}$ shearing rate in order to examine the impact of the velocity shear on the turbulence.
- The shearing rate was found to be of the same values as the $1/\tau_{ac}$ outside the VSL, but about five times higher in the proximity of the VSL.
- A small reduction of the relative level of fluctuatuations at the VSL is observed in the statistical parameters of the U_{fl} and I_{sat} signals.
- It was concluded that the system is in the state of marginal stability outside the VSL, while in the proximity of the VSL, the shear slightly dissipates the turbulent structures.
- The results were published in [16.1-4], [16.1-6], [16.1-7], [16.1-8], [**16.2-17**] and presented in conferences [16.3-10], [16.3-12].

2. **Investigation of the CASTOR SOL by means of 2D matrix of Langmuir probes**

- Magnetic field lines in the edge plasma region of the CASTOR tokamak were mapped by the biasing electrode and the 2 dimensional matrix of Langmuir probes: an alternating voltage was applied to the electrode and the power spectrum for this particular frequency clearly showed the projection of the biasing electrode in the 2D array of probes.
- The safety factor q was established in agreement with a theoretical calculation.
- Toroidal structures were mapped by evaluation of cross-correlations of the tips of the rake probe and the 2D array of probes. The poloidal and radial extents of turbulent structures were established.
- Formation of a convective cell around a biased flux tube was explored. The poloidal phase velocity was evaluated around the convective cell from the data from the 2D array of probes to show the impact of the strong local $E_{rad} \times B_{tor}$ drift.
- The results were published in [16.2-1], [**16.2-2**] and presented in conference [16.3-2].

3. **Analyses of relaxation events in the CASTOR tokamak using deeply immersed biasing electrode**

- It was found that a strong transport barrier is established during certain regimes with improved confinement. The barrier periodically collapses and rises with the frequency of approximately 10 kHz.

- The transport barrier was described in detail by temporal evolution of radial profiles of the floating potential, radial and poloidal electric field and the ion saturation current. The poloidal symmetry of the barrier was demonstrated.
- The flow velocities showed an interplay between the toroidal and the poloidal flow.
- The magnetic activity indicated a significant redistribution of the current density profile deep inside the plasma column.
- The results were published in [16.1-1], [16.1-5], [16.1-8], [16.1-9], [16.2-3], [16.2-6], [**16.2-7**], [16.2-12] and presented in conference [16.3-5].

4. **Study of statistical properties of fluctuations in the plasma boundary region of the TJ-II stellarator**

- Statistical parameters of the fluctuations at the plasma boundary of the TJ-II stellarator were studied in detail in order to clarify what is the role of the natural and the imposed $E_{rad} \times B_{pol}$ shear and the magnetic topology in properties of the statistical parameters.
- The analyses have shown that the mechanism leading to changes in the shape of turbulence in the edge plasma is caused not only by the $E_{rad} \times B_{pol}$ shear, but is also related to the magnetic topology.
- The results were published in [**16.2-11**], and presented in conference [16.3-7].

Part III - Ball-pen probe

In the IPP Prague, a new diagnostic tool called "Ball-pen probe" (BPP) for direct measurements of the plasma potential and electron temperature with high temporal resolution has been developed. Apart of this, the probe enables also an estimation of the diffusion coefficient by means of calculating a decrease of high frequencies inside the BPP shaft. A method for evaluating the diffusion coefficient was developed and published in two journal articles. Radial profiles of the diffusion coefficient for several regimes (different magnetic field) were obtained for the CASTOR tokamak and compared with the Bohm's diffusion derived from the electron temperature profile. Preliminary calculations at the RFX-mod reversed field pinch were performed and a radial profile of the diffusion coefficient was obtained as well. The results were published in [16.1-2], [**16.1-3**], [**16.1-11**], [16.1-12], [16.1-13], [**16.2-4**], [16.2-5], [**16.2-15**], [**16.2-16**] and presented in conferences [16.3-3], [16.3-4], [16.3-8], [16.3-11].

Fusion research is a team work owing to the complexity of the investigated problems. So it was also in my case. Apart from the visits abroad, where I was a guest in experimental campaigns, I had participated in a number of domestic and international campaigns at the CASTOR tokamak. My task was not only to process the data, but

also to take care of the experiment: To connect the diagnostics to the data acquisition system, to run the machine, to solve minor problems with discharge regimes as well as with the probes and to arrange the configuration of experiment according to current needs during the campaigns. This flexibility makes measurements at the CASTOR tokamak very efficient and desirable also for scientists from large facilities abroad. All this work was, of course, possible only with help of the technicians, who were taking care of the vacuum, fabricating the probes and installing them into the diagnostic ports, and of my colleagues, mainly my supervisor, who taught me how to control the machine and who was always helpful in cases of major problems with the discharge.

A new tokamak – COMPASS – was moved and reinstalled at the Institute of Plasma Physics AS CR, v.v.i. in Prague [103]. The COMPASS (COMPact ASSembly), originally working at Culham in Great Britain as COMPASS-C (with circular plasma cross-section in 1989–1991) and as COMPASS-D (with divertor in 1992–2001), was offered to our institute and transferred in autumn 2007. I was participating in reinstallation, namely in development of a new high resolution Thomson scattering diagnostics. The results were published in **[16.2-9]**, [16.2-10], **[16.2-14]** and presented in conferences [16.3-6], [16.3-9].

Finally, a part of my work was devoted to education of new scientists. Tokamak CASTOR is a place where students from Czech universities and from abroad come to gain experience and to collect experimental data for their bachelor, master and PhD theses and where Summer schools in plasma physics take place. I was involved in these activities as well. The results were published in [16.1-7], [16.2-13] and presented in conference [16.3-1]. During the Summer Training Course SUMTRAIC 2004, a conclusion was made which fully reflects my personal attitude to the plasma physics research, as shown in figure 15.1.

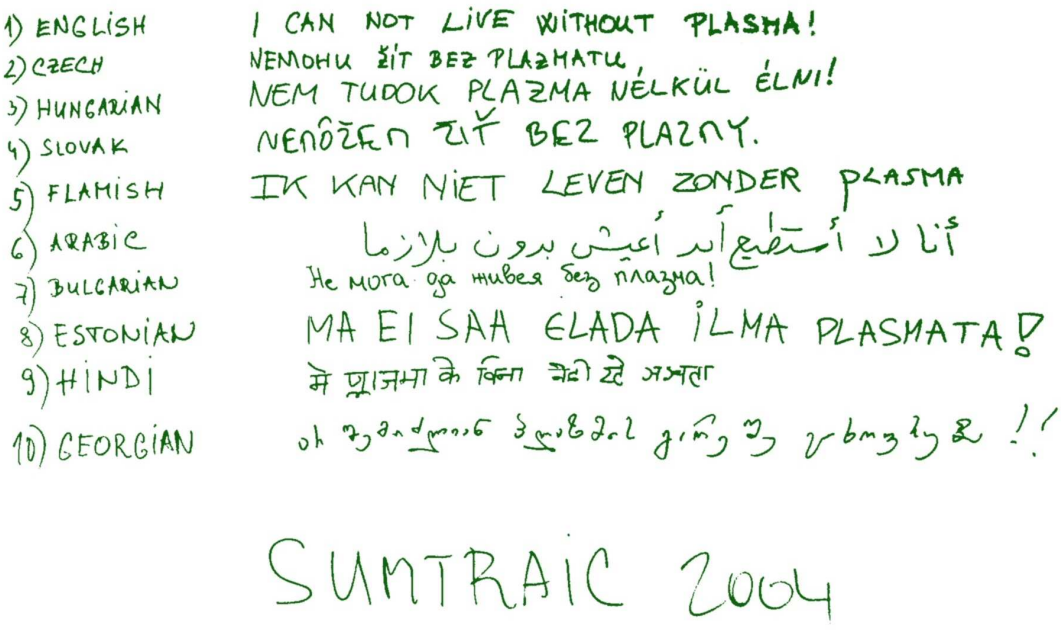

Figure 15.1: *My personal approach to the research of plasma turbulence at the edge of fusion facilities as concluded in the Summer Training Course SUMTRAIC 2004.*

Chapter 16

List of publications

16.1 Publications in scientific journals

1. M. Spolaore, E. Martines, J. Brotankova, J. Stockel, J. Adamek, E. Dufkova, I. Duran, M. Hron, V. Weinzettl, P. Peleman, G. Van Oost, P. Devynck, H. Figueiredo, G. Kirnev, Relaxation phenomena during edge plasma biasing in the CASTOR tokamak, *Czechoslovak Journal of Physics* Vol. **55**, No.12, p. 1597-1606, 2005.

2. R. Schrittwieser, J. Adamek, C. Ionita, J. Stockel, J. Brotankova, E. Martines, G. Popa, C. Costin, L. Van de Peppel, G. Van Oost, Direct measurements of the plasma potential by katsumata-type probes, *Czechoslovak Journal of Physics*, Suppl. B., Vol. **56**, p. 145-150, 2006.

3. J. Brotankova, E. Martines, J. Adamek, J. Stockel, G. Popa, C. Costin, R. Schrittwieser, C. Ionita, G. Van Oost, A probe-based method for measuring the transport coefficient in the tokamak edge region, *Czechoslovak Journal of Physics*, Vol. **56**, No.12, p. 1321-1327, 2006.

4. P. Devynck, J. Brotankova, P. Peleman, M. Spolaore, H. Figueiredo, M. Hron, G. Kirnev, E. Martines, J. Stockel, G. Van Oost, V. Weinzettl, Dynamics of turbulent transport in the scrape-off layer of the CASTOR tokamak, *Physics and Plasmas*, Vol. **13**, No. 10, 102505-102513, 2006.

5. J. Stockel, M. Spolaore, J. Brotankova, J. Horacek, R. Dejarnac, P. Devynck, I. Duran, J.P. Gunn, M. Hron, M. Kocan, E. Martines, R. Panek, P. Peleman, A. Sharma, G. Van Oost, Dynamics of the edge transport barrier at plasma biasing on the CASTOR tokamak, *Voprosy Atomnoj Nauki I Tekhniky* (*Problems of Atomic Science and Technology*: Plasma Physics), No. 6, p. 9-23, 2006.

6. G. Van Oost, V.V. Bulanin, A.J.H. Donne, E.Z. Gusakov, A. Kraemer-Flecken, L.I. Krupnik, A. Melnikov, S. Nanobashvili, P. Peleman, K.A. Razumova, J. Stockel, V. Vershkov, J. Adamek, A.B. Altukov, V.F. Andreev, L.G. Askinazi, I.S. Bondarenko, J. Brotankova, A. Yu. Dnestrovskij, I. Duran, L.G. Eliseev, L.A. Esipov, S.A. Grashin, A.D. Gurchenko, G.M.D. Hogeweij, M. Hron, C. Ionita, S. Jachmich, S.M. Khrebtov, D.V. Kouprienko, S.E. Lysenko, E. Martines, S.V. Perfilov, A.V. Petrov, A.Yu. Popov, D. Reiser, R. Schrittwieser, S. Soldatov, M. Spolaore, A.Yu. Stepanov, G. Telesca, A.O. Urazbaev, G. Verdoolaege, F. Zacek, O. Zimmermann, Multi-machine studies of the role of turbulence and electric fields in the establishment of improved confinement in tokamak plasmas, *Plasma Physics and Controlled Fusion* Vol **49** (5A): A29-A44, 2007.

7. G. Van Oost, M. Berta, J. Brotankova, R. Dejarnac, E. Del Bosco, E. Dufkova, I. Duran, M.P. Gryaznevich, M. Hron, A. Malaquias, G. Mank, P. Peleman, J. Sentkerestiova, J. Stockel, V. Weinzettl, S. Zoletnik, J. Ferrera, A. Fonseca, H. Hegazy, Y. Kuznetsov, A. Ossyannikov, A. Sing, M. Sokholov, A. Talebitaher, Joint experiments on small tokamaks: edge plasma studies on CASTOR, *Nuclear Fusion* Vol. **47** (5): p. 378-386, May 2007.

8. J. Stockel, J. Adamek, P. Balan, O. Bilyk, J. Brotankova, R. Dejarnac, P. Devynck, I. Duran, J.P. Gunn, M. Hron, J. Horacek, C. Ionita, M. Kocan, E. Martines, R. Panek, P. Peleman, R. Schrittwieser, G. Van Oost, F. Zacek, Advanced probes for edge plasma diagnostics on the CASTOR tokamak, *Journal of Physics*: Conference Series **63**, 012001, 2007.

9. P. Peleman, Y. Xu, M. Spolaore, J. Brotankova, P. Devynck, J. Stockel, G. Van Oost, C. Boucher, Highly resolved measurements of periodic radial electric field and associated relaxations in edge biasing experiments, *Journal of Nuclear Materials* Vol. **17** 363-365, p. 638-642, 2007.

10. R. Dejarnac, J.P. Gunn, J. Stockel, J. Adamek, J. Brotankova, C. Ionita, Study of ion sheath expansion and anisotropy of the electron parallel energy distribution in the CASTOR tokamak, *Plasma Physics and Controlled Fusion* Vol. **49**, No. 10, p. 1791-1808, 2007.

11. J. Brotankova, E. Martines, J. Adamek, J. Stockel, G. Popa, C. Costin, R. Schrittwieser, C. Ionita, G. Van Oost, Novel technique for direct measurement of the plasma diffusion coefficient in magnetised plasma, *Contributions to Plasma Physics* Vol. **48**, No. 5-7, p. 418-423, 2008.

12. J. Adamek, M. Kocan, R. Panek, J. P.Gunn, E. Martines, J. Stockel, C. Ionita, G. Popa, C. Costin, J. Brotankova, R. Schrittwieser, G. Van Oost, Simultaneous Measurements of Ion Temperature by Katsumata and Segmented Tunnel Probe, *Contributions to Plasma Physics* Vol. **48**, No. 5-7, p. 395-399, 2008.

13. J. Adamek, V. Rohde, H.W. Muller, A. Herrmann, C. Ionita, R. Schrittwieser, F. Mehlmann, J. Stockel, J. Horacek, J. Brotankova a and ASDEX Upgrade Team, Direct measurements of the plasma potential in ELMy H-mode plasma with ball-pen probes on ASDEX Upgrade tokamak, *Journal of Nuclear Materials*, doi:10.1016/j.jnucmat.2009.01.286, 2009.

16.2 Publications in conference proceedings

1. J. Stockel, P. Devynck, J. Gunn, E. Martines, G. Bonhomme, G. Van Oost, M. Hron, J. Adamek, J. Brotankova, R. Dejarnac, I. Duran, T. Gorler, T. Hansen, R. Panek, P. Stejskal, V. Svoboda, F. Zacek, Formation of convective cells in the scrape-off layer of the CASTOR tokamak, *12th ICPP*, Nice (France), 2004.

2. J. Brotankova, J. Stockel, E. Martines, G. Van Oost, V. Svoboda, T. Gorler, T. Hansen, Fluctuation measurements with 2D matrix of Langmuir probes on the CASTOR tokamak, *32th EPS Plasma Physics Conference*, *EPC*, **29C**, P5.018 (4 pages), Tarragona (Spain), 2005.

3. M. Spolaore, J. Brotankova, P. Peleman, P. Devynck, H. Figueiredo, G. Kirnev, E. Martines, J. Stockel, G. Van Oost, J. Adamek, E. Dufkova, I. Duran, M. Hron, V. Weinzettl, Relaxation phenomena during edge plasma biasing

in the CASTOR tokamak, *32th EPS Plasma Physics Conference*, *EPC*, **29C**, P4.031 (4 pages), Tarragona (Spain), 2005.

4. J. Brotankova, E. Martines, J. Adamek, G. Popa, C. Costin, R. Schrittwieser, C. Ionita, J. Stockel, G. Van Oost, L. van de Peppel, A new probe-based method for measuring the diffusion coefficient in the tokamak edge region, *33rd EPS Plasma Physics Conference*, *EPC*, **30I**, P2.195 (4 pages), Roma (Italy), 2006.

5. R. Schrittwieser, J. Adamek, C. Ionita, J. Stockel, E. Martines, J. Brotankova, G. Popa, C. Costin, G. Van Oost, L. van de Peppel, Direct Measurements of the Plasma Potential by Katsumata-type Probes, *33rd EPS Plasma Physics Conference*, *EPC*, **30I**, P4.196 (4 pages), Roma (Italy), 2006.

6. M. Hron, P. Peleman, M. Spolaore, R. Dejarnac, O. Bilykova, J. Brotankova, J. Sentkerestiova, I. Duran, L. van de Peppel, J. Gunn, J. Stockel, G. Van Oost, J. Horacek, J. Adamek, M. Stepan, Detailed measurements of momentum balance during the periodic collapse of a transport barrier, *33rd EPS Plasma Physics Conference*, *EPC*, **30I**, P4.076 (4 pages), Roma (Italy), 2006.

7. J. Brotankova, J. Stockel, M. Hron, M. Stepan, M. Peterka, J. Horacek, I. Duran, M. Spolaore, P. Peleman, Deep analysis of relaxation events in the CASTOR tokamak using deeply immersed biasing electrode, *WDS'06 Proceedings of Contributed Papers: Part II - Physics of Plasmas and Ionized Media*, Prague, Matfyzpress, p. 127–132, 2006.

8. J. Stockel, J. Brotankova, M. Hron, J. Adamek, I. Duran, G. Van Oost, P. Peleman, J. Gunn, P. Devynck, E. Martines, R. Schrittwieser, M. Kocan, Edge plasma diagnostics in tokamaks, *Proceedings of the Sixth International workshop and school "Towards Fusion Energy – Plasma Physics, Diagnostics, Spin-offs"*, Kudowa Zdroj (Poland), p. 910-935, 2006.

9. J. Brotankova, P. Belsky, R. Barth, H. van der Meiden, V. Weinzettl, P. Bohm, M. Aftanas, New High Resolution Thomson Scattering system for the COMPASS tokamak, *WDS'07 Proceedings of Contributed Papers: Part II - Physics of Plasmas and Ionized Media*, Matfyzpress, p. 218–223, 2007.

10. M. Aftanas, P. Belsky, P. Bohm, V. Weinzettl, J. Brotankova, R. Barth, H. van der Meiden, Exploitation of Avalanche Photodiodes for Thomson Scattering Diagnostics in Tokamaks, *WDS'07 Proceedings of Contributed Papers: Part II - Physics of Plasmas and Ionized Media*, Matfyzpress, p. 224–228, 2007.

11. J. Brotankova, R.O. Orozco, M.A. Pedrosa, C. Hidalgo, E. Sanchez, J. Stockel, Study of the statistical properties of fluctuations in the plasma boundary region of the TJ-II stellarator, *Proceedings of 34th EPS Conference on Plasma Physics* (*Plasma Physics Reports*), P1.086 (4 pages), Warsaw (Poland), 2007.

12. J. Stockel, J. Adamek, J. Brotankova, R. Dejarnac, P. Devynck, I. Duran, J. Gunn, J. Horacek, M. Hron, M. Kocan, E. Martines, P. Peleman, R. Panek,

M. Spolaore, G. Van Oost, Survey of results on plasma biasing in the CASTOR tokamak, *Proceedings of 34th EPS Conference on Plasma Physics* (*Plasma Physics Reports*), P2–031–P2–031, Warsaw (Poland), 2007.

13. M.P. Gryaznevich, G. Van Oost, E. Del Bosco, M. Berta, J. Brotankova, R. Dejarnac, E. Dufkova, I. Duran, M. Hron, J. Zajac, A. Malaquias, G. Mank, P. Peleman, J. Sentkerestiova, J. Stockel, V. Weinzettl, S. Zoletnik, B. Tal, J. Ferrera, A. Fonseca, H. Hegazy, Y. Kuznetsov, L. Ruchko, G.M. Vorobjev, A. Ossyannikov, E. Sukhov, A. Sing, B. Kuteev, A. Melnikov, V. Vershkov, N. Kirneva, G. Kirnev, V. Budaev, M. Sokolov, A. Talebitaher, P. Khorsid, R. Gonzales, I. El Chama Neto, A.E. Kraemer-Flecken, V. Soldatov, A.M. Marques Fonseca, C.R. Gutierrez-Tapia, L.I. Krupnik, Progress on joint experiments on small tokamaks, *Proceedings of 34th EPS Conference on Plasma Physics* (*Plasma Physics Reports*), P1.070 (4 pages), Warsaw (Poland), 2007.

14. J. Brotankova, P. Belsky, R. Barth, H. van der Meiden, V. Weinzettl, P. Bohm, M. Aftanas, Development of New High Resolution Thomson Scattering system for the COMPASS tokamak, *Proceedings of the 13th International Symposium on LASER-AIDED PLASMA DIAGNOSTICS: NIFS-PROC-68*, Takayama (Japan), p. 130–133, 2007.

15. J. Brotankova, J. Adamek, E. Martines, J. Stockel, M. Spolaore, R. Cavazzana, G. Serianni, N. Vianello, M. Zuin, Measurements of plasma potential and electron temperature by Ball-pen probes in RFX-mod, *Problems of Atomic Science and Technology* No. 1, *Series:* Plasma Physics (15), p. 16-18, January 2009.

16. J. Brotankova, J. Stockel, I. Duran, M. Hron, G. Van Oost, Measurement of Sheared Flows at the Plasma Edge of the CASTOR Tokamak, *Proceedings of the 18th IAEA Technical Meeting on Research Using Small Fusion Devices*, submitted for publication.

17. J. Brotankova, J. Stockel, M. Hron, I. Duran, J. Horacek, G. Van Oost, Detailed measurements of poloidal velocity of density and floating potential fluctuations in the edge plasma of the CASTOR tokamak, *WDS'08 Proceedings of Contributed Papers: Part II - Physics of Plasmas and Ionized Media*, Matfyzpress, p. 94-99, 2008.

16.3 Presentations at international conferences

1. Arun K. Sarma, I. Uytdenhouwen, S. Yordanova, E. Dufkova, E. El-demerdash, S. Shalaby, F. Valk, T. Szepesi, M. Sziberth, M. Kocan, M. Tarana, J. Brotankova, **poster** at the SUMTRAIC 2004, *22th Symposium on Plasma Physics and Technology*, Prague (Czech Republic), 2004.

2. J. Brotankova, J. Stockel, E. Martines, G. Van Oost, V. Svoboda, T. Gorler, T. Hansen, Fluctuation measurements with 2D matrix of Langmuir probes on

the CASTOR tokamak, **poster** at the *32th EPS Plasma Physics Conference*, Tarragona (Spain), 27 June – 1 July, 2005.

3. J. Brotankova, E. Martines, J. Adamek, G. Popa, C. Costin, R. Schrittwieser, C. Ionita, J. Stockel, G. Van Oost, L. van de Peppel, A new probe-based method for measuring the diffusion coefficient in the tokamak edge region, **poster** at the *33rd EPS Plasma Physics Conference*, Roma (Italy), June 19–23, 2006.

4. J. Brotankova, E. Martines, J. Adamek, G. Popa, C. Costin, R. Schrittwieser, C. Ionita, J. Stockel, G. Van Oost, L. van de Peppel, A new probe-based method for measuring the diffusion coefficient in the tokamak edge region, **oral contribution** at the *9th wokshop on the Electric Fields, Structures, and Relaxation in Plasmas*, Roma (Italy), June 26–27, 2006.

5. J. Brotankova, M. Spolaore, J. Stockel, P. Peleman, M. Hron, Stepan, Deep analysis of relaxation events on the CASTOR tokamak, **oral contribution** at the *WDS'06*, Prague (Czech Republic), June 6–9, 2006.

6. J. Brotankova, P. Belsky, R. Barth, H. van der Meiden, V. Weinzettl, P. Bohm, M. Aftanas, New High Resolution Thomson Scattering system for the COMPASS tokamak, **oral contribution** at the *WDS'07*, Prague (Czech Republic), June 5–8, 2007.

7. J. Brotankova, R.O. Orozco, M.A. Pedrosa, C. Hidalgo, E. Sanchez, J. Stockel, Study of the statistical properties of fluctuations in the plasma boundary region of the TJ-II stellarator, **poster** at the *34th EPS Plasma Physics Conference*, Warsaw (Poland), July 2-6, 2007.

8. J. Brotankova, E. Martines, J. Adamek, J. Stockel, G. Popa, C. Costin, R. Schrittwieser, C. Ionita, G. Van Oost, Novel technique for direct measurement of the plasma diffusion coefficient in magnetised plasma, **oral contribution** at the *7th International Workshop on Electrical Probes in Magnetized Plasmas*, Prague (Czech Republic), July 22–25, 2007.

9. J. Brotankova, P. Belsky, R. Barth, H. van der Meiden, V. Weinzettl, P. Bohm, M. Aftanas, Development of New High Resolution Thomson Scattering system for the COMPASS tokamak, **oral contribution** at the *13th International Symposium on Laiser-Aided Plasma Diagnostics*, Takayama (Japan), September 18–21, 2007.

10. J. Brotankova, J. Stockel, M. Hron, I. Duran, J. Horacek, G. Van Oost, Detailed measurements of poloidal velocity of density and floating potential fluctuations in the edge plasma of the CASTOR tokamak, **oral contribution** at the *WDS'08*, Prague (Czech Republic), June 3–6, 2008.

11. Presented by J. Stockel: J. Brotankova, J. Adamek, E. Martines, J. Stockel, M. Spolaore, R. Cavazzana, G. Serianni, N. Vianello, M. Zuin, Measurements of plasma potential and electron temperature by Ball-pen probes in RFX-mod, **oral contribution** at the *3-rd International Workshop on the Role of*

Electric Fields in Plasma Confinement in Stellarators and Tokamaks, Alushta (Crimea, Ukraine), September 22–27, 2008.

12. Presented by J. Stockel: J. Brotankova, J. Stockel, I. Duran, M. Hron, G. Van Oost, Measurement of Sheared Flows at the Plasma Edge of the CASTOR Tokamak, **poster** at the *18th IAEA Technical Meeting on Research Using Small Fusion Devices*, Alushta (Crimea, Ukraine), September 25–27, 2008.

16.4 Stays abroad

- September 2003 (2 weeks): 5th Carolus Magnus Summer School on Plasma and Fusion Energy Physics, Bruxelles, Belgium.
- May, June 2005 (6 weeks): reversal field pinch RFX-mod, Consorzio RFX, Padova, Italy.
- November 2006 (5 weeks): stellarator TJ-II, CIEMAT, Madrid, Spain.
- March 2007 (1 week): FOM Institute of Plasma Physics Rijnhuizen, Netherlands.
- October 2007 (2 weeks): reversal field pinch RFX-mod, Consorzio RFX, Padova, Italy.

APPENDIX

A-1 Toroidal magnetic field

In the frame of my thesis, I have performed a detailed analyses of the generation of the toroidal magnetic field B_{tor}.

The toroidal magnetic field (B_{tor}) is induced via 28 poloidal field coils each with 11 turns ($L_{tot} = 2.8$ mH as shown in following) connected in series to the capacitor bank ($C = 0.229$ F). Capacitors can be charged to voltage U up to 2000 V. In the standard regime, $U = 1084$ V which generates $B_{tor} = 1$ T. The parameters, however, allow to operate with B_{tor} up to 1.2 T. Current flowing through the coils is up to 20 kA. The maximum of B_{tor} is at the axis of the torus and it decreases with the major radius as $1/R$, as illustrated in figure 16.1 by the blue line. The part of the chamber close to the main axis is thus called High Field Side (HFS), while the part farther is indicated as Low Field Side (LFS).

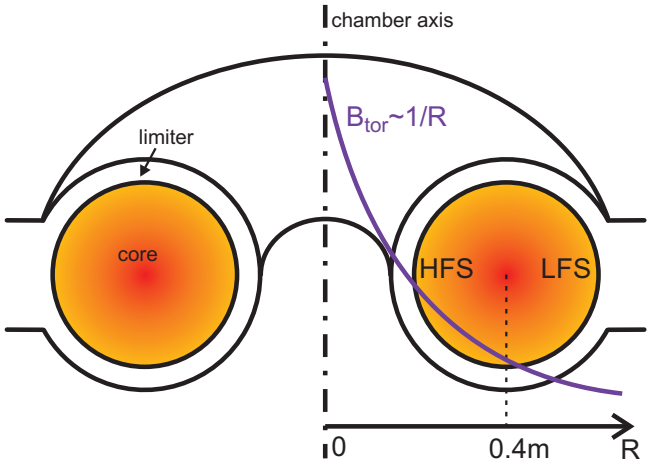

Figure 16.1: *The* $1/R$ *decrease of* B_{tor}.

In the standard regime ($B_{tor} = 1$ T), the total electrostatic energy stored in the capacitor bank is $W_C = 1/2\ CU^2 = 134.5$ kJ. Total energy of the magnetic field (for $B_{tor} = 1$ T) inside of the LCFC (Last Closed Flux Surface) is $W_{B_{tor}} = (V/2\mu_0)B_{tor}^2 = 44$ kJ, where $V = 0.11\ m^3$ is a volume of the region of the vacuum vessel. That means that only about 33 % of energy stored in the B_{tor} capacitor banks are efectively used for particle confinement.

The B_{tor} is measured with a single coil (active area $S = 0.0283$ m^2) placed in the

shadow of the limiter at $r = 95$ mm, as depicted in figure 16.2. The output voltage of the coil is digitized by 12 bit A/D converter (sb2) usually with the sampling rate of 100 μs/sample, stored in the PC oriented database, and further numerically processed.

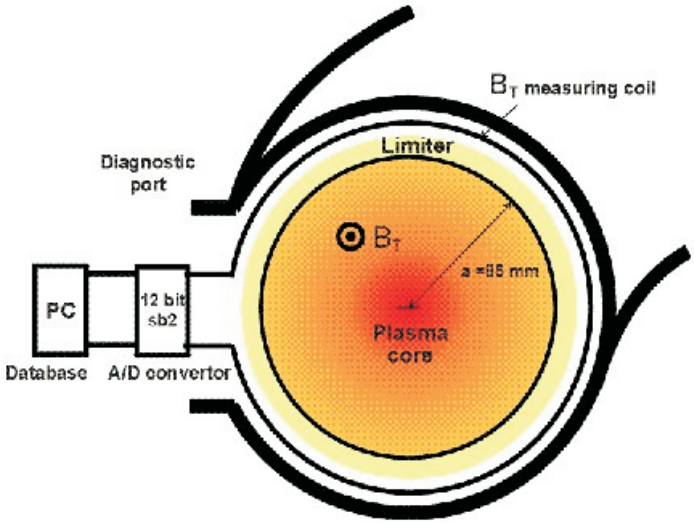

Figure 16.2: *Position of the B_{tor} coil depicted in a poloidal cross-section of the CASTOR tokamak.*

For the voltage in the coil, we can write

$$V(t) = -\frac{\mathrm{d}\Phi}{\mathrm{dt}} = -S \cdot \frac{\mathrm{d}B}{\mathrm{dt}}, \tag{A-1}$$

where $\Phi = NBS$ is magnetic flux through the coil's cross-section, $N = 1$ is number of turns of the coil and S is its active area. Solution of this simple differential equation is:

$$B(t) = -\frac{1}{S}\int_0^t V(t')dt'. \tag{A-2}$$

Generation of B_{tor} based on RLC oscillating circuit causes sinusoidal character of B_{tor}. C and L_{tot} limits the half period of B_{tor} evolution to

$$\tau_{1/2} = \pi\sqrt{L_{tot}C} \cong 83 \text{ ms} \tag{A-3}$$

according to measurements. RLC oscillating circuit used for creation of B_{tor} consists of the poloidally oriented coils and the B_{tor} capacitor bank. The resistance is equal to the resistance of the coils and the wires. Generally, a following formula can be written for a B_{tor} in a toroid:

$$B_{tor} = \frac{\mu_0}{2\pi}\frac{NI}{r} \tag{A-4}$$

where N is the number of turns of the coil, r is the minor radius and I is the current through the RLC oscillating circuit:

$$I = CU\frac{\beta^2 + \omega_0^2}{\omega_0}e^{-\beta t}\sin\omega_0 t \tag{A-5}$$

where

$$\beta = \frac{1}{2}\frac{R}{L_{tot}} \qquad \text{and} \qquad \omega_0 = \sqrt{\frac{1}{\mathrm{L_{tot}C}} - \frac{1}{4}\frac{\mathrm{R^2}}{\mathrm{L_{tot}^2}}}. \tag{A-6}$$

Substituting (A-5) into (A-4), we obtain

$$B_{tor} = \frac{\mu_0}{2\pi}\frac{N}{r} \cdot CU\frac{\beta^2 + \omega_0^2}{\omega_0} e^{-\beta t} \sin \omega_0 t. \tag{A-7}$$

If we define

$$\alpha_1 = \frac{\mu_0}{2\pi}\frac{N}{r} \cdot CU\frac{\beta^2 + \omega_0^2}{\omega_0} \tag{A-8}$$

$$\alpha_2 = \beta \tag{A-9}$$

$$\alpha_3 = \omega_0, \tag{A-10}$$

we can re-write formula (A-7) as

$$B_{tor} = \alpha_1 \cdot e^{-\alpha_2 t} \sin(\alpha_3 t). \tag{A-11}$$

This formula was fitted to experimental data of B_{tor} with free parameters α_1, α_2, α_3. We obtained the values $\alpha_1 = 1.622$, $\alpha_2 = 10.922$, $\alpha_3 = 37.914$. Final formula for the time evolution of B_{tor} is

$$B_{tor} = 1.622 \cdot e^{-10.922 \cdot t} \sin 37.914 \cdot t. \tag{A-12}$$

From formulae (A-8), (A-9), and (A-10) we obtained the values $R = 0.061\ \Omega$, $C = 0.229$ F, $U_0 = 1084$ V.

A-2 Integrals of n_e and T_e

Central electron density, averaged electron density

The electron density n_e is measured by an interferometer as one of the main plasma parameters, shown in figure 3.3. It is a chord averaged density, normalized to 1 m^3. For some calculations, we need the central plasma electron density $n_e(0)$ or the volume averaged electron density $\langle n_e \rangle$.

Central electron density

The measured electron density $n_{e\ meas}$ is a line averaged value:

$$n_{e\ meas} = \int_{-a}^{a} n_e(r)dr \cdot \frac{1}{2a} \tag{A-13}$$

where $2a$ is the chord length. Assuming a parabolic density profile

$$n_e(r) = n_e(0)\left(1 - \frac{r^2}{a^2}\right), \tag{A-14}$$

we can write

$$n_{e\ meas} = n_e(0) \int_{-a}^{a} \left(1 - \frac{r^2}{a^2}\right) dr \cdot \frac{1}{2a}. \tag{A-15}$$

The integral is equal to $\frac{4}{3}a$, thus the central density can be easily calculated as

$$n_e(0) = \frac{3}{2} n_{e\ meas}. \tag{A-16}$$

Volume averaged electron density

The volume averaged electron density can be derived from

$$\langle n_e \rangle = \int_{0}^{a} n_e(r) \cdot 2\pi r dr \cdot \frac{1}{\pi a^2} \tag{A-17}$$

where πa^2 is the surface of the poloidal cross-section (since we integrate over the cross-section). Again, assuming a parabolic temperature profile (equation (A-14)), we can write

$$\langle n_e \rangle = n_e(0) \int_{0}^{a} \left(1 - \frac{r^2}{a^2}\right) 2\pi r dr \cdot \frac{1}{\pi a^2}. \tag{A-18}$$

The integral is equal to $2\pi \cdot \frac{1}{4}a^2$, thus the volume averaged electron density is from (A-18) and (A-16)

$$\langle n_e \rangle = \frac{1}{2} n_e(0) = \frac{3}{4} n_{e\ meas}. \tag{A-19}$$

Volume averaged electron temperature

The volume averaged electron temperature can be derived in the same manner as the density from

$$\langle T_e \rangle = \int_0^a T_e(r) 2\pi r dr \cdot \frac{1}{\pi a^2} \tag{A-20}$$

where πa^2 is the surface of the poloidal plasma cross-section. Assuming the profile

$$T_e(r) = T_e(0) \left(1 - \frac{r^2}{a^2}\right)^{\alpha} \tag{A-21}$$

where $\alpha = 2$, the averaged electron temperature can be written as

$$\langle T_e \rangle = T_e(0) \int_0^a \left(1 - \frac{r^2}{a^2}\right)^2 2\pi r dr \cdot \frac{1}{\pi a^2}. \tag{A-22}$$

The integral is equal to $2\pi \cdot \frac{a^2}{6}$, thus the volume averaged electron temperature can be easily calculated as

$$\langle T_e \rangle = \frac{1}{3} T_e(0). \tag{A-23}$$

Average of the product of electron temperature and density

The average of electron temperature and density can be written as

$$\langle T_e(r) n_e(r) \rangle = \int_0^a T_e(r) \cdot n_e(r) \cdot 2\pi r dr \cdot \frac{1}{\pi a^2}. \tag{A-24}$$

Assuming the profiles of T_e as (A-21) and n_e as (A-14), we can write

$$\langle T_e(r) n_e(r) \rangle = T_e(0) \cdot n_e(0) \int_0^a \left(1 - \frac{r^2}{a^2}\right)^2 \cdot \left(1 - \frac{r^2}{a^2}\right) 2\pi r dr \cdot \frac{1}{\pi a^2}. \tag{A-25}$$

After integration (the integral is $2\pi \cdot \frac{a^2}{8}$):

$$\langle T_e(r) n_e(r) \rangle = \frac{1}{4} T_e(0) \cdot n_e(0). \tag{A-26}$$

Bibliography

[1] F. Francis Chen, Introduction fo Plasma Physics, Plenum Press, New York (1974).

[2] H. Prinzler, P. Heymann, J. Stockel, J. Badalec, F. Zacek, K. Jakubka, V. Kopecky, Investigation of the start up phase in the TM 1 tokamak, *Czechoslovak Journal of Physics*, Vol. **B34**, p. 665–679 (1984).

[3] M. Valovic, J. Badalec, K. Jakubka, V. Kopecky, J. Stockel, F. Zacek, A start-up discharge phase in a CASTOR tokamak, *Proceedings of the 12th EPS Conferencce on Plasma Physics*, Budapest, (September 1985).

[4] I. Duran, Fluktuace magnetického pole na tokamku CASTOR (Fluctuations of the magnetic field of the CASTOR tokamak), *PhD Thesis*, KEVF, MFF UK, Prague (2003).

[5] M. Valovic, Control of plasma position in the CASTOR tokamak, *Czechoslovak Journal of Physics*, Vol. **B39**, p. 1111–1119 (1989).

[6] M. Valovic, Magnetic diagnostics on the CASTOR tokamak, *Czechoslovak Journal of Physics*, Vol. **B38**, p. 65-71 (1988).

[7] V. Weinzettl, Prostorové a časové chování lehkých nečistot ve vysokoteplotním plazmatu tokamaku CASTOR (Spatial and temporal behaviuor of light impurities in a high-temperature plasma of the CASTOR tokamak), *PhD Thesis*, FNSPE CTU, Prague (2005).

[8] A. Raicu, Th. Ionescu-Bujor, A. Pantea, V. Valeanu, J. Badalec, K. Jakubka, Vl. Kopecky, J. Stockel, M. Valovic, F. Zacek, The thermal ionization phase during the plasma formation in TM-1-MH tokamak, *Czechoslovak Journal of Physics*, Vol. **B 37**, p. 850-861 (1987).

[9] I. Duran, Runaway electrons in tokamaks, *rešeršní práce*, KFE CVUT, Prague (1995).

[10] R. Dejarnac, J.P. Gunn, J. Stockel, J. Adamek, J. Brotankova, C. Ionita, Study of ion sheath expansion and anisotropy of the electron parallel energy distribution in the CASTOR tokamak, *Plasma Physics and Controlled Fusion* **49**, 1791-1808 (2007).

[11] J. Brotankova, V. Weinzettl, H-alpha line measurements and Te profile estimation, *Czechoslovak Journal of Physics*, Suppl. S3, Vol. **50**, p. 71–74 (2000).

[12] K. S. Dyabilin, J. Badalec, A. A. Borschegovski, J. Datlov, K. Jakubka, V. Kopecky, A. A. Korotkov, J. Stockel, M. Valovic, F. Zacek, Global energy balance and density limit on CASTOR tokamak, *Czechoslovak Journal of Physics*, Vol. **B 37**, p. 713–724 (1987).

[13] M. Hron, Transport částic v okrajovém plazmatu na tokamaku Castor (Particles transport in the edge plasma of the tokamak CASTOR), *Diploma Thesis*, KFE, FJFI CVUT, Prague (1996).

[14] J. Brotankova, K. Jakubka, L. Kryska, J. Stockel, F. Zacek, Measurement of energy confinement in CASTOR tokamak regimes with edge plasma polarization, *Czechoslovak Journal of Physics*, Suppl. S3, Vol. **50**, p. 75–80 (2000).

[15] E. Martines, M. Hron, J. Stockel, Coherent structures in the edge turbulence of the CASTOR tokamak, *Plasma Physics and Controlled Fusion* **44**, p. 351-359 (2002).

[16] J. Stockel, P. Devynck, J. Gunn, E. Martines, G. Bonhomme, G. Van Oost, M. Hron, I. Duran, R. Panek, P. Stejskal, J. Adamek, Edge plasma physics and relevant diagnostics on the CASTOR tokamak, *Schriften des Forschungszentrums Jlich*, Vol. **3**, p. 1-6 (2004).

[17] I. Duran, O. Hronova, J. Stockel, J. Sentkerestiova, J. Havlicek, Magnetic measurements using array of integrated Hall sensors on the CASTOR tokamak, *Review of Scientific Instruments* **79**, 10F123 (2008).

[18] J. Stockel, P. Devynck, G. Bonhomme, E. Martines, G. Van Oost, M. Hron, I. Voitsekhovitch, J. Adamek, F. Doveil, I. Duran, J. Gunn, P. Stejskal, V. Weinzettl, Poloidal structure of the scrape off layer turbulence in the CASTOR tokamak, *Proceedings of the 30th EPS Conference*, ECA Vol. **27A**, P-1.179 (2003).

[19] J. Adamek, J. Stockel, M. Hron, J. Ryszawy, M. Tichy, R. Schrittwieser, C. Ionita, P. Balan, E. Martines, G. Van Oost, A novel approach to direct measurement of the plasma potential *Czechoslovak Journal of Physics* **54**, C95–C99 (2004).

[20] J. Adamek, J. Stockel, I. Duran, M. Hron, R. Panek, M. Tichy, R. Schrittwieser, C. Ionita, P. Balan, E. Martines, G. Van Oost, Comparative measurements of the plasma potential with the ball-pen and emissive probes on the CASTOR tokamak, *Czechoslovak Journal of Physics* **55**, 235-242 (2005).

[21] R. Schrittwieser, J. Adamek, J. Stockel, J. Brotankova, E. Martines, G. Popa, C. Costin, L. van de Peppel, G. Van Oost, Direct measurements of the plasma potential by Katsumata–type probes, *Czechoslovak Journal of Physics* **56**, Suppl. B (145–150) (2006).

[22] J. Gunn, J. Stockel, J. Adamek, I. Duran, J. Horacek, M. Hron, K. Jakubka, L. Kryska, F. Zacek, G. Van Oost, Direct measurements of $E \times B$ flow and its impact on edge turbulence in the CASTOR tokamak using an optimized Gundestrup probe, *Czechoslovak Journal of Physics* **51**, p. 1001-1010 (2001).

[23] J. Adamek, M. Kocan, R. Panek, J.P. Gunn, E. Martines, J. Stockel, C. Ionita, G. Popa, C. Costin, J. Brotankova, R. Schrittwieser, G. Van Oost, Simultaneous Measurements of Ion Temperature by Katsumata and Segmented Tunnel Probe, *Contributions to Plasma Physics* **48**, No. 5-7, p. 395-399 (2008).

[24] P. Balan, J. Adamek, O. Barina, P. DeBeule, I. Duran, J.P. Gunn, M. Hron, C. Ionita, E. Martines, R. Panek, R. Schrittwieser, J. Stockel, G. Van Den Berge, G. Van Oost, T. Van Rompuy, Simultaneous Measurement of Electron and Ion Temperatures with a New Kind of Langmuir Probe, *Proceedings of the 30th EPS Conference*, ECA Vol. **27A**, P-1.84 (2003).

[25] Peter C. Stangeby, The plasma boundary of magnetic fusion devices, *Plasma Physics Series*, 1999.

[26] M. Berta, B. Tal, A. Bencze, S. Zoletnik, J. Stockel, M. Hron, R. Dejarnac, J. Zajac, The spatial structure of flows, Reynolds stress and turbulence in the CASTOR tokamak, *33rd EPS Conference*, Rome, ECA Vol.**30I**, P-4.074 (2006).

[27] I. Duran, O. Hronova, J. Stockel, J. Sentkerestiova, J. Havlicek, Magnetic measurements using array of integrated Hall sensors on the CASTOR tokamak, *Review of Scientific Instruments* **79**, 1 (2008).

[28] J. Stockel, P. Devynck, J. Gunn, E. Martines, G. Bonhomme, G. Van Oost, M. Hron, J. Adamek, J. Brotankova, R. Dejarnac, I. Duran, T. Gorler, T. Hansen, R. Panek, P. Stejskal, V. Svoboda, F. Zacek, Formation of convective cells in the scrape-off layer of the CASTOR tokamak, 12th International Congress on Plasma Physics, Nice (2004).

[29] M. Kocan, R. Panek, J. Stockel, M. Hron, J.P. Gunn, R. Dejarnac, Ion temperature measurements in the tokamak scrape-off layer, *Journal of Nuclear Materials*, 363-365, p. 1436-1440 (2007).

[30] J. Stockel, J. Adamek, P. Balan, O. Bilyk, J. Brotankova, R. Dejarnac, P. Devynck, I. Duran, J. P. Gunn, M. Hron, J. Horacek, C. Ionita, M. Kocan, E. Martines, R. Panek, P. Peleman, R. Schrittwieser, G. Van Oost, F. Zacek, Advanced probes for edge plasma diagnostics on the CASTOR tokamak, *Journal of Physics*, Conference Series, **63** No. 0 (2006).

[31] J. Adamek, M. Kocan, R. Panek, J.P. Gunn, E. Martines, J. Stockel, C. Ionita, G. Popa, C. Costin, J. Brotankova, R. Schrittwieser, G. Van Oost, Simultaneous Measurements of Ion Temperature by Segmented Tunnel and Katsumata Probe, *Contributions to Plasma Physics* **48**, No. 5-7, p. 395-399 (2008).

[32] M. Kocan, J.P. Gunn, J.-Y. Pascal, G. Bonhomme, C. Fenzi, E. Gauthier, J.-L. Segui, Edge ion-to-electron temperature ratio in the Tore Supra tokamak, *Plasma Physics and Controlled Fusion*, **50**, 125009 (10pp) (2008).

[33] J. Brotankova, E. Martines, J. Adamek, J. Stockel, G. Popa, C. Costin, R. Schrittwieser, C. Ionita, G. Van Oost, A probe-based method for measuring the transport coefficient in the tokamak edge region, *Czechoslovak Journal of Physics*, Vol. **56** (12), No.12, p. 1321–1327 (2006).

[34] J. Brotankova, E. Martines, J. Adamek, J. Stockel, G. Popa, C. Costin, R. Schrittwieser, C. Ionita, G. Van Oost, Novel technique for direct measurement of the plasma diffusion coefficient in magnetised plasma, *Contributions to Plasma Physics* **48**, No. 5-7, p. 418–423 (2008).

[35] M. Hron, Turbulence plazmatu na tokamaku Castor (Plasma turbulence in the CASTOR tokamak), *PhD Thesis*, KEVF, MFF UK, Prague (2002).

[36] P.C. Stangeby, A tutorial on some basic aspects of divertor physics, *Plasma Physics and Controlled Fusion*, **42**, B271-B291 (2000).

[37] J. Stockel, E. Martines, G. Van Oost, V. Svoboda, T. Gorler, T. Hansen, Fluctuation measurements with 2D matrix of Langmuir probes on the CASTOR tokamak, *Proceedings of the 32nd EPS Conference*, EPC Vol. **29C**, P-5.018 (2005).

[38] J. Brotankova, J. Stockel, M. Hron, I. Duran, G. Van Oost, Measurement of Sheared Flows at the Plasma Edge of the CASTOR Tokamak, *Proceedings of the 18th IAEA Technical Meeting on Research Using Small Fusion Devices*, submitted for publication.

[39] J. A. Wesson *et al.*: Tokamaks, Clarendon Press, Oxford, 3rd edition, 2004.

[40] G. Van Oost, M. Berta, J. Brotankova, R. Dejarnac, E. Del Bosco, E. Dufkova, I. Duran, M.P. Gryaznevich, J. Horacek, M. Hron, A. Malaquias, G. Mank, P. Peleman, J. Sentkerestiova, J. Stockel, V. Weinzettl, S. Zoletnik, B. Tal, J. Ferrera, A. Fonseca, H. Hegazy, Y. Kuznetsov, A. Ossyannikov, A. Singh, M. Sokholov, A. Talebitaher, Joint experiments on small tokamaks: edge plasma studies on CASTOR, *Nuclear fusion* **47** (5): 378-386 (May 2007).

[41] J. Stockel, J. Adamek, P. Balan, O. Bilyk, J. Brotankova, R. Dejarnac, P. Devynck, I. Duran, J.P. Gunn, M. Hron, J. Horacek, C. Ionita, M. Kocan, E. Martines, R. Panek, P. Peleman, R. Schrittwieser, G. Van Oost, F. Zacek, Advanced probes for edge plasma diagnostics on the CASTOR tokamak, *Journal of Physics, conference series*, **63**, 012001 (2007).

[42] R. Dejarnac, J.P. Gunn, J. Stockel, J. Adamek, J. Brotankova, C. Ionita, Study of ion sheath expansion and anisotropy of the electron parallel energy distribution in the CASTOR tokamak, *Plasma Physics and Controlled Fusion* **49** 1791-1808 (2007).

[43] J. Schirmer, G.D. Conway, H. Zohm, W. Suttrop and the ASDEX Upgrade Team, The radial electric field and its associated shear in the ASDEX Upgrade tokamak, *Nuclear Fusion* Vol. **46**, S780S791 (2006).

[44] L. Krlin, J. Stockel, V. Svoboda, Stochastic ($E \times B$) diffusion of ions in a spatially periodical potential field, *Plasma Physics and Controlled Fusion*, Vol. **41**, No. 3, p. 339–353 (1999).

[45] J. Stockel, J. Badalec, I. Duran, M. Hron, J. Horacek, K. Jakubka, L. Kryska, J. Petrzilka, F. Zacek, M.V.P. Heller, Z.A. Brazilio, I.L. Caldas, Magnetic and electrostatic fluctuations in the CASTOR tokamak, Plasma Physics and Controlled Fusion **41** (1999) A577-A585.

[46] G. Vayakis, Anomalous Transport in the Tokamak Edge, *PhD thesis*, Department of Engineering Science, Oxford, (1991).

[47] Bendat, Piersol: Random Data: Analysis and Measurements Procedures, Wiley and Sons, p. 148 (2000).

[48] Ch.P. Ritz, D. Roger, S. Bengtson, S.J. Levinson, E.J. Powers, Turbulent structure in the edge plasma of the TEXT tokamak, *Physics of Fluids* Vol. **27**, No. 12, p. 2956–2959 (December 1984).

[49] G.Van Oost, J. Stockel, M. Hron, P. Devynck, K. Dyabilin, J.P. Gunn, J. Horacek, E. Martines, M. Tendler, Potential structures and flow measurements with separatrix biasing in the CASTOR tokamak, *J. Plasma Fusion Res. SERIES* Vol. **4**, p 29-35 (2001).

[50] P. Devynck, J. Brotankova, P. Peleman, M. Spolaore, H. Figueiredo, M. Hron, G. Kirnev, E. Martines, J. Stockel, G. Van Oost, V. Weinzettl, Dynamics of turbulent transport in the scrape-off layer of the CASTOR tokamak, *Physics of Plasmas*, **13** (10), 102505-102513 (2006).

[51] C. Hidalgo, B. Goncalves, M.A. Pedrosa, C. Silva, R. Balbin, M. Hron, A. Loarte, K. Erents, G.F. Matthews, R. Pitts, Experimental evidence of fluctuations and flows near marginal stability and dynamical interplay between gradients and transport in the JET plasma boundary region, *Journal of Nuclear Materials*, 313316 (2003) 863867.

[52] O.E. Garcia, N.H. Bian, V. Naulin, A.H. Nielsen, J. Juul Rasmussen, Two-dimensional convection and interchange motions in fluids and magnetized plasmas, *Physica Scripta* T122, p. 104-124 (2006).

[53] J. Horacek, A.H. Nielsen, O.E. Garcia, R.A. Pitts, Spatio-temporal correlations in edge tokamak plasma fluctuations in both experiment and modelling, Abstract in the *Bulleting of APS* **52**, DPP07-2007-000077, APS Meeting, Florida, (November 2007).

[54] M. Hron, E. Martines, P. Devynck, G. Bonhomme, E. Gravier, J. Adamek, F. Doveil, I. Voitsekchovich, J. Stockel, A. Azeroul, I. Duran, G. Van Oost, F. Zacek, Probe array diagnostics for spatially resolved fluctuation measurements, *Proceedings of the 29th EPS conference*, Vol. **C**, P-5.043 (2002).

[55] J. Stockel, P. Devynck, J. Gunn, E. Martines, G. Bonhomme, I. Voitsekhovitch, G. Van Oost, M. Hron, I. Duran, P. Stejskal, J. Adamek, V. Weinzettl, F. Zacek, Formation of convective cells during scrape-off layer biasing in the CASTOR tokamak, *Plasma Physics Controlled Fusion*, **47** No. 4, p. 635-643 (April 2005).

[56] E. Martines, M. Hron and J. Stockel, Coherent structures in the edge turbulence of the CASTOR tokamak, *Plasma Physics and Controlled Fusion* **44** No. 3, p. 351-359 (March 2002).

[57] P. Devynck, G. Bonhomme, E. Martines, J. Stockel, G. Van Oost, I. Voitsekhovitch, J. Adamek, A. Azeroual, F. Doveil, I. Duran, E. Gravier, J. Gunn, M. Hron, Spatially resolved characterization of electrostatic fluctuations in the scrape-off layer of the CASTOR tokamak, *Plasma Physics and Controlled Fusion*, **47**, No. 2, p. 269-280 (2005).

[58] J.W. Connor, R.J. Hastie, H.R. Wilson Connor, R. L. Miller, Magnetohydrodynamic stability of tokamak edge plasmas, *Physics of Plasmas*, Vol. **5**, No. 7, p. 2687 (1998).

[59] J. Stockel, M. Spolaore, P. Peleman, J. Brotankova, J. Horacek, R. Dejarnac, P. Devynck, I. Duran, J.P. Gunn, M. Hron, M. Kocan, E. Martines, R. Panek, A. Sharma, G. Van Oost, Dynamics of the edge transport barrier at plasma biasing on the CASTOR tokamak, *Problems of Atomic Science and Technology*, Vol. **12**, No. 6, p. 19-23 (2006).

[60] P. Peleman, S. Jachmich, M. Van Schoor, G. Van Oost, W. Knaepen, C. Boucher, Comparative Study of Flat and Round Collectors Using a Validated 1D Fluid Probe Model, *Contributions to Plasma Physics* **46**, No. 5-6, p. 422–426 (2006).

[61] P. Peleman, Y. Xu, M. Spolaore, J. Brotankova, P. Devynck, J. Stockel, G. Van Oost, C. Boucher, Highly resolved measurements of periodic radial electric field and associated relaxations in edge biasing experiments, *Book of Abstracts, Hefei, Anhui*, 314/ P3-23 (2006).

[62] S.J. Zweben, J.A. Boedo, O. Grulke, C. Hidalgo, B. LaBombard, R.J. Maqueda, P. Scarin, J.L. Terry, Edge turbulence measurements in toroidal fusion devices, *Plasma Physics and Controlled Fusion* **49**, S1-S23 (2007).

[63] E. Sanchez, C. Hidalgo, D. Lopez-Bruna, I. Garcia-Cortes, R. Balbin, M.A. Pedrosa, B. van Milligen, C. Riccardi, G. Chiodini, J. Bleuel, M. Endler, B.A. Carreras, D.E. Newman, Statistical characterization of fluctuation wave forms in the boundary region of fusion and nonfusion plasmas, *Physics of Plasma*, Vol. **7**, No. 5. (2000).

[64] O.E. Garcia, J. Horacek, R.A. Pitts, A.H. Nielsen, W. Fundamenski, V. Naulin, J. Juul Rasmussen, Fluctuations and transport in the TCV scrape-off layer, *Nuclear Fusion* **47** p. 667-676 (2007).

[65] O.E. Garcia, Collective motions in non-uniformly magnetized plasmas, *European Journal of Physics* **24**, p. 331–339 (2003).

[66] R.O. Orozco, E. Faleiro, C. Hidalgo, M.A. Pedrosa, C. Silva, E. Sanchez, J.M. Gomez, E. Calderon, On the influence of ExB sheared flows in the statistical properties of turbulence in the plasma boundary of the TJ-II stellarator, *Proceedings of the 32nd EPS conference*, Vol. **29C**, P-5.031 (2005).

[67] C. Alejaldre, J. Alonso, L. Almoguera, E. Ascasibar, A. Baciero, R. Balbin, M. Blaumoser, J. Botija, B. Branas, E. de la Cal, A. Cappa, R. Carrasco, F. Castejon, J.R. Cepero, C. Cremy, J. Doncel, C. Dulya, T. Estrada, A. Fernandez, M. Frances, C. Fuentes, A. Garcia, I. Garcia-Cortes, J. Guasp, J. Herranz, C. Hidalgo, J.A. Jimenez, I. Kirpitchev, V. Krivenski, I. Labrador, F. Lapayese, K. Likin, M. Liniers, A. Lopez-Fraguas, A. Lopez-Sanchez, E. de la Luna, R. Martin, A. Martinez, L. Martinez-Laso, M. Medrano, P. Mendez, K. McCarthy, F. Medina, B. van Milligen, M. Ochando, L. Pacios, I. Pastor, M.A. Pedrosa, A. de la Pena, A. Portas, J. Qin, L. Rodriguez-Rodrigo, A. Salas, E. Sanchez, J. Sanchez, F. Tabares, D. Tafalla, V. Tribaldos, J. Vega, B. Zurro, First plasmas in the TJ-II Flexible Heliac, *Plasma Physics and Controlled Fusion* **41**, A539 (1999).

[68] E. Ascasibar, C. Alejaldre, J. Alonso, L. Almoguera, A. Baciero, R. Balbin, M. Blaumoser, J. Botija, B. Branas, E. de la Cal, A. Cappa, J. Castellano, R. Carrasco, F. Castejon, J.R. Cepero, C. Cremy, J. Doncel, S. Eguilior, T. Estrada, A. Fernandez, C. Fuentes, A. Garcia, I. Garcia-Cortes, J. Guasp, J. Herranz, C. Hidalgo, J.A. Jimenez, I. Kirpitchev, V. Krivenski, I. Labrador, F. Lapayese, K. Likin, M. Linier, A. Lopez-Fraguas, A. Lopez-Sanchez, E. de la Luna, R. Martin, L. Martinez-Laso, M. Medrano, P. Mendez, K.J. McCarthy, F. Medina, B. van Milligen, M. Ochando, L. Pacios, I. Pastor, M.A. Pedrosa, A. de la Pena, A. Portas, J. Qin, L. Rodriguez-Rodrigo, J. Romero, A. Salas, E. Sanchez, J. Sanchez, F. Tabares, D. Tafalla, V. Tribaldos, J. Vega, B. Zurro, Overview of TJ-II flexible heliac results, *Fusion Engineering and Design* 56-57, 145-154 (2001).

[69] C. Hidalgo, C. Alejaldre, A. Alonso, J. Alonso, L. Almoguera, F. de Aragon, E. Ascasibar, A. Baciero, R. Balbin, E. Blanco, J. Botija, B. Branas, E. Calderon, A. Cappa, J.A. Carmona, R. Carrasco, F. Castejon, J.R. Cepero, A.A. Chmyga, J. Doncel, N.B. Dreval, S. Eguilior, L. Eliseev, T. Estrada, J.A. Ferreira, A. Fernandez, J.M. Fontdecaba, C. Fuentes, A. Garcia, I. Garcia-Cortes, B. Goncalves, J. Guasp, J. Herranz, A. Hidalgo, R. Jimenez, J.A. Jimenez, D. Jimenez-Rey, I. Kirpitchev, S.M. Khrebtov, A.D. Komarov, A.S. Kozachok, L. Krupnik, F. Lapayese, M. Liniers, D. Lopez-Bruna, A. Lopez-Fraguas, J. Lopez-Razola, A. Lopez-Sanchez, E. de la Luna, G. Marcon, R. Martin, K.J. McCarthy, F. Medina, M. Medrano, A.V. Melnikov, P. Mendez, B. van Milligen, I.S. Nedzelskiy, M. Ochando, O. Orozco, J.L. de Pablos, L. Pacios, I. Pastor, M.A. Pedrosa, A. de la Pena, A. Pereira, A. Petrov, S. Petrov, A. Portas, D. Rapisarda, L. Rodriguez-Rodrigo, E. Rodriguez-Solano, J. Romero, A. Salas, E. Sanchez, J. Sanchez, M. Sanchez, K. Sarksian, C. Silva, S. Schchepetov, N. Skvortsova, F. Tabares, D. Tafalla, A. Tolkachev, V. Tribaldos, I. Vargas, J. Vega, G. Wolfers, B. Zurro, Overview of TJ-II experiment, *Nuclear Fusion* **45**, S266S275 (2005).

[70] C. Alejaldre, J. Alonso, L. Almoguera, E. Ascasibar, A. Baciero, R. Balbin, M. Blaumoser, J. Botija, B. Branas, E. de la Cal, A. Cappa, R. Carrasco, F. Castejon, J.R. Cepero, C. Cremy, J.M. Delgado, J. Doncel, C. Dulya, T. Estrada, A. Fernandez, C. Fuentes, A. Garcia, I. Garcia-Cortes, J. Guasp,

J. Herranz, C. Hidalgo, J.A. Jimenez, I. Kirpitchev, V. Krivenski, I. Labrador, F. Lapayese, K. Likin, M. Linier, A. Lopez-Fraguas, A. Lopez-Sanchez, E. de la Luna, R. Martin, A. Martinez, L. Martinez-Laso, M. Medrano, P. Mendez, K.J. McCarthy, F. Medina, B. van Milligen, M. Ochando, L. Pacios, I. Pastor, M.A. Pedrosa, A. de la Pena, A. Portas, J. Qin, L. Rodriguez-Rodrigo, A. Salas, E. Sanchez, J. Sanchez, F. Tabares, D. Tafalla, V. Tribaldos, J. Vega, B. Zurro, D. Akulina, O.I. Fedyanin, S. Grebenshchikov, N. Kharchev, A. Meshcheryakov, K.A. Sarksian, R. Barth, G. van Dijk, H. van der Meiden, Confinemet studies in the TJ-II stellarator, *Plasma Physics and Controlled Fusion* **41**, B109-B117 (1999).

[71] E. Ascasibar, C. Alejaldre, J. Alonso, L. Almoguera, A. Baciero, R. Balbin, I. Blanco, M. Blaumoser, J. Botija, B. Branas, A. Cappa, R. Carrasco, F. Castejon, J.R. Cepero, A.A. Chmyga, J. Doncel, N.B. Dreval, S. Eguilior, L. Eliseev, T. Estrada, O. Fedyanin, A. Fernandez, J.M. Fontdecaba, C. Fuentes, A. Garcia, I. Garcia-Cortes, B. Goncalves, J. Guasp, J. Herranz, A. Hidalgo, C. Hidalgo, J.A. Jimenez, I. Kirpitchev, S.M. Khrebtov, A. Komarov, A.S. Kozachok, L. Krupnik, F. Lapayese, K. Likin, M. Liniers, A. Lopez-Bruna, A. Lopez-Fraguas, J. Lopez-Razola, A. Lopez-Sanchez, E. de la Luna, A. Malaquias, R. Martin, M. Medrano, A. Melnikov, P. Mendez, K.J. McCarthy, F. Medina, B. van Milligen, I.S. Nedzelskiy, M. Ochando, L. Pacios, I. Pastor, M.A. Pedrosa, A. de la Pena, A. Petrov, S. Petrov, A. Portas, J. Romero, L. Rodriguez-Rodrigo, A. Salas, E. Sanchez, J. Sanchez, K. Sarksian, S. Schchepetov, N. Skvortsova, F. Tabares, D. Tafalla, V. Tribaldos, C.F.A. Varandas, J. Vega, B. Zurro, Confinement and stability on the TJ-II stellarator, *Plasma Physics and Controlled Fusion* **44**, B307-B322 (2002).

[72] C. Alejaldre, L. Almoguera, J. Alonso, E. Ascasibar, A. Baciero, R. Balbin, M. Blaumoser, J. Botija, B. Branas, E. de la Cal, A. Cappa, R. Carrasco, F. Castejon, J. Castellano, J.R. Cepero, C. Cremy, J. Doncel, S. Eguilior, T. Estrada, A. Fernandez, C. Fuentes, A. Garcia, I. Garcia-Cortes, J. Guasp, J. Herranz, C. Hidalgo, J.A. Jimenez, I. Kirpitchev, V. Krivenski, I. Labrador, F. Lapayese, K. Likin, M. Liniers, A. Lopez-Fraguas, A. Lopez-Sanchez, E. de la Luna, R. Martin, L. Martinez-Laso, K.J. McCarthy, F. Medina, M. Medrano, P. Mendez, B. van Milligen, M. Ochando, L. Pacios, I. Pastor, M.A. Pedrosa, A. de la Pena, A. Portas, J. Qin, L. Rodriguez-Rodrigo, J. Romero, A. Salas, E. Sanchez, J. Sanchez, F. Tabares, D. Tafalla, V. Tribaldos, J. Vega, B. Zurro, Review of confinement and transport studies in the TJ-II flexible heliac, *Nuclear Fusion* **41**, 1449 (2001).

[73] F. Castejon, C. Alejaldre, J. Alonso, L. Almoguera, E. Ascasibar, A. Baciero, R. Balbin, M. Blaumoser, J. Botija, B. Branas, E. de la Cal, A. Cappa, R. Carrasco, J. R. Cepero, C. Cremy, J. Doncel, S. Eguilior, T. Estrada, A. Fernandez, C. Fuentes, A. Garcia, I. Garcia-Corts, J. Guasp, J. Herranz, C. Hidalgo, J.A. Jimenez, I. Kirpitchev, V. Krivenski, I. Labrador, F. Lapayese, K. Likin, M. Liniers, A. Lopez-Fraguas, A. Lopez-Snchez, E. de la Luna, R. Martin, L. Martinez-Laso, M. Medrano, P. Mndez, K.J. McCarthy, F. Medina, B. van Milligen, M. Ochando, L. Pacios, I. Pastor, M.A. Pedrosa, A. de la Pena, A. Por-

tas, J.Qin, L. Rodriguez-Rodrigo, A. Salas, E. Sanchez, J. Sanchez, F. Tabares, D. Tafalla, V.Tribaldos, J. Vega, B. Zurro, Latest Physics Results of TJ-II Flexible Heliac, *Problems of Atomic Science and Technology* **N 6**, Series: Plasma Physics 6.3 p. 3–7 (2000).

[74] F. Castejon, V. Tribaldos, I. Garcia-Cortes, E. de la Luna, J. Herranz, I. Pastor, T. Estrada, TJ-II Team, Enhanced heat confinement in the flexible heliac TJ-II, Nuclear Fusion **42**, 271280 (2002).

[75] M.A. Pedrosa, A. Lopez-Sanchez, C. Hidalgo, A. Montoro, A. Gabriel, J. Encabo, J. de la Gama, L.M. Martinez, E. Sanchez, R. Perez, C. Sierra, Fast movable remotely controlled Langmuir probe system, *Review of Scientific Instruments*, Vol. **70**, No. 1. (1999).

[76] C. Hidalgo, M.A. Pedrosa, E. Sanchez, B. Goncalves, J.A Alonso, E. Calderon, A.A Chmyga, N.B. Dreval, L. Eliseev, T. Estrada, L. Krupnik, A.V. Melnikov, R.O. Orozco, J.L. de Pablos, C. Silva, Physics of sheared flow development in the boundary of fusion plasmas, *Plasma Physics and Controlled Fusion* **48**, S169S176 (2006).

[77] M.A. Pedrosa, C. Hidalgo, E. Calderón, A. Alonso, R.O. Orozco, J.L. De Pablos, and the TJ-II team, Spontaneous edge $E \times B$ sheared flow development studies in the TJ-II stellarator, *Czechoslovak Journal of Physics* **55**, 1579-1587 (2005).

[78] M.A. Pedrosa, R.O. Orozco, C. Hidalgo, J.A. Alonso, J.L. de Pablos and C. Silva, On the time scales and statistical properties of turbulence during ExB sheared flow development in the TJ-II stellarator, *33rd EPS Conference*, ECA Vol. **30I**, P-1.139 (2006).

[79] C. Hidalgo, M.A. Pedrosa, L. Garcia, A. Ware, Experimental evidence of coupling between sheared-flow development and an increase in the level of turbulence in the TJ-II stellarator, *Physical Review* E **70**, 067402 (2004).

[80] M.A. Pedrosa, C. Hidalgo, E. Calderon, T. Estrada, A. Fernandez, J. Herranz, I. Pastor and the TJ-II team, Threshold for sheared flow and turbulence development in the TJ-II stellarator, *Plasma Physics and Controlled Fusion* **7**, p. 777-788, (2005).

[81] B.Ph. van Milligen, T. Kalhoff, M.A. Pedrosa, C. Hidalgo, Bicoherence during confinement transitions in the TJ-II stellarator, *Nuclear Fusion* **48**, 11503 (2008).

[82] C. Hidalgo, M.A. Pedrosa, N. Dreval, K.J. McCarthy, L. Eliseev, M.A. Ochando, T. Estrada, I. Pastor, E. Ascasibar, E. Calderon, A. Cappa, A.A. Chmyga, A. Fernandez, B. Goncalves, J. Herranz, J.A. Jimenez, S.M. Khrebtov, A.D. Komarov, A.S. Kozachok, L. Krupnik, A. Lopez-Fraguas, A Lopez-Sanchez, A.V. Melnikov, F. Medina, B. van Milligen, C. Silva, F. Tabares, D. Tafalla, Improved confinement regimes induced by limiter biasing in the TJ-II stellarator, *Plasma Physics and Controlled Fusion* **46**, 287297 (2004).

[83] J. Horacek, Measurement of edge electrostatic turbulence in the TCV tokamak plasma boundary, *PhD Thesis*, Faculte Sciences de Base, Ecole Polytechnique Federale de Lausanne, Lausanne (2006).

[84] J. Horacek, R.A. Pitts, A.H. Nielsen, O.E. Garcia, Understanding SOL plasma turbulence by interchange motions, *Bulletin of the American Physical Society* (52), Vol. **16**, p. 192–193 (2007).

[85] A.V. Chankin, D.P. Coster, N. Asakura, G.D. Conway, Corrigan, S.K. Erents, W. Fun-damenski, Gunter, J. Horacek, A. Kallenbach, M. Kaufmann, C. Konz, K. Lackner, H.W. Muller, J. Neuhauser, R.A. Pitts, M. Wischmeier, A possible role of radial electric field in driving parallel ion flow in scrape-off layer of divertor tokamaks, *Nuclear Fusion* (**47**), p. 762–772 (2007).

[86] R. Schrittwieser, J. Adamek, P. Balan, M. Hron, C. Ionita, K. Jakubka, L. Kryska, E. Martines, J. Stockel, M. Tichy, G. Van Oost, Measurements with an emissive probe in the CASTOR tokamak, *Plasma Physics and Controlled Fusion* **44**, No. 5, p. 567–578 (2002).

[87] A.V. Melnikov, L.G. Eliseev, The direct measurements of the plasma electric potential by heavy ion beam probe on T-10 tokamak. Does T-10 obtain the H-mode?, *Czechoslovak Journal of Physics* **49** Suppl. 3, 35–40 (1999).

[88] J. Adamek, C. Ionita, R. Schrittwieser, J. Stockel, M. Tichy, G. Van Oost, Direct Measurements of the Electron Temperature by a Ball-pen/Langmuir probe, *Proceedings of the 32nd EPS Conference*, ECA Vol. **27A**, P-1.179 (2003).

[89] R. Schrittwieser, C. Ionita, J. Adamek, J. Brotankova, J. Stockel, E. Martines, C. Costin, G. Popa, L. van de Peppel, G. Van Oost, Direct measurements of the plasma potential by katsumata-type probes, *Czechoslovak Journal of Physics* (**56**), p. B145–B150 (2006).

[90] J. Adamek, V. Rohde, H.W. Muller, A. Herrmann, C. Ionita, R. Schrittwieser, F. Mehlmann, J. Stockel, J. Horacek, J. Brotankova a and ASDEX Upgrade Team, Direct measurements of the plasma potential in ELMy H-mode plasma with ball-pen probes on ASDEX Upgrade tokamak, *Journal of Nuclear Materials*, doi:10.1016/j.jnucmat.2009.01.286 (2009).

[91] J. Brotankova, J. Adamek, E. Martines, J. Stockel, M. Spolaore, R. Cavazzana, G. Serianni, N. Vianello, M. Zuin, Measurements of plasma potential and electron temperature by Ball-pen probes in RFX-mod, *Problems of Atomic Science and Technology* No. 1, *Series:* Plasma Physics (15), p. 16-18 (January 2009).

[92] I. Katsumata, M. Okazaki, Ion Sensitive Probe-A New Diagnostic Method for Plasma in Magnetic Fields, *Japanese Journal of Applied Physics* (**6**), p. 123–124 (1967).

[93] V.I. Demidov, S.V. Ratynskaia, K. Rydpal, Electric probes for plasmas: The link between theory and instrument, *Review of Scientific Instruments*, Vol. **73**, No. 10, p. 3409 (October 2002).

[94] T. Bolzonella, N. Pomaro, G. Serianni, D. Marcuzzi, New wide bandwidth in-vessel magnetic measurement system for RFX, *Review of Scientific Instruments* Vol. **74**, No. 3 (March 2003).

[95] P. Sonato, G. Chitarin, P. Zaccaria, F. Gnesotto, S. Ortolani, A. Buffa, M. Bagatin, W.R. Baker, S. Dal Bello, P. Fiorentin, L. Grando, G. Marchiori, D. Marcuzzi, A. Masiello, S. Peruzzo, N. Pomaro, G. Serianni, Machine modification for active MHD control in RFX, *Fusion Engineering and Design*, 66-68, 161-168 (2003).

[96] G. Serianni, T. Bolzonella, R. Cavazzana, G. Marchiori, N. Pomaro, L. Lotto, M. Monari, C. Taliercio, Development, tests, and data acquisition of the integrated system of internal sensors for RFX, *Review of Scientific Instruments* Vol. **75**, No. 10 (October 2004).

[97] G. Serianni, T. Bolzonella, R. Cavazzana, G. Marchiori, N. Pomaro, L. Lotto, M. Monari, C. Taliercio, Development, tests and data acquisition of the Integrated System of Internal Sensors for RFX, *Proccedings of the 15th topical conference on high temperature plasma diagnostics: Review of Scientific Instruments* Vol. **75**, 3381 (2004).

[98] G. Serianni, W. Baker, S. Dal Bello, High-spatial resolution edge electrostatic probe system for RFX, *Review of Scientific Instruments* Vol. **74**, No. 3 (March 2003).

[99] R. Cavazzana, P. Scarin, G. Serianni, M. Agostini, F. Degli Agostini, V. Cervaro, L. Lotto, Y. Yagi, H. Sakakita, H. Koguchi, Y. Hirano, Optical and electrical diagnostics for the investigation of edge turbulence in fusion plasmas, *Review of Scientific Instruments* Vol. **75**, No. 10 (October 2004).

[100] B. A. Carreras, R. Balbin, B. van Milligen, M.A. Pedrosa, I. Garcia-Cortes, E. Sanchez, C. Hidalgo, J. Bleuel, M. Endler, H. Thomsen, A. Chankin, S. Davies, K. Erents, G.F. Matthews, Characterization of the frequency ranges of the plasma edge fluctuation spectra, *Physics of Plasmas* Vol. **6**, No. 12 (December 1999).

[101] M.A. Pedrosa, C. Hidalgo, B.A. Carreras, R. Balbin, I. Garcia-Cortes, D. Newman, B. van Milligen, E. Sanchez, J. Bleuel, M. Endler, S. Davies, G.F. Matthews, Empirical Similarity of Frequency Spectra of the Edge-Plasma Fluctuations in Toroidal Magnetic-Confinement Systems, *Physical Review Letters*, Vol. **82**, No. 18, (May 1999).

[102] V. Antoni, R. Cavazzana, D. Desideri, E. Martines, G. Serianni, L. Tramontin, Electrostatic Turbulence and Transport in the Velocity Shear Layer of a Reversed Field Pinch Plasma, *Physical review letters*, Vol. **80**, No. 19, p. 4185-4188, (1998).

[103] R. Panek, O. Bilykova, V. Fuchs, M. Hron, P. Chraska, P. Pavlo, J. Stockel, J, Urban, V. Weinzettl, J. Zajac, F. Zacek, Reinstallation of the COMPASS-D tokamak in IPP ASCR, *Czechoslovak Journal of Physics* Vol. **56**, Suppl. B, p. 125-137 (2007).

Contents